UNIVERSITÀ DEGLI STUDI DI PADOVA

Physics and Astronomy Department "Galileo Galilei"
Master in Astrophysics and Cosmology

Looking for Binary Companions with Doppler Measurements of Directly Imaged Exoplanets

Supervisor:

Prof. Luca Malavolta

Co-supervisor:

Dr. Silvano Desidera

Dr. Cecilia Lazzoni

Candidate:

Ilaria Giovannini

Academic Year 2023/2024

Acknowledgements

I want to thank the people who accompanied me during these six months of analysis and writing of my thesis, offering constant inspiration and contributing, step by step, to the realization of this project. I thank my Co-supervisors, Dr. Silvano Desidera and Dr. Cecilia Lazzoni, and my Supervisor, Prof. Luca Malavolta. Thanks to their valuable support and shared expertise, I was able to deepen my knowledge of exoplanets, laying a solid foundation for my future as an observational astronomer.

I want also to thank Dr. Florian Rodler, Dr. Kevin Hoy, and Dr. Alice Zurlo for kindly providing the data used in this thesis and for their contribution to my research work.

Abstract

Context. As of today, more than 5500 exoplanets have been discovered, and yet no satellite has been confirmed around any of them. Satellites, exomoons or binary companions, are objects that orbit around an exoplanet or brown dwarf. These objects are important to define better the possible formation scenarios of the whole system and its dynamical evolution.
Aims. With this project, I will select a group of exoplanets and brown dwarfs detected with a specific technique, called direct imaging, and with conditions suitable for the detection of satellites through the radial velocity technique.
Methods. I first selected the sub-group of self-luminous exoplanets and brown dwarfs, detected with the direct imaging technique, as provided by the NASA and European archives. Then, I restricted the sample to those targets that were suitable for radial velocity measurements. This is a cutting-edge technique since I am trying to retrieve radial velocities from the planetary spectrum, not from the stellar one. I thus estimated the radial velocity semi-amplitude of each object in the catalogue to compute detection limits for satellites with the state-of-the-art spectrographs that are available nowadays, the near-infrared high-resolution spectrograph CRIRES+ and its link to the extreme adaptive optics system of SPHERE (HiRISE) at VLT. In this radial velocity precision study, the target's main characteristics, such as mass, angular separation, effective temperature and its contrast with the host star, were taken into account, along with the properties of the assigned instrument, either CRIRES+ or HiRISE. Moreover, I calculated the fraction of stellar contamination that perturbed the target spectrum.
Results. I selected a total of 5 targets, HR 3549 B, HIP 64892 B, and HD 984 B for CRIRES+ and β Pic b and HD 1160 B for HiRISE, with the most promising conditions for the detection of satellites with future observations. Among them, HR 3549 B has the lowest detection limits, pushing down to $\sim$40 m/s. This translates to a minimum detectable mass for the satellite of $0.06 M_J$ at a separation of 0.035 AU from the host planet. Increasingly more massive satellites might be revealed on wider orbits around the planet. Moreover, 3 additional objects, η Tel B, HIP 78530 B and HD 284149 b are also very promising considering treatments of the CRIRES+ PSF shape at large separations (> 1"), which in this work resulted in an overestimate of contamination of the spectra by the central star.
Conclusions. This project is an important baseline for proposals submission and observations aiming to detect satellites around directly imaged exoplanets and brown dwarfs through measurements of the Doppler shifts of substellar spectral lines. Moreover, with the upcoming next-generation instruments such as the ANDES spectrograph at ELT, this kind of study will be even more relevant because it provides the basis for the systematic analysis and possible detection of a wide group of satellites.

Keywords: Exomoons; Radial Velocity; Direct Imaging; Exoplanets; Formation

Contents

Glossary

AO Adaptive Optics

AU Astronomical Units

BD Brown Dwarf

CCD Charge-Coupled Device

CPD Circumplanetary Disc

CPI Common Path and Infrastructure

CRIRES+ CRyogenic high-resolution InfraRed Echelle Spectrograph

DM Deformable Mirror

E-ELT European Extremely Large Telescope

ESA European Space Agency

ESO European Southern Observatory

ExAO Extreme Adaptive Optics

FB Fibre Bundle

FEM Fibre Extraction Module

FIM Fibre Injection Module

FFP Free-Floating Planet

FGS/NIRISS Fine Guidance Sensor and Near Infrared Imager and Slitless Spectrograph

FoV Field of View

GPI Gemini Planet Imager

HabEx Habitable Exoplanet Imaging Mission

HCI High Contrast Imaging

HiRISE High-Resolution Imaging and Spectroscopy of Exoplanet

HRS High Resolution Spectroscopy

HST Hubble Space Telescope

HZ Habitable Zone

IFS Integral Field Spectrograph

IR Infrared

IRDIS Infrared Dual-band Imager and Spectrograph

JWST James Webb Space Telescope

KBO Kuiper Belt Object

LGS Laser Guide Star

LOS Line of Sight

MACAO Multi-Applications Curvature Adaptive Optics

mas milliarcseconds

MIRI Mid-Infrared Instrument

NASA National Aeronautics and Space Administration

NGS Natural Guide Star

NIR Near-Infrared

NIRCam Near Infrared Camera

NIRSpec Near Infrared Spectrograph

SCExAO Subaru Coronagraphic Extreme Adaptive Optics

SED Spectral Energy Distribution

SMF Single Mode Fiber

SNR (S/N) Signal to Noise Ratio

SPHERE Spectro-Polarimetric High-contrast Exoplanet Research

SR Strehl Ratio

PSF Point Spread Function

TDV Transit Duration Variation

TRV Transit Radius Variation

TTV Transit Timing Variation

UV Ultraviolet

VLT Very Large Telescope

VIS Visible

WFS Wavefront Sensor

ZIMPOL Zurich IMaging POLarimeter

Introduction

Extrasolar planets, or exoplanets, are objects that orbit stars outside our Solar System. A planet is a celestial object that orbits a star, has a round shape, has reached hydrostatic equilibrium, and has cleared the neighbourhood from other smaller bodies. The first official exoplanet discovered in 1995, was 51 Pegasi b, by Mayor & Queloz (1995), a hot Jupiter orbiting around a Sun-like star. Hot Jupiters are a subclass of giant planets with a size comparable to the known Solar System planet, Jupiter, but very close to their host star, with a semi-major axis less than 0.1 AU (equivalent to a period of about 10 days for a Sun-like star). At that time this discovery was very unexpected and astonishing.
In almost 30 years, thanks to the contribution of numerous astronomers from the astrophysical community, the total number of confirmed exoplanets has reached a value of 5756 (03/09/2024)[1]. The enrichment of this catalogue was possible thanks to the various detection techniques developed, including radial velocity, transit method, gravitational microlensing, astrometry, pulsar timing, and direct imaging, together with the constant improvement in our ground-based and space-based instrumentation over the years.
Exoplanet research is important because it enhances our knowledge of planetary systems' diversity, formation, and evolution, along with the comprehension of habitability and the search of extrasolar life.

As for today, there are different detection techniques to discover and study exoplanets, each of them focuses on particular characteristics of the object and is enhanced in specific configurations of the planet-host star system (Fischer et al. (2014); Kaushik et al. (2024)). All of them, besides direct imaging, work by indirectly detecting the presence of the planetary companion, studying the visible effect that the object induces on the parent star, or surrounding objects, and are strongly influenced by the stellar activity. Instead, direct imaging is a powerful complementary method and the only one capable of recognizing the planet as an individual source of light, in principle as a result of the planet's thermal emission and reflected stellar light, even if as of today no planet has been detected with reflected light. This technique helps define in more detail possible formation scenarios and evolution mechanisms for the system itself and it can also provide insights into the atmospheric composition of the exoplanet. Direct imaging evaluates the planetary flux, which is higher in the infrared wavelength range and for younger planets. For this reason, the main targets, and also the objects of my research, are young self-luminous giant exoplanets at wide separation from their host star. In fact, well-separated planets have a reduced stellar flux that contaminates the intrinsic planetary spectrum, additionally, young planets are self-luminous because of their ongoing gravitational contraction which emits more light, thus it is easier to detect them. A better description of the main properties and targets of direct imaging is presented in chapter 1.

[1] https://exoplanetarchive.ipac.caltech.edu/

The main objective of this project is the search of satellites, in the form of exomoons or binary planets. As we look at our Solar System, rocky moons are widely represented both in masses and orbital characteristics. According to the NASA/JPL Solar System Dynamics[2] team, the current total number of moons in our Solar System is 293. Looking at the inner rocky planets, the Earth presents one large satellite, the Moon, and Mars has two tiny moons on very eccentric and high inclination orbits, Phobos and Deimos. However, these are only a few numbers compared to the variety of satellites orbiting around the Solar System's giant planets, Jupiter (95 moons), Saturn (146 moons), Uranus (28 moons), and Neptune (16 moons). Although we do not have examples of binary planets in our own Solar System, we can consider the Pluto-Charon pair to be the extent of such objects at the very lower end of the mass distribution.
In an article, by Ochiai et al. (2014), and also in a more recent one by Lazzoni et al. (2024), studying the formation of gravitationally bounded binary planets, they both concluded that at least 1 out of 10 systems might host a binary planet formed by an orbital crossing of a pair of planets. In Ochiai et al. (2014) they assumed that the two planets were formed by core accretion, while in Lazzoni et al. (2024) they assumed the formation by gravitational instability. All of this leads to the question: why shouldn't exo-satellites exist? And why shouldn't we look for them?
As for today, only some candidate companions have been proposed, such as two around transiting planets, Kepler-1625 b (Teachey & Kipping (2018)) and Kepler-1708 b (Kipping et al. (2022)), one orbiting a directly-imaged brown dwarf, DH Tau B (Lazzoni et al. (2020)), and another around an isolated planetary-mass object, 2MASS J1119–1137 AB (Limbach et al. (2021)), yet none have been definitively confirmed.

The techniques known to possibly detect satellites are different. The most adopted ones are transit time variations (TTVs) and transit duration variations (TDVs) which rely on the transit method (Kipping (2009)). These techniques study the possible presence of a secondary companion, an exoplanet or an exomoon, that gravitationally perturb the orbit of the transiting one, breaking its strict periodicity and varying the measured mid-transit time or the transit duration. For a given planetary mass, both variations are proportional to the mass of the perturber, additionally, TTVs are related to the presence of small resonances (1:2 or 2:3). The presence of an exomoon will induce TDVs and simultaneously periodic out-of-phase TTV signals. However, the transit method is more successful in detecting exoplanets at small separations from the host star. Inner exoplanets are statistically less favourable to host exomoons due to either the outcome of the migration mechanism, for example in hot Jupiters (Trani et al. (2020)), or strong tidal perturbations from the central star that disrupt the satellite. In fact, hot Jupiters have a small Hill radius, which is the outermost stable orbit around a planet, and the star's tidal forces would destabilize any satellite's orbit. Another method is the Rossiter-McLaughlin effect (Zhuang et al. (2012); Gaudi & Winn (2007)). It is a spectroscopic phenomenon observed when a satellite is seen to transit across the face of the parent star distorting its typical radial velocity due to the stellar rotation. These motions produce blueshifts and redshifts, in the star's spectrum, usually observed as a broadening of the spectral lines. A third common method to discover exomoons is the microlensing technique, which studies the light coming from a background star deviated by a foreground lens system which, in some cases, could be a moon-planet system. The outcome is a bump in the light curve caused by a temporary magnification of the background source. The bump properties

[2] https://ssd.jpl.nasa.gov/

reflect the caustic-crossing configurations and the relative distance between the observer and the two sources. Sajadian & Sangtarash (2023) evaluated the efficiency of the Roman telescope, which will be launched in May 2027, in detecting these moon-induced perturbations, which is (0.002-0.094)%. However, these events are unpredictable, unrepeatable, and short-lived, so most of the time they are difficult to study in details, especially if the level of precision of a satellite companion is sought.
A better illustration of these techniques, along with all the other techniques for the detection of satellites or binary companions, is illustrated in chapter 2.

In this project, I decided to search for satellites around directly imaged exoplanets. The direct imaging technique, thanks to its capability to resolve the exoplanet from the host star, makes it possible to adapt all the other methods for exoplanet discoveries to satellites' detection, with some additional limits in the application. In particular, the techniques are applied considering the exoplanet as the equivalent of the central star and the satellite as the detectable companion. A detailed analysis of the limitations of the different methods applied on a planetary target, β Pic b, is illustrated in Lazzoni et al. (2022). Moreover, directly imaged exoplanets are typically well separated from the central star, so the capability of giant exoplanets to form and preserve satellites is higher with respect to hot Jupiter's (Trani et al. (2020)), because proto-satellites would feel less tidal perturbations from the host and would have more space to develop into.

To identify these objects, first I constructed a catalogue, illustrated in chapter 3, which collects all the discovered exoplanets with the direct imaging technique. Such sample was then restricted to exoplanets which had an angular separation smaller than 10" and orbiting stars with a magnitude brighter than 12 mag. In fact, planets further away from the host star will not satisfy the instrumental requirements needed to retrieve the spectrum, and fainter hosts do not produce any improvement in the adaptive optics systems of both adopted instruments.
I collected the data from NASA[3] and European[4] catalogues. After this, in Section 3.4 are illustrated in details the different types of instrumentation employed during this analysis and, in particular, for every object in the catalogue, I associated an instrument between CRIRES+ (CRyogenic high-resolution InfraRed Echelle Spectrograph, Dorn et al. (2023)) and HiRISE (Otten et al. (2021)), based on their main characteristics and capabilities.
In the second part of the analysis, presented in chapter 4, the focus shifted to the evaluation of the host star contamination in the planetary spectra and the study of the radial velocity perturbation induced on the planet by a possible satellite companion. This was done by sampling a synthetic population of satellites around every planet of the catalogue and understanding their dynamical influence on the planet. Then, to figure out what type of satellites are detectable by the adopted instrumentation, for every planet the limits in the radial velocity precision are evaluated, based on the planet's and instrument's characteristics.
Finally, in the last chapter, the conclusions and future prospects of this work are illustrated. In particular, with the upcoming next-generation telescopes, such as the E-ELT[5], and the upcoming instruments with unprecedented angular resolution, such as the ANDES spectrograph at ELT (Marconi et al. (2024); Palle et al. (2023)), this project will serve as a founding block for the optimal exploitation of advanced and future research.

[3] https://exoplanetarchive.ipac.caltech.edu/
[4] https://exoplanet.eu/catalog/
[5] https://elt.eso.org/

Chapter 1

Direct imaging

This project consists of the search of satellites, either rocky exomoons or more massive binary companions, around directly imaged exoplanets. This chapter provides a detailed overview of the main properties of the direct imaging method, including its key features, typical targets, and some of the main techniques used for detection.

1.1 Introduction

The first exoplanet discovered with direct imaging is 2MASS J1207334-393254 b (2M1207 b) by Chauvin et al. (2005b). This exoplanet was detected with the infrared wavefront sensor of VLT/NACO and it is a $5M_J$ planet around the brown dwarf 2M1207 A. From this discovery, the number of objects detected with this technique has increased and will continue to increase, thanks to the rapid improvement of high-contrast instruments. Figure 1.1 shows the distribution of the semi-major axis of all exoplanets discovered up to July 23, 2024, with the various techniques, as a function of their mass. This plot illustrates that direct imaging is particularly effective for detecting exoplanets that are far from their host stars, making it an important method for finding planets that other techniques are not able to reach. A detailed analysis of the typical targets of direct imaging is discussed in Section 1.5.

Direct imaging is the only method that offers the capability to detect an exoplanet considering it as a point self-luminous source due to its thermal emission. To directly detect an exoplanet, the most relevant parameters are the intrinsic planetary flux and its separation from the host star. The former depends on the age of the planet, as well as its mass and formation mechanism. Observations in the infrared range are preferred because, not only the stellar emission decrease along with its contamination, but also the intrinsic planetary flux increases. Nowadays, only young, warm and, thus self-luminous planets are within reach of ground-based instrumentation that can push down to contrasts of 10^{-6} at a few arcsecs from the host star (Perryman (2018)). This is expected to improve with the upcoming next 30-40m telescopes, even if, directly detecting an Earth-like planet is still a distant objective.

When the exoplanet is too faint to be directly detected, it is convenient to put some limits on its mass by evaluating the contrast ratio, $F_p/F_\star$. This ratio compares the planet's flux, F_p (which includes both reflected and thermal light), to the star's flux, $F_\star$

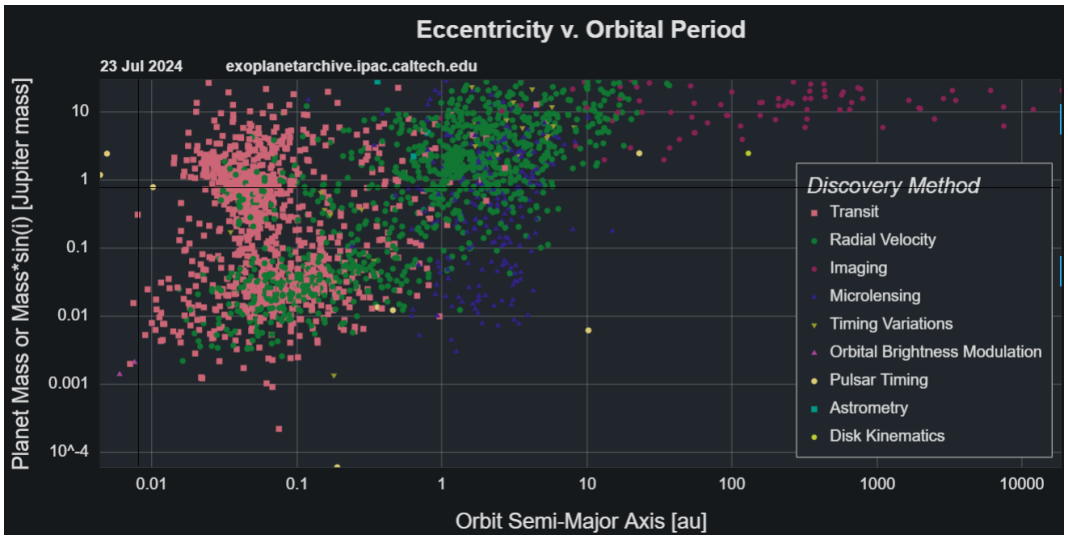

Figure 1.1: Planets discovered till 23rd July 2024 with all the detection techniques. Direct imaging focuses on planets well separated from the host star with respect to the other methods. Source: NASA Exoplanets Archive https://filtergraph.com/nea/default/index/4707728.

and it depends on many factors such as the stellar spectral type, the planet's orbital semi-major axis, mass, composition, radius, and age, and the wavelength of the observation. The dependence on the wavelength of the observation for the intrinsic (thermal) flux is related to the effective temperature of the exoplanet, as well as its gravity and chemical composition. The dependence on the wavelength for the reflected flux is related to the albedo of the planet, which is its capability to reflect the light coming from the source star. In particular, a planet with a thick atmosphere, such as Venus, has a higher albedo and reflects more light, while a planet with no atmosphere, like Mercury, has a lower albedo and reflects less light. Since planets emit far less light than their host stars, the $F_P/F_\star$ ratio is typically very small. For example, the expected contrast of a Jupiter-like planet around a Sun-like star at a distance of 10 pc from the observer and angular separation of 0.5 arcsecs is 10^{-9} in the visible, and 10^{-5} in the mid-infrared, while for an Earth-like planet in the same system at an angular separation of 0.1 arcsecs, it drops to 10^{-10} in the visible, and 10^{-7} in the mid-infrared (Perryman (2018)).

Another parameter, fundamental to resolve the planet-star system, is the angular resolution. For definition, the angular resolution is a property of the telescope that defines the smallest angle between two close objects the instrument can resolve. Assuming a circular aperture, the resolution near the diffraction limit is proportional to the observing wavelength, λ, and the telescope diameter, $\theta = 1.22\ \lambda/D$ (see Figure 1.4). In particular, to resolve the planet, the value of the telescope's angular resolution should be smaller than the planet-star angular separation, which depends on the planetary orbital parameters and the distance of the system from the observer. The maximum angular separation between the planet and the star is $\theta = a(1 + e)/d$, where a is the semi-major axis in astronomical units (AU), d is the distance of the system from the observer in parsec (pc) and e is the eccentricity of the planetary orbit (Traub & Oppenheimer (2010)).

The telescope's angular resolution is strictly related to the Point Spread Function (PSF) which describes how the unresolved point light source appears in the final image and how the telescope responds to it. It is influenced by diffraction, aberrations, and optical imperfections in the telescope and characterizes the blurring of the image due to them.

A common mathematical model used to describe the PSF is the Airy disk, which is the result of self-destructive and self-constructive diffraction produced by a circular aperture, such as the primary mirror or lens of a telescope.
As shown in the left Figure 1.2, the Airy disk PSF shows a central peak surrounded by concentric rings of decreasing intensity when the distance between two peaks is smaller than θ, otherwise, the two central peaks will overlap and resolve the two light sources will be more difficult. The size of the central peak and the spacing of the rings depend on the aperture size of the telescope and the wavelength of observation. Therefore, provided to observe in the infrared interval of wavelength (750nm$< \lambda <$ 1mm), to lower the angular resolution, the diameter of the telescope should increase, and this is not always achievable due to the limited budget and technology capabilities. The interferometric observations are a possible solution since they coherently combine light coming from individual telescopes and, in this case, the angular resolution becomes $\theta = \lambda/2B$, where B is the distance of the two outermost telescopes. These types of observations are useful for very close and faint objects near bright stars.

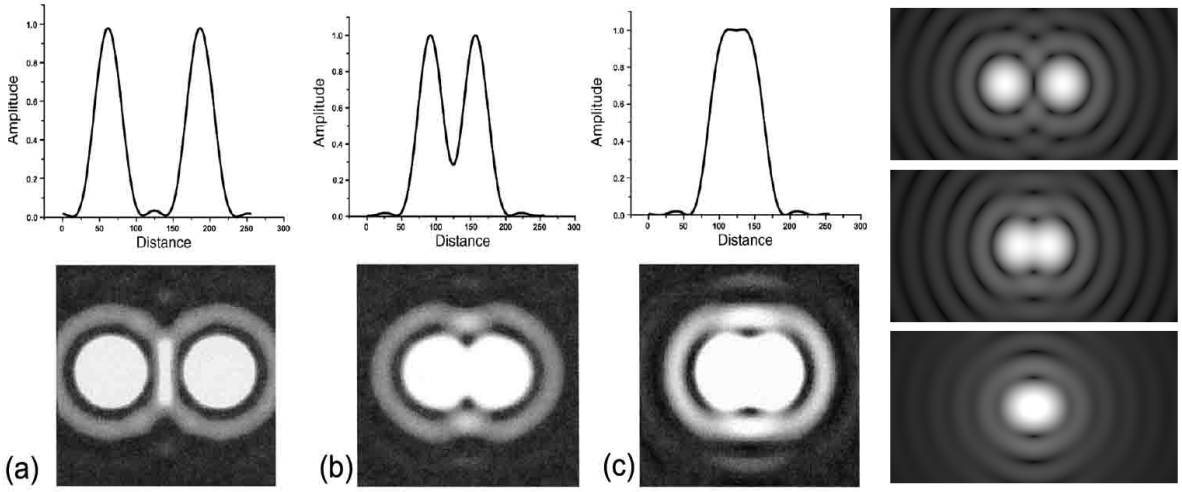

Figure 1.2: Different configurations of the airy disk based on the angular resolution of the telescope and the wavelength of observation.

Ground-based observations are limited by the Earth's atmosphere which can distort the final image and create speckles. The diffraction limit, which is the theoretical maximum resolving power of the telescope lens, can only be achieved with systems designed to remove the effects of the atmosphere (see Section 1.2) or observing with space-based telescopes (see Section 1.3). In the next sections, are illustrated these types of systems and their main characteristics.

1.2 High Contrast Imaging (HCI)

Today's efficiency of directly detecting exoplanets and planetary systems is related to the improvement of ground-based instrumentation: through Adaptive Optics (AO) systems, to minimize the effects of atmospheric turbulence; infrared (IR) detectors, to improve the planet-star contrast; coronagraphic techniques, to suppress light from the host star; and post-processing, to treat residual aberrations (Chauvin (2024), Perryman (2018)).

1.2.1 Adaptive optics (AO)

When observing from the ground, different temperature layers, or different wind speeds, generate atmosphere turbulences. These turbulences affect the light wavefront propagation preventing large telescopes from reaching the required spatial resolution. Before entering the pupil telescope, these turbulences can interact constructively and introduce a speckle pattern which often looks like a real source and is hard to distinguish (Zurlo (2024)). Adaptive Optics (AO) systems, introduced by Babcock (1953), offer a solution that tries to reduce this speckle noise quasi-simultaneously. The AO system, illustrated in Figure 1.3, is made up of three components: a wavefront sensor (WFS), which takes some of the astronomical light, a deformable mirror (DM), that lies in the optical path, and a real-time computer system, that receives input from the detector. The WFS measures the distortions introduced by the atmosphere on a timescale of a few milliseconds, then, the real-time computer calculates the optimal shape of the mirror to correct these distortions and reshape the surface of it accordingly. For example, an 8–10m telescope (like VLT or Keck) can produce AO-corrected images with an angular resolution of 30–60 mas at IR wavelengths, while the resolution without correction is of the order of 1 arcseconds.

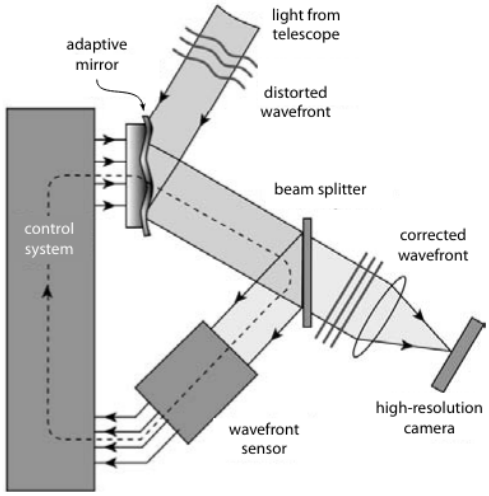

Figure 1.3: Typical structure of how an AO system works. The wavefront distorted by the atmosphere is reflected from a deformable mirror. The system operates in a closed loop, where a WFS measures the residual wavefront error after reflection and corrects the DM such as to leave the wavefront flat. These corrections are updated thousands of times per second to keep up with the rapidly changing effects of atmospheric turbulence. Source: Perryman (2018) (fig. 7.2).

To model the behaviour of the atmosphere, is necessary to collect light from a nearby brighter guide star or, in the absence of such a natural source, generate a laser guide star (LGS). The perfect AO correction would be obtained by taking as a guide star the source star itself, but when this source is very faint in the visible it cannot be utilized. The WFS detects and corrects the light of the guide star that, approximately, has passed through the same amount of atmospheric turbulence, and the image is corrected almost perfectly. The use of a guide star introduces two main limitations: the dependence on the guide star's magnitude to properly correct the distortions and the small field of view (FoV) in which the AO can operate (Babcock (1953)). In fact, too faint guide stars will not be useful for the AO correction, in addition, as the angular distance of the guide star

increases, the image quality after AO correction decreases. To increase the FoV and the sky coverage, different solutions have been developed, such as the introduction of LGS, a bright artificial laser beam propagated from the telescope and reflected from the higher atmosphere, when no nearby bright guide star can be found. Another solution is the multi-conjugate adaptive optics technique (MCAO), which utilizes multiple deformable mirrors to achieve a greater FoV (Guyon (2018)).
To understand how effective the AO correction is, the value of the Strehl ratio should be estimated. The Strehl ratio is the ratio between the peak intensity of the image and that of a perfect imaging system operating at the diffraction limit. One of the instruments adopted in this research, SPHERE, can correct for the atmospheric aberrations almost perfectly, with a Strehl ratio of 90% in the K-band and, with coronagraphy and image post-processing, can reach a contrast value of $10^{-6} - 10^{-7}$ at 0.5" separation (Perryman (2018)). While CRIRES+, in case of good conditions (seeing <0.8" and coherence time >3ms) and a bright (R < 7), nearby (within ∼5") reference source, has a SR larger than 30% in the K-band and the resulting PSF is still very close to the diffraction limit. At shorter wavelengths, for example in the J-band, or in case of poor conditions or a faint, distant reference source, the correction is only partial and the SR may only be a few percent.

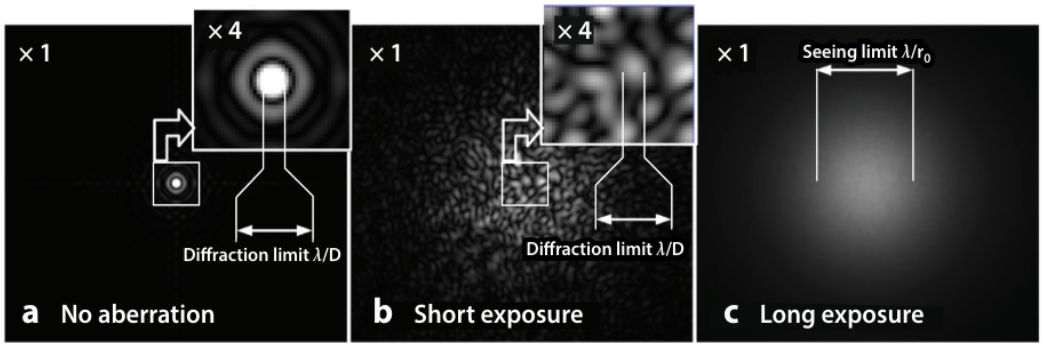

Figure 1.4: To the left (a) representation of a typical image in the absence of optical aberrations, where a telescope of diameter D that operates at the diffraction limit, delivers at a wavelength λ a PSF of angular width λ/D. At the center and to the right (b,c) representation of a typical image where light propagation has been distorted by atmospheric turbulence, which introduces optical path length delays yielding distorted/blurred images. Source: Guyon (2018) (fig. 4).

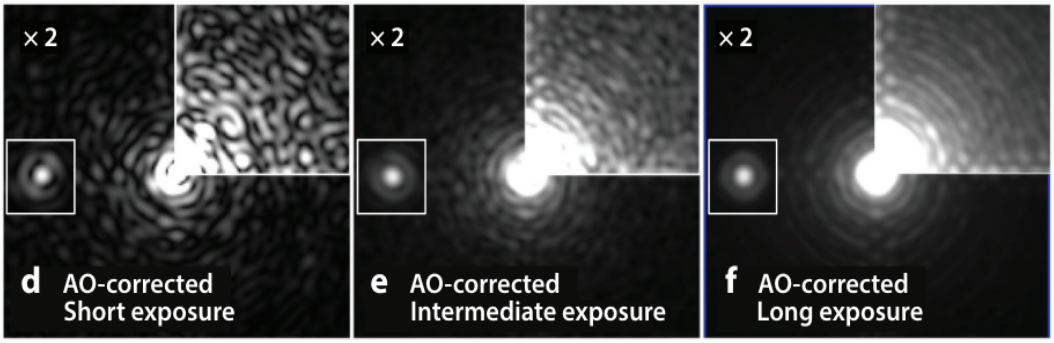

Figure 1.5: Representation of AO-corrected images with increasing exposure times. It shows that speckle noise averages to a smooth halo when the exposure time increases. Source: Guyon (2018) (fig. 4).

1.2.2 Coronagraph

Often, the contamination of the bright stellar light, makes it difficult to directly detect and resolve a planetary companion, because not only are planets a source of light extremely fainter than stars, but also the few light rays coming from them tend to be lost in the glare of their host star. This can be suppressed by adopting a coronagraph facility, which operates by placing a mask in the telescope's focal plane that blocks some of the stellar light. Figure 1.6 represents the difference between the outcome with Extreme Adaptive Optics (ExAO) alone and with an ExAO + coronagraph.

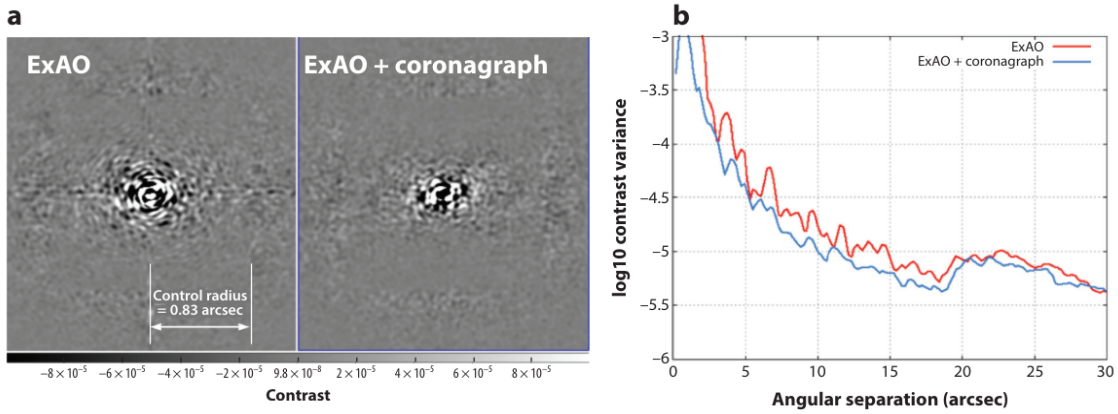

Figure 1.6: Left: representation of the difference of how the ExAO system works with and without coronagraph. Right: numerical simulation to represent how the PSF improves considering the coronagraph. Source: Guyon (2018) (fig. 9).

There are two main classes of coronagraph, the first class to be developed consisted of *solar coronagraphs*, which aimed to study and resolve the corona of our Sun, and then a new class of *stellar coronagraph* was developed to study the presence of extrasolar planets or circumstellar discs around nearby stars. Within this second type of attachment, there is the occulting-mask coronagraph, which uses an opaque mask that physically blocks light and manages diffraction effects, or phase-mask coronagraph, which adopts a transparent mask to shift the stellar light phase into a self-destructive interference and eliminates itself. The most utilized types of stellar coronagraphs are the first-generation Apodized Lyot coronagraph (ALC) (Guerri et al. (2009)), the second-generation four quadrant phase-mask (4QPM) (Rouan et al. (2000)), and the last-generation Apodizing phase plate coronagraph (APP) (Kenworthy et al. (2007)). Finally, there is also a class of satellite-based coronagraphs that are much more effective because of the absence of atmospheric scattering, which eliminates the largest source of noise present in a ground-based coronagraph.

1.3 Space-based imaging

Another way to remove atmospheric contamination and reach the diffraction limit is to observe directly outside of it with space-based facilities. The main limitation of these types of observation is the dimension. One of the aims of direct observations is to be able to resolve the exoplanet from the parent star and this can be done only if the angular resolution of the telescope is smaller than the angular separation of the two

objects. Recalling the equation for the angular resolution of a telescope, $\theta = \lambda/D$, at a given wavelength of observation, to reduce the resolving angle the diameter of the telescope should increase. This often brings some difficulties because of the limitations in technologies and budgets that do not let us construct space-based telescopes with the same dimensions as ground-based ones.
Despite these difficulties, some of the present and future instrumentation can be used for the direct detection of an exoplanet, such as the James Webb Space Telescope (JWST) and the Roman space telescope, which are illustrated in Sections 1.4.2 and 1.4.3.

1.4 Direct imaging facilities

Nowadays, lots of ground-based telescopes have been added with instruments capable of directly detecting and analyzing extrasolar planets, making use of a combination of large mirrors, AO, coronagraphs, and interferometers. However, as of today, there are no space-based telescopes completely dedicated to this technique, even if some of them have several imaging capabilities for exoplanets, such as the JWST or the future mission Nancy Grace Roman Space Telescope. This section also illustrates the main future missions and instruments that will bring important improvement in the direct search of exoplanets, such as the Habitable Exoplanet Imaging Mission (HabEx; still to be approved; Gaudi et al. (2019)) and the European Extremely Large Telescope (E-ELT; operating by the end of 2028; Marconi et al. (2024)).

1.4.1 Ground-based telescopes

The most relevant ground-based systems developed, almost in parallel, for different 8m-class telescopes are Gemini Planet Imager (GPI), Subaru Coronagraphic Extreme Adaptive Optics (SCExAO), and VLT-SPHERE. All these second-generation planet imagers can reach astrometric precision down to 1-2 mas with respect to the first-generations that were only able to reach 10-20 mas (Maire et al. (2021)).
Following the second generation of direct imaging instruments, a new generation of instruments has been developed, and will continue to be developed, aiming to connect spectral and spatial resolution at high precision levels, such as HiRISE at VLT, which couple CRIRES+ and SPHERE (Otten et al. (2021), reported in Section 3.4.2) and KPIC at Keck (Delorme et al. (2021)) which couple the Keck II AO system with the NIR-SPEC spectrograph.

GPI

GPI is a high contrast imaging instrument that was built for the 8-meter Gemini South Telescope in Chile, to detect faint exoplanets next to bright stars and probing their atmospheres at small angular resolution[1].
The system consists of high-order adaptive optics, a coronagraph, a calibration interferometer, and an integral field spectrograph. This instrument is built to detect infrared radiation from young Jupiter-like exoplanets in wide orbits and its first observations targeted already known planetary systems, including β Pic system, where GPI obtained the first-ever spectrum of the very young planetary companion, β Pic b (Macintosh et al. (2014)).

[1] https://www.gemini.edu/news/press-releases/gemini1401

SCExAO

SCExAO is a high-contrast imaging system for the 8.2-meter Subaru Telescope of the National Astronomical Observatory of Japan, located at the Mauna Kea Observatory in Hawaii[2].
The design of this system is very different from GPI or SPHERE, the coronagraph uses an Phase Induced Amplitude Apodization (PIAA) design which means it is able to image exoplanets closer to their stars with respect to conventional Lyot coronagraphs. For example, at a distance of 100 pc, the PIAA coronagraph on SCExAO is able to image from 4 AU outwards, while GPI and VLT-SPHERE from 12 AU outwards (Jovanovic et al. (2013)).

SPHERE

SPHERE (Spectro-Polarimetric High-contrast Exoplanet Research) is the extreme adaptive optics system and coronagraphic facility at the ESO-VLT (Very Large Telescope). Its primary science goal is imaging, low-resolution spectroscopy, and polarimetric characterization of extrasolar planetary systems at optical and near-infrared wavelengths[3].
In particular, in this thesis project SPHERE is adopted within HiRISE, an improved instrument that couples the high contrast imaging of SPHERE and the high-resolution spectroscopy of CRIRES+ with optical fibres (Otten et al. (2021)). For a detailed analysis of CRIRES+ and HiRISE systems see Sections 3.4.1 and 3.4.2, respectively.
The instrument design of SPHERE was optimized to provide the highest image quality and contrast performance in a narrow field of view (up to ∼10") around bright targets that are observed in the visible or near-infrared (Beuzit et al. (2019)). Moreover, SPHERE provides lower contrast values at smaller semi-major axis, which means that it improves the detection limits of giant exoplanets. When analyzing young giant exoplanets and brown dwarfs, that are still cooling down, the infrared wavelength range is interesting because it is where they present their peak of emissivity, hence where they are the brightest, for this reason, the SPHERE IR arm is designed to cover Y,J,H and K_s bands. SPHERE is installed at the UT3 Nasmyth focus of the VLT and includes the following sub-systems:

1. CPI (Common Path and Infrastructure) receives direct light from the telescope and provides highly stabilized, AO-corrected, and coronagraphic beams to the three sub-instruments: IRDIS, IFS, and ZIMPOL. The most important check for SPHERE observations concerns the AO performance, measured by the Strehl ratio (SR) which directly impacts raw contrast level. For targets with magnitude in the visible, R=9-10, SPHERE can reach in H-band an SR $\geq$ 90%.

2. IFS (Integral Field Spectrograph) provides the highest possible contrast for point source detection in the nearby area of the star. IFS has two possible configurations either at a spectral resolution of R∼50 between 0.95 - 1.35 μm (Y-J) or at R∼30 between 0.95 - 1.65 μm (Y-H), which provides a slightly deeper contrast and is more effective at shorter separation. In almost 50% of the cases, IFS obtains a contrast better than 10^{-6} for stars with $J < 6$ mag.

3. IRDIS (Infrared Dual-band Imager and Spectrograph) provides classical imaging (CI), dual-band imaging (DBI), dual-polarization imaging (DPI), and long slit spec-

[2] https://www.naoj.org/Projects/SCEXAO/scexaoWEB/000home.web/indexm.html
[3] https://www.eso.org/sci/facilities/paranal/instruments/sphere.html

troscopy (LSS) either between 0.95 – 2.32 μm, with resolving power of R$\sim$50 (LRS) or between 0.95 - 1.65 μm with R$\sim$350 (MRS).

4. ZIMPOL (Zurich IMaging POLarimeter) provides diffraction-limited classical imaging and differential polarimetric imaging (DPI) at $<$ 30 mas resolution in the visible, covering wavelength from 510 to 900 nm. Different CCD read-out modes are implemented, allowing for fast read-out noise for observations of bright targets, or low read-out noise for observations of faint targets.

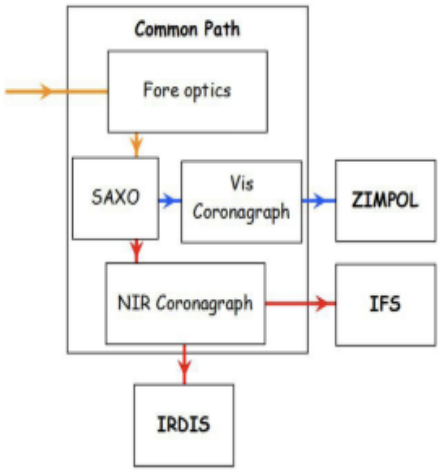

Figure 1.7: Global sub-system configuration of SPHERE; In orange are indicated the Optical beams for VIS+NIR, in blue for VIS and red for NIR. Source: Beuzit et al. (2019) (fig. 1).

1.4.2 Space-based telescope

JWST

The JWST was launched on 25 December 2021 on an Ariane 5 rocket from Kourou, French Guiana and in January 2022 it arrived at its destination, the Lagrange point L2[4]. It is a space telescope designed to conduct infrared astronomy to detect very far, old and faint objects. In particular, it observes a lower frequency range, from long-wavelength visible light through mid-infrared (0.6-28.3 μm) and because of this, the telescope must be kept extremely cold, below 50 K, to reduce as much as possible its IR light emissions that would interfere with the collected light. It is composed of the Optical Telescope Element (OTE), the Integrated Science Instrument Module (ISIM), the sun shield and the spacecraft bus. The sun shield protects the system from the heat of the Sun and Earth, while the spacecraft bus provides support for the operations. The OTE consists of the mirrors and the backplane that collects the light and gives it to the ISIM. The ISIM contains the four main cameras and science instruments and other subsystems:

- NIRCam (Near Infrared Camera) which is an IR imager with spectral coverage between 0.6-5 μm. It serves as the observatory's wavefront sensor used to align and focus the main mirror segments;
- NIRSpec (Near Infrared Spectrograph) which performs spectroscopy over the same wavelength range. It has three observing modes: a low-resolution mode using a prism,

[4] https://science.nasa.gov/mission/webb/

an R=1000 multi-object mode, and an R=2700 long-slit spectroscopy mode;

- MIRI (Mid-Infrared Instrument) which measures the mid-to-long-infrared wavelength range (5-27 μm). It contains both a mid-infrared camera and an imaging spectrometer and its temperature needs to be below 6 K.
- FGS/NIRISS (Fine Guidance Sensor and Near Infrared Imager and Slitless Spectrograph) which is used to stabilize the LOS of the observatory during science observations. The NIRISS module is used for astronomical imaging and spectroscopy between 0.8-5 μm.

JWST's advantages for exoplanet imaging are related to its large aperture, its operation at wavelengths greater than 3 μm, where young planets are brightest, its stability of the PSF and its great sensitivity. It approaches contrast limits of 10^{-5} with NIRCam and 10^{-4} for MIRI at 1" (Beichman et al. (2019)).

1.4.3 Future missions

Nancy Grace Roman Telescope

The Roman Space Telescope is a NASA observatory[5] that will be launched in May 2027 and it is designed to investigate dark energy, infrared astrophysics and also exoplanets. The telescope has a 2.4-meter primary mirror (the same size as the Hubble Space Telescope's (HST) primary mirror) and it will have two instruments, the Wide Field Instrument and the Coronagraph Instrument. The former is an IR camera with a FoV 100 times larger than HST, the latter is a system of masks, prisms, detectors and self-flexing mirrors that will block starlight from distant stars to directly reveal exoplanets and planet-forming discs.
The mission aims to directly detect worlds and dusty discs around nearby stars with detail up to a thousand times better than other observatories. While Roman is primarily an infrared telescope, it will be able to image worlds in visible light using the Coronagraph Instrument, which is predicted to achieve detection limits of 10^{-8} in flux ratio at separations of 150-450 mas at 575 nm (Bailey et al. (2023)).

HabEx

HabEx is a proposed space telescope mission concept developed by NASA with three driving science goals during its 5-years primary mission[6] (Gaudi et al. (2019)). One of them is to directly detect nearby worlds and explore them characterizing potentially habitable Earth-like exoplanets around Sun-like stars. If approved it will be launched in the 2030s and it will have a 4-meter diameter with imaging and spectroscopic capabilities from UV to NIR. The habitability will be hunted by measuring the spectra of detected planets and searching for signatures, such as water and possibly indicative of biological activity, such as oxygen or ozone. HabEx architecture is defined by a monolithic off-axis telescope with a diffraction limit at 0.4 μm and it will employ two starlight suppression systems: a coronagraph and a starshade. The main properties of the former are described in Section 1.2.2, while the latter is an external, large, flower-shaped, flat structure that blocks the starlight before it enters the telescope.

[5] https://science.nasa.gov/mission/roman-space-telescope/
[6] https://www.jpl.nasa.gov/habex/

Such a mission, if approved, will enable broad astrophysics and planetary science not possible from current or planned facilities.

E-ELT

The E-ELT, with its 40-meters diameter, will be the biggest optical telescope ever built from the ground and it will be operating by the end of 2028[7] (Marconi et al. (2024)).
To understand its capabilities, one night of observations with E-ELT, is equivalent to 25 nights of observations with VLT. The 40-m telescope of E-ELT will enable astronomers to reach down to contrasts never reached before, allowing astronomers to search for Earth twins. It's important to note that although the E-ELT will improve resolution and imaging capabilities, increasing the diameter from 8 to 40 meters will also lead to a significant growth of vibrations and environmental effects. The instruments of ELT, illustrated in detail in https://elt.eso.org/instrument/, included a diffraction-limited near-infrared imager (ELT-CAM: MICADO), a multi-conjugate adaptive optics unit that will feed MICADO (ELT-MORFEO), a single-field near-infrared integral field spectrograph (ELT-IFU: HARMONI), a first generation mid-infrared imager and spectrometer (ELT-MDIR: METIS), a high dispersion echelle spectrograph (ELT-ANDES) and a second-generation instruments with a multi-object spectrograph (ELT-MOS: MOSAIC). Moreover, an Extreme AO planetary camera and spectrograph (ELT-PCS) is included in the instrumentation plan, with the objective that E-ELT will be able to take images of Earth-sized exoplanets.

1.5 Targets of direct imaging

1.5.1 Giant planets

The main targets of this technique with currently available instrumentation are young, self-luminous, giant exoplanets. Young exoplanets are hotter and brighter since they release energy because of the ongoing gravitational contraction, and thus easier to be detected with respect to their older counterparts. Giant exoplanets, for definition, are objects more massive than 0.1-0.2 M_J and they can be distinguished into two main clusters, hot Jupiters and temperate-to-cold giants, represented in Figure 1.8. The former are very near to their host star (a<0.1 AU) and undergo very intense radiation from the parent star, the latter, are objects at larger separation with similar characteristics to our Solar System giant planets (0.4 AU<a<several AU). Between these two clusters, the radial velocity and transit detections have revealed the so-called period valley, a transition in which relatively few giant planets have been found. This valley in the period distribution of giant planets is strictly related to the different formation and migration mechanisms between temperate-to-cold giants and hot Jupiters (Santerne (2018)). In this project, the focus will be on temperate-to-cold giant planets because they are further out from their host star, thus easier to be detected with the direct imaging technique. Moreover, satellites around hot Jupiters are less favoured because of the tidal gravitational perturbation from the near star (Szabó et al. (2024)) or the outcome of a migration mechanism (Trani et al. (2020)).
After a statistical analysis of the properties of a population of giants with 1-75 M_J at orbital separations between 5-300 AU, Vigan et al. (2021) concluded that the frequency

[7] https://elt.eso.org/about/timeline/

estimate for temperate-to-cold giant planets is significantly higher for massive, B or A type, stars than for lower mass M dwarfs. In general, the occurrence of systems in which at least one companion has a mass between 1-75 M_J and a semi-major axis between 5-300 AU, is 23.0%, 5.8%, and 12.6% for B-A, F-G-K, and M stars, respectively. In particular, the frequency of systems in which at least one companion is a giant planet (mass between 2-13 M_J) and a semi-major axis between 3-100 AU around B-A type stars is 8.6%.

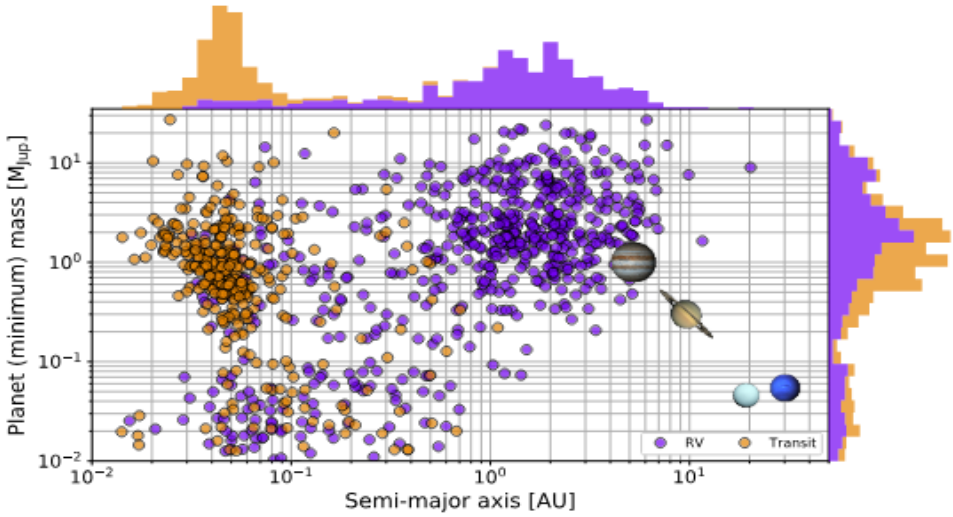

Figure 1.8: Extrasolar giant planets discovered to date (source: NASA Exoplanet Archive) by the transit (orange marks) and radial velocity (violet marks) surveys. The plot represents the planetary mass, in units of Jupiter masses, as a function of the semi-major axis, in units of AU. The top and right histograms represent the raw distribution of extrasolar planets in their semi-major axis and (minimum) mass, respectively. This reveals the two main populations of extrasolar giant planets and the period valley, where few objects have been found. For comparison, the Solar system planets are also present.

1.5.2 Brown dwarfs

Brown dwarfs (BD), or 'failed stars', are sub-stellar objects of masses ranging from about $13M_J$ to $75M_J$ and are interesting to include in the search of satellites or binary companions, because they occupy the domain between planets and stars (Perryman (2018)). The lower mass limit for brown dwarfs is the minimum mass necessary to ignite deuterium fusion, a process that does not occur in planets. The upper mass limit is the minimum mass needed to ignite nuclear hydrogen fusion into helium, which occurs inside stars but not BD. This classification is based on the mass rather than their formation mechanisms because, although objects with similar masses may have formed in different ways, nowadays it is difficult to precisely determine the exact process that brought to the final object. The detection and characterization of these objects are problematic due to their faintness and low temperatures. Moreover, their occurrence rate around solar-type stars is very small, almost 5-15 times lower than the occurrence rate of extrasolar giant planets. Vigan et al. (2021) found that the frequency of brown dwarf companions is much higher for low-mass M dwarfs than for higher mass, B or A type, stars.

1.5.3 Outcome of direct imaging

In general, when an exoplanet is directly detected it is possible to estimate the projected separation and the planetary flux. From the first one, the semi-major axis can be calculated knowing the eccentricity distribution. From the second one, if the system age is known with precision, it is possible to retrieve the planetary mass based on atmospheric models such as BT-SETTL (Allard (2014)), AMES-COND (Baraffe et al. (2003)) and ATMO (Phillips et al. (2020)). These models are being calibrated with systems where the dynamical mass of the planets is well characterized or constrained thanks to independent radial velocity and/or astrometric studies. Examples of the most adopted calibrating systems are HR 8799 b,c,d and e, β Pic b and 51 Eri b. In particular, the HR 8799 system is one of the most known and well-studied systems with direct imaging, astrometry and radial velocity techniques with a detailed characterization of their orbits and masses. These systems are fundamental to refining our theoretical models for planetary mass estimations. After their discoveries, young giant and well-separated planets are subject to continuous monitoring to put constraints on their planetary orbits. The orbital inclination can be estimated only when multiple epochs are available. Except for a few cases, where the orbital characterization was easier, such as β Pic b or the HR 8799 planetary system, their orbital motion is only partially resolved (Chauvin (2024)).
Additionally, as anticipated before, this technique can provide the resolved planetary spectra and/or the spectral energy distribution (SED) from which the effective temperature, gravity, and chemical composition can be retrieved.
Finally, direct imaging also contributes to a better definition of the formation scenarios, especially for young giant planets (see next section). Observing young planets is useful because they are still close to the epoch and site of their formation, and in some cases, they remain connected to their formation disc. This method also improves our knowledge of the system's architecture and its dynamical evolution. Additionally, it provides a better understanding of the formation of rocky planets, since giant planets can influence the system dynamics and overall structure.

1.6 Formation scenarios

Planetary systems are the by-products of star formation. After the first stages of protostar formation through the gravitational collapse of a molecular cloud, dust grains start to settle on the mid-plane of the system and, through collisions or gravitational instabilities, these grains grow in mass and size till they reach the planetesimal configuration. Planetesimals are bodies dominated by self-gravity whose dynamics are not any more affected by gas drag, typically larger than 1 km in size and similar to asteroids. In this phase, it is important to distinguish between different coagulation zones, which will bring different evolution scenarios. The first is the terrestrial zone, where planetesimals collect together to form sub-Earth-sized bodies. The second zone is beyond the snow-line or frost line, the distance in the solar nebula from the central protostar where the temperature is low enough for a particular volatile to condense. Different volatile have different condensation temperatures at different partial pressures, so different positions of their snowlines, for example, in our Solar system the snowline of water vapour separates the rocky planets from giants and it lies at 2.7 AU. Beyond this line, where the accretion material abounds, planetesimals can grow up to 5-10 Earth masses ($M_\oplus$) and start to accrete surrounding gas developing in giant planets. The third, and last, is the asteroid or Kuiper belt zone,

where the coagulation is incomplete due to exterior planets' perturbation, and planetesimals do not evolve into planets but remain smaller, such as asteroids or comets (Perryman (2018)).

The main limitation in the definition of a giant planet's formation scenario is to consider the presence of gas for the accretion during the process and their accretion time scales. There are two main models for the formation of giant exoplanets: core accretion and gravitational disc instability. In the former, the process begins with planetesimal coagulation and core formation, resembling the rocky planets' formation, followed by the accretion of a gaseous envelope. In the latter, the planet forms from a gravitational fragmentation in the circumstellar disc. It is important to note that these two mechanisms do not exclude themselves and they can both contribute to the formation of giant planets. Nowadays, the core accretion theory is the most widely considered and is also applied to our Solar System gas and ice giants (Pollack et al. (1996)), nevertheless, this model cannot justify the current observations of giant planets around metal-poor stars or at very large distances (Helled et al. (2014a)).

Core accretion

This formation scenario, also described as a "bottom-up" configuration, can be divided into different stages. The first one is the formation of a heavy-element core, which takes after the rocky planet formation, leading to a 5-20$M_\oplus$ core and a very low mass envelope of gas. After this, the second stage presents a rapid accretion by capturing surrounding gas into the envelope, along with a slow continuous accretion of the core. In this phase, the envelope and the core accrete almost simultaneously, and when the two masses become comparable the envelope accretion starts to accelerate into forming the final gas-giant planet. This stage ends when the protoplanetary disc cannot supply gas fast enough, either because of the opening of a gap or because the gas disc dissipates. In some cases, for smaller core masses or longer core formation time scales, the gas can be dispersed before the accretion is completed, and this may result in ice giants, rather than gas-rich giants. Finally, when the accretion phase stops, it begins a phase of contraction and cooling to reach the final configuration (Helled et al. (2014a)).

Gravitational disc instability

An alternative scenario, also described as the "top-down" model, is defined by a rapid single collapse in a massive, gravitationally unstable protoplanetary gas disc, mimicking the star formation process. This mechanism starts with some density perturbations that grow and develop into spiral arms, which transfer angular momentum outward and mass inward through gravitational torques. After this, the cooling or the mass infall can induce a further collapse of spiral arms into clumps (Helled et al. (2014a)), which can evolve or not into gas giant planets.
This model is weaker than core accretion because there are still a lot of uncertainties regarding how clumps form and behave or how they can evolve into planets. However, this mechanism justifies some inconsistencies in the core accretion model, such as the progressive accumulation of solids, form sub-μm scales upwards, and the lengthier formation time scale. In fact, in low metallicity systems, the disc dissipates faster and the core accretion model would not be a viable formation scenario because it has a time scale of $10^5 - 10^6$ years, while the gravitational instability has a time scale of $10^4 - 10^5$ years,

Helled et al. (2014b)).

1.6.1 Circumplanetary discs

Independently of which giant planet's formation scenario occurred, either core accretion or gravitational instability, at the last formation stages a circumplanetary disc (CPD) forms around the gas-giant planet. From such CPDs formation models predict the births of satellites, as it was for many of the rocky moons present in our Solar System. Numbers of CPDs detections are found around giant planets or brown dwarfs with masses near the planetary limit, for example, around the $2M_J$ PDS 70 c (Benisty et al. (2021)), $10M_J$ DH Tau B and $14M_J$ GSC 6214-210 B (van Holstein et al. (2021)), $1.2M_J$ HD 100546 b (Pineda et al. (2019)), and $10M_J$ SR 12 AB c (Wu et al. (2022)).

In the work by Szulágyi et al. (2017) they analyzed the different characteristics of the CPD relative to the formation scenario that took place. They simulated the two different formation scenarios with similar initial conditions and found that the CPD mass is linearly related to the circumstellar disc mass. However, a CPD around an exoplanet formed with a gravitational instability scenario would be only 8 times more massive than one around an exoplanet formed assuming a core accretion scenario and, with only this information, it is not possible to distinguish between the two scenarios. Instead, a CPD around a planet formed in the core accretion model will have a temperature of at least one order of magnitude higher than one around a planet formed in the gravitational instability model. The temperature of CPDs depends on many factors, such as the semi-major axis of the planet, the local density and opacity, and the planet's mass and age. For this reason, a detailed characterization of the CPDs properties, in particular their temperature, is important to better understand not only the formation scenario of the hosting gas giant planet but also to improve the knowledge of satellite formation models, whose final configuration depends on the time scales of gas dissipation (Mosqueira & Estrada (2003)).
The characteristics of the CPD affect its detectability, so in one of the works by Szulágyi et al. (2019) they tried to model circumplanetary discs in NIR wavelengths concluding that the CPD's brightness is 20-100 times higher than the planet's and this misinterpretation could lead to an overestimation of the planet's mass by over an order of magnitude. They also concluded that the CPD's magnitude depends on the disc's parameters such as the dust-to-gas ratio, the viscosity or the distance from the central star. Moreover, in following works, they studied the detectability of a CPD around a giant planet with SPHERE (Szulágyi & Garufi (2021)), JWST and ELT (Chen & Szulágyi (2022)), by injecting scattered light in mock observations and adopting the polarized differential imaging technique, to mimick the method to detect circumstellar discs. For SPHERE, they found out that a CPD at 50 AU from a solar-type host star is easier to detect around more massive planets ($M_P > 5M_J$) and in a nearly face-on configuration ($i<30°$). Regarding JWST and ELT, they concluded that the best wavelengths to detect a CPD are mid-IR wavelength range and beyond, plus JWST/MIRI and ELT/METIS produce the best results.

Chapter 2

Exomoons and binary planets

The goal of this project is to detect an exomoon or a more massive binary companion orbiting a giant extrasolar planet. This will be done by analyzing the spectroscopic perturbations caused by their presence. To have a clearer understanding of these still unknown objects it is convenient to first examine their counterparts within the Solar System, as discussed in Section 2.1, focusing on their main characteristics and formation scenarios. To begin this analysis, it is important to review the key features of the major Solar System moons. This helps establish a clear starting point for this analysis and to keep in mind the key characteristics to focus on. However, it is important to remember that the Solar System cannot be considered a general model we can rely on but rather a specific configuration, as shown by the discovery of the first exoplanet (Mayor & Queloz (1995)). Therefore, the discovery of the first exosatellite may reveal completely different characteristics from the moons we are familiar with.
Then, in Sections 2.2 and 2.3 are analyzed the formation scenario and stability criteria of these objects around their primary companion. The last Section, 2.5, presents an illustration of the various detection methods, highlighting their advantages and disadvantages. In particular, among these, the radial velocity technique, which is the primary method used in this study, is described in detail in chapter 4.

2.1 Solar System

Moons, or planetary satellites, are naturally formed bodies that orbit planets. The most studied planetary satellite is Earth's Moon. In our Solar System, the current total number of moons orbiting planets is 288: one orbiting Earth, two around Mars, 95 around Jupiter, 146 around Saturn, 28 around Uranus and 16 around Neptune. Moreover, over 470 small satellites are orbiting smaller objects, such as asteroids, dwarf planets (five moons are known to orbit Pluto for example), or Kuiper Belt Objects (KBOs) beyond Neptune's orbit.[1]
Moons in our Solar System are classified as either regular or irregular based on their physical and orbital characteristics. Regular moons follow a relatively close, stable and nearly circular orbit, often aligned with their planetary host equator. These moons typically form within the CPD after a major collision or from an accumulation of leftover materials in the early Solar System. Almost all planets in our Solar System host at least one regular

[1]Information about Solar System moons were found in https://ssd.jpl.nasa.gov/

satellite. The latter are a total of 60 objects, among which the most famous examples are Ganymede around Jupiter and Titan around Saturn, both larger than Mercury. Irregular moons, on the other hand, follow an eccentric, highly inclined orbit, often in retrograde motion. It is believed that these moons were once independent objects orbiting the Sun before being captured by a nearby planet, such as Triton around Neptune, the largest irregular satellite in our Solar System.
The natural satellites of the Solar System are fundamental indicators of its formation and evolution. For example, the different architecture of the Jovian and Saturnian moons suggests that these gas giants interacted differently with the circumstellar gas and debris disc. The satellites' configuration could indicate different evolutionary timescales of their CPDs.
As anticipated in Section 1.6.1, CPDs formed through core accretion and gravitational instability are very different. As a consequence, these two formation scenarios lead to different types of satellites (Szulágyi et al. (2017)). Inderbitzi et al. (2020) found more massive exomoons only around planets formed via gravitational instability, while their formation around planets formed through core accretion was excluded.

2.1.1 Inner planets' moons

The total number of moons in the inner part of the Solar System, before the Asteroid belt, is three. Mercury and Venus have no satellites, while Earth has one, the Moon, and Mars has two, Phobos and Deimos.

The *Moon* has a diameter of about 3 474 km and it is located at about 384 400 km from Earth. It takes approximately 27.3 days to complete one orbit around Earth, and its rotation is synchronized with its orbit, so it always shows the same face to Earth, a phenomenon known as tidal locking. This tidal locking causes tides, stabilizes Earth's axis, and gradually slows its rotation. The Moon's gravity is about one-sixth that of Earth, which significantly impacts its surface features and the behaviour of objects on it. The Moon is primarily composed of rocky material, with a surface covered in craters, plains, mountains, and valleys. It does not have a true atmosphere, only an exosphere, which is an extremely thin layer of gases. It is believed that the Moon formed about 4.5 billion years ago from debris ejected during a collision between Earth and a Mars-sized body called Theia, during the late stages of the Solar System's formation. This theory is supported by the similarity in isotopic compositions between Earth and Moon rocks, as well as computer simulations of the impact.

Phobos is the largest and closest of Mars' two moons. It orbits Mars at a very close distance and has an irregular shape, resembling a potato, with dimensions roughly 27 km $\times$ 22 km $\times$ 18 km. Phobos orbits Mars faster than Mars rotates and has a heavily cratered surface, indicating significant impacts over its history. *Deimos* is smaller, with a diameter of 15 km in diameter, and it is farther away from Mars. It has a more regular shape compared to Phobos, but also has a heavily cratered surface. Phobos and Deimos are believed to be captured asteroids from the asteroid belt.

2.1.2 Outer planets' moons

Jupiter, the largest planet in our Solar System, has 95 moons divided into groups based on their characteristics and orbits. The Galilean Moons, Io, Europa, Ganymede, and Callisto, are the four largest moons of Jupiter and were discovered by Galileo Galilei in 1610.

With around 400 active volcanoes, *Io* is the most volcanically active body in the Solar System. This is caused both by tidal heating, due to its proximity to Jupiter, and gravitational interactions with the other Galilean moons. *Europa* is believed to have a liquid water ocean beneath its icy surface, making it a very promising candidate for the search for extraterrestrial life. It has a radius of 1565 km, and its surface is relatively smooth with few impact craters. Both Io and Europa are tidally locked to Jupiter, always showing the same face to the planet. *Ganymede*, the largest moon in the Solar System with a radius of 2634 km, is even larger than Mercury and is the only moon known to have its own magnetic field. Its surface is very diverse, with both heavily cratered regions and younger, smoother terrains. Io, Europa and Ganymede are in a 1:2:4 orbital resonance, which perturbs Io's orbit in a more eccentric one. The last one, *Callisto*, is the most heavily cratered object in the Solar System with a radius of 2403 km and a very ancient surface. The most widely accepted theory for the formation of Galilean moons is the accretion model, which suggests that they formed from the same disc of gas and dust that surrounded Jupiter within the first few million years of the Solar System's history. The gravitational interactions between Jupiter and its moons led to tidal heating, which explains the high geological activity of these moons.
Besides the four Galilean moons, Jupiter has numerous smaller regular moons that orbit further out, such as Amalthea, Himalia, Elara, and Pasiphae, and some irregular moons on highly eccentric orbits, probably captured objects, as Themisto, Carpo, and Euporie.

Saturn has a total of 146 moons, mostly made of ice. The largest one is *Titan*, which is the only one with a thick atmosphere, primarily composed of nitrogen (N) with trace amounts of methane (CH_4) and ethane (C_2H_6). Titan's surface is covered in lakes and rivers of liquid methane and ethane, making it the only other body in the Solar System, besides Earth, with liquid on its surface. *Rhea* is Saturn's second-largest moon. Similar to *Dione* and *Tethys*, two other moons of Saturn, it has a heavily cratered surface with a tenuous atmosphere of oxygen (O_2) and carbon dioxide (CO_2). Rhea also has a high albedo suggesting a surface of water ice. Moreover, Dione might have a subsurface ocean, similar to Enceladus and Europa. *Enceladus* is a small, icy moon with a surface of geyser-like jets of water vapor and ice particles erupting from its south pole, indicating the presence of a subsurface ocean. Its geologically active surface suggests internal heating, possibly due to tidal forces. *Hyperion* is the largest of all irregular moons and has a chaotic rotation due to its low density. Its surface is covered in craters and has a porous, sponge-like appearance. It was likely formed through capture by Saturn's gravity. *Iapetus* is Saturn's third largest moon and it presents a stark colour dichotomy, with one hemisphere being much darker than the other. This is probably due to the deposition of dark material from ice volcanism. It also presents an unusual equatorial ridge along its equator. Most of Saturn's major moons, except two, are tidally locked with their parent planet, meaning the same side always faces Saturn. The formation of most of Saturn's regular moons is due to the accretion of icy materials in the outer regions of Saturn's protoplanetary disc. We can try to compare Jupiter's with Saturn's moons. Jupiter has four major satellites, three of which are locked in mean-motion resonances with each other. Saturn, instead, has only one large icy satellite, Titan, while the rest are small icy moons. The hypothesis formulated to explain these differences may come from the fact that Jupiter, being more massive than Saturn, was able to open a gap in the protoplanetary disc unlike Saturn, which hardly did. Such a scenario was also confirmed by means of numerical simulation (Sasaki et al. (2010)).

Uranus has 28 known moons, including five major ones: Miranda, Ariel, Umbriel, Titania, and Oberon. *Miranda* is the smallest of these, but it has a varied terrain with cliffs, canyons, and other unique geological features. Its surface suggests a complex geological history, possibly due to tidal heating from its interactions with Uranus and its other moons. *Ariel* is one of the Uranus' brightest moons and has a young surface compared to the others. *Umbriel* is the darkest of Uranus' major moons with a heavily cratered surface, like *Oberon*, the second-largest moon of Uranus. *Titania* is the largest moon of Uranus and has a relatively young surface with few large impact craters, signs of possibly tectonic processes or cryovolcanism.
These moons are believed to have formed from the CPD around Uranus during its early formation stages, and perhaps some may have been captured from the outer Solar System.

Neptune has 16 known moons, the largest one is *Triton*. Triton has a diameter of about 2 700 km, larger than Pluto. It orbits Neptune in a retrograde direction, meaning it moves opposite to the planet's rotation. Its surface is relatively young with geysers erupting nitrogen gas and dust. Triton is believed to be a captured Kuiper Belt object due to its composition resembling that of Pluto and other objects in the Kuiper Belt. *Proteus* is the second-largest moon of Neptune and has an irregular shape. It is heavily cratered and may be in a state of hydrostatic equilibrium, meaning its gravity has pulled it into a nearly round shape.
Neptune's other moons mostly have irregular orbits and shapes. Similar to Jupiter and Saturn's moons, the most widely accepted theory for the formation of Neptune's moons is that they formed from a debris disc left over from the planet's formation or were captured objects from the Kuiper Belt.

Pluto, despite being downgraded to dwarf planet, still counts 5 moons. The largest, *Charon*, is about half the size of Pluto. This system is often referred to as a "double dwarf planet" system because Pluto and Charon's mass ratio is the highest within all the Solar System moon-planet systems and they both orbit around a common centre of mass outside Pluto's surface. Charon's rotational period matches its orbital period, meaning it always presents the same face towards Pluto. Charon's surface is characterized by vast plains, mountains, and canyons. It is believed to have formed from a giant impact that has ejected material into orbit around Pluto. The other Pluto's smaller irregularly shaped moons are thought to have formed from the debris of the same impact that created Charon.

2.2 Satellites formation

2.2.1 Exomoons formation

The formation of exomoons is a natural by-product of the formation of planets.
The three main scenarios are giant impact, co-accretion and capture (Barr (2016); Teachey (2024)). The first scenario happens when there is an impact between two planetary embryos during the late stages of a system's evolution. In the early Solar System, impacts between embryos of 0.1-1 $M_{\oplus}$ were common around 200-300 Myrs after the dissipation of the solar nebula (Morbidelli et al. (2012)). This scenario justifies the formation of Earth's moon and Charon, Pluto's moon, but it can also explain the absence of moons around Mercury and Venus as well as their internal composition. The mass of materials orbiting the planet after such an impact represents an upper limit on the satellite's mass that

might form. The outcome of these collisions depends on the total ejected mass, M_o, with respect to the planetary mass, M_p (Barr (2016)). If $M_o/M_p > 0.03$ the most common outcome is the accretion of material into a single satellite. While, if $0.03 < M_o/M_p < 0.3$ two satellites are more likely to form.
In the co-accretion scenario, exomoons form from leftover materials in the CPD of the host planet. The most adopted co-accretion model is the Minimum Mass Sub-Nebula (MMSN) which uses the masses and locations of present moons to estimate the surface mass density of gas and solids as a function of the distance from the planet. An alternative scenario is represented by the gas-starved disc model, which predicts that gas within the CPD, which contains meter-sized particles of rock and ice, flows outwards from the planet and accretes into bodies large enough to de-couple from the gas and remain in orbit as satellites. This model predicts the maximum mass of a satellite or the total mass of the satellite system.
In the capture scenario, an initially unbound body is captured by the planet's gravity. This can occur either through intact capture, where the object ends up in orbit around the planet, or disintegrative capture, where an existing body disrupts and re-accretes around the parent body.
Besides these, fission is another mechanism for exomoons formation, but it cannot be directly applied to Solar System moons. However, it must be kept into account because it may be viable for exomoons discovered in future with properties different from Solar System moons. Fission is based on the break-off of the planet due to its high rotational rate and it was proposed as an alternative theory for the Moon formation but then ruled out by observational constraints.

The mechanisms of exomoon formation can be distinguished based on certain characteristics such as orbit, mass and composition. Understanding the properties of the companion is very important to put constraints into the formation scenarios. Looking at our Solar System it can be seen that moons in prograde, co-planar orbits (regular moons) are typically linked with the formation scenario of co-accretion, like the Galilean moons, or giant impacts, such as the Moon or Charon. While moons in retrograde and very inclined orbits (irregular moons) are linked to the formation by capture, such as Triton. Moreover, objects around gas giant planets typically have high density ratios $\rho_{sat}/\rho_{pl} > 1$, while around rocky/icy planets they have small density ratios $\rho_{sat}/\rho_{pl} < 1$, meaning that moons around these planets have a lower or similar density with respect to their host planet. Finally, in our Solar System, the giant impact scenario has produced companions with high mass ratios, such as Earth's Moon with M_s/M_P=0.01, and Pluto's moon with M_s/M_P=0.12, while satellites around outer planets, which typically formed by co-accretion, have lower mass ratios, around M_s/M_p=10^{-4}.

2.2.2 Binary companions formation

Binary planets are defined as two celestial bodies of similar size that are gravitationally bound and orbit a common centre of mass. The closest example in our Solar System is the Pluto-Charon dwarf planet system, which represents the low-mass end of the binary system distribution.
The formation of these systems is studied differently and remains more uncertain. For example, an article by Ochiai et al. (2014) and also a more recent one by Lazzoni et al. (2024) investigated simulations in which the binary system formed through orbital crossing and tidal capture of a pair of gas-giant planets. These gas giants were formed independently,

either by core accretion or gravitational instability, respectively. Both studies concluded similar results. In particular, Ochiai et al. (2014) affirm that at least 10% of binary planets form when the Hill sphere of one planet crosses the orbit of the other and the stability of these systems, considering ejection and merging rates, depends on the semi-major axis. They concluded that the binary system survives tidal decay only if it is beyond 0.3 AU from the central star. Moreover, they found that if the secondary planet enters the Hill sphere of the primary planet from the upper-left a prograde binary forms, while if it enters from the lower-left it results in a retrograde binary. On the other hand, Lazzoni et al. (2024) found that when planets experience repeated close encounters, systems can form binary planets at a frequency of 14.3%, with 2.4% of planets being ejected and 0.02% colliding with the central star. Thus, 11.9% of systems with planets formed by gravitational instability are likely to host at least one binary system.

2.3 Satellites stability

The basic requirement to detect a satellite is long-term stability. For a satellite to stabilize around an exoplanet, some prerequisites should be respected (Barnes & O'Brien (2002); Barr (2016)). The distance of the satellite from the host planet should be between the Roche radius, R_R, and a fraction of the Hill radius, R_H

$$R_R < a_s < fR_H$$

where f is a number between 0 and 1, typically fixed at 1/3 or 1/2. The Roche radius is the innermost distance a satellite can orbit the planet without being disrupted due to the planetary tidal gravitational forces. Its expression is given by the equation

$$R_R = R_P \left(2\frac{\rho_P}{\rho_s}\right)^{1/3}$$

where R_P is the planetary radius, ρ_P and ρ_s are the planetary and satellite's densities, respectively. On the other hand, the Hill radius is the outermost stable orbit beyond which the gravitational attraction of the planet is not effective anymore and the satellite slowly departs from its orbit. It is expressed as

$$R_H = a_P\,(1 - e_P)\left(\frac{M_P}{3M_\star}\right)^{1/3}$$

where a_P and e_P are the semi-major axis and the eccentricity of the planetary orbit, respectively, and M_P and $M_\star$ are the planetary and stellar mass, respectively. This implies that if the planet migrates inward reducing its semi-major axis (a_P), its Hill sphere contracts. As a result, the satellites orbiting the planet might be lost in a time scale estimated by Szabó et al. (2024) to be between 1 000-10 000 years. Instead, distant planets, having a larger Hill sphere, can keep their satellites up to time scales of 1-10 Gyrs or more.
In realistic moon-planet systems, due to outside perturbations, the satellite can escape even if its orbit is inside but close to the Hill radius, so the f factor introduces a more realistic reduced Hill radius. Domingos et al. (2006) found that for a satellite in prograde orbits $f = 0.4895$, while in retrograde orbits $f = 0.9309$. However, more recently, Rosario-Franco et al. (2020) found that for a prograde satellite, the value reduces to $f = 0.4061$.

When studying the long-term stability of a satellite around an exoplanet, it is important to keep into account also the mutual perturbations induced by the other objects in the system. For example, other satellites orbiting the same parent planet might compromise the stability of a moon's orbit. Additionally, the presence of other planets in the system could perturb the orbit of the host planet, which in turn impacts the orbit of its exomoon. Perturbations from the host star on the planet and its companion are also significant and can sometimes bring instability. However, studying the long-term stability of these multiple systems is challenging because it requires solving an N-body problem with $N > 3$, which is currently only possible for a few particular configurations.
Dobos et al. (2021) analyzed the evolution of a simple three-body system composed of a star, a known exoplanet and a satellite along the lifetime of the star to understand the long-term stability of the moon's orbit. They found that satellites do not survive around most of the close-in planets (with orbital periods of less than 10 days) over the star's lifetime. However, for exoplanets with orbital periods between 10-300 days, the survival rate increases to 70%. This means that satellites around close-in exoplanets, which are easier to detect with current detection methods, tend to escape or be tidally disrupted. This might be a possible explanation for the lack of exomoons discoveries so far and provides a hint for our future observations.

2.4 Satellites habitability

Since the discovery of the first exoplanet, one of the main goals of the research in this field has been to find habitable worlds. In particular, astronomers are searching for an Earth-like exoplanet around a Sun-like star in the habitable zone (HZ). The HZ is the region around the central star where an exoplanet could potentially host liquid water. These boundaries are based on the concept of liquid water on Earth and then generalized for all the other systems. It is important to note that the presence of liquid water on an exoplanet is a necessary but not sufficient requirement to allow extrasolar life as we know it. Other important considerations that should be taken into account when evaluating the habitability of an exoplanet include the presence of particular elements or molecules (like O_2, CH_4 and CO_2), the presence of an atmosphere and capability to retain it, the presence of internal and external sources of energy like tidal heating or heat flux from young planets, the presence of a magnetosphere that protects from stellar winds, persistence of climatic stability, and many other factors that indicate the presence of life on Earth (Teachey (2024)).
However, the search for habitability should not be restricted only to exoplanets but should also include habitable exomoons. In our Solar System, some moons of the giant planets, such as Europa around Jupiter and Enceladus around Saturn, might host liquid water underneath their surface, making them potentially habitable worlds. This liquid water is not due to their position in the HZ of the Sun, but rather because of their internal heating caused by tidal energy injected by their host planets. This tidal heating could be in the form of volcanoes, like those on Io, or geysers, like on Europa and Enceladus. Therefore, even exomoons, if present, might be located at a particular distance from their parent exoplanet that allows the presence of liquid water even if the exoplanet itself is further out of the HZ of its host star. Nevertheless, it should not be excluded that giant planets in the habitable zone of their star might host potentially habitable exomoons. Keeping these factors into account, the possible lower limit for a satellite's mass to be considered habitable is 0.12-0.23 M_E (Kaltenegger (2010)).

2.5 Detection techniques

There are several methods adopted for the detection and study of satellites (Teachey (2024); Heller (2018); Barr (2016)). Some of the possible signatures of exomoons which can help us detect them are listed below.

- Direct IR observation may reveal the presence of a young satellite by its thermal emission around a young giant exoplanet, but the angular separation of the planet-satellite system will be much smaller and difficult to resolve;
- In an unresolved exoplanet-exomoon system the analysis of the combined SED can give information about tidally heated satellites;
- The analysis of the interaction of the satellite with the magnetosphere of the exoplanet can produce detectable radio emissions;
- The gravitational influence of the satellite on the exoplanet can be analysed spectroscopically in the reflex motion (Vanderburg et al. (2018); Ruffio et al. (2023), see chapter 4);
- Exomoons can be unveiled through microlensing light curves of a background source when the lens system (planet+moon) crosses close to it and amplifies its luminosity. Modelling the caustics and the light curves can give us the masses and architectures of the lens system;
- Pulsar timing can give a very precise calculation of the variation in the time-of-arrival induced by a satellite. This was also the method used for the first unofficial discovery of an exoplanet around the millisecond pulsar PSR1257 + 12 (Wolszczan & Frail (1992));
- In particular configurations of the system, it is possible to see the transit of the satellite in front of the exoplanet and/or of the star, which induces variation similar to that of the exoplanet transiting the star but shallower;
- TTVs, TDVs and TRVs are variations respectively in time, duration and radius induced by the satellite around the exoplanet when it transits the star.
- Photometry could detect volcanic or cryo-volcanic activity on the satellite in the form of deep transit at specific wavelengths. As a result, the exoplanet would seem larger than expected from its mass (Oza et al. (2019a)).
- It is also possible to study either the Rossiter-McLaughlin effect induced by an exoplanet-exomoon system transiting in front of a rotating star or the Rossiter-McLaughlin effect of an exomoon transiting in front of its host planet;
- Multi-band observations can help disentangle the signal of the satellite.

If a planet is directly detected, we can think of using the methods originally developed to search for exoplanets around stars for the hunt of exomoons. This is done by replacing the star with the exoplanet and the exoplanet with the satellite. In this case, we can retrieve the indirect effects that a satellite induces on its exoplanet using transits, radial velocities and astrometry techniques. In my thesis, I focused on the radial velocity method applied to exoplanets revealed with direct imaging which is discussed in Chapter 4. In the following, instead, I will briefly describe some other promising techniques used to detect

exomoons such as TTVs and TDVs (Kipping (2009)), microlensing, and the Rossiter-McLaughlin effect. Each of these techniques is sensitive to different characteristics both of the satellite and of the exoplanet hosting them, like the mass ratio or the satellite's semi-major axis.

2.5.1 TTVs and TDVs

When a satellite is transiting in front of either the host exoplanet or the star, it can cause a reduction in the observed light, providing photometric information about its presence. Since the radius of a satellite is typically small, these flux variations can be hard to detect and may be lost in the noise. One possible solution is to fold multiple transit light curves of the same planet and obtain a single, phase-folded light curve with a higher S/N. This technique is known as the Orbital Sampling Effect (Heller (2014)) and is very useful for detecting small satellites or identifying a population of satellites.
It is also convenient to analyze the gravitational perturbation indirectly induced by the satellite during the transit of its host exoplanet in front of the star. These perturbations are called Transit Timing Variations (TTVs) and Transit Duration Variations (TDVs) and rely on the transit method. Both variations are proportional to the mass ratio of the perturber, M_s/M_p, which can be a satellite orbiting the exoplanet or a secondary exoplanet orbiting the same star. Moreover, TTVs can also depend on the presence of small resonances (1:2 or 2:3). For these methods the observation of a single orbit is not sufficient for the detection. At least three transits are needed to measure a periodic change (Barr (2016)).
TTVs (Transit Timing Variations) are caused by a tangential offset of the planet from the exoplanet-exomoon barycenter and this produces a non-periodic transit with variation in the mid-transit time because the exoplanet transits before or after the barycenter of the system. These variations are of the order of seconds or minutes and the amplitude is proportional to $(M_s/M_p)(a_s/a_p)$, the ratio between the satellite's and the exoplanet's masses and the scaled semi-major axis.

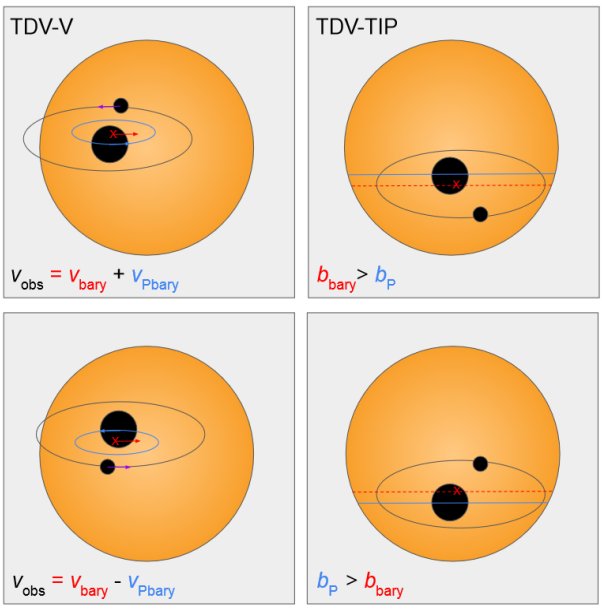

Figure 2.1: On the left an illustration of the geometry that results in TDV-Vs. on the right an illustration of the geometry that results in TDV-TIPs. Source: Teachey (2024) (fig. 3).

TDVs (Transit Duration Variations) are caused by the presence of the satellite that either changes the planetary velocity with respect to the barycenter (TDV-V) or changes the orbital inclination, hence the impact parameter b, of the exoplanet-exomoon system (TDV-TIP). In the first case, the planet appears to transit the star faster or slower based on the configuration and the barycenter will have a fixed and periodic transit (see left Figure 2.1). In the other case, the planet will be vertically offset with respect to the barycenter. The amplitude of the TDV is proportional to $(M_s/M_p)(a_s/a_p)(P_p/P_s)$, the ratio between the satellite's and the exoplanet's masses, the scaled semi-major axis and the ratio between the two orbital periods (see left Figure 2.1).
The period and the semi-major axis are related by the proportionality $P^2 \propto a^3$, which means that the amplitude of the TDV results $\propto a$. Since TTV scales like $M_s\, a_s$ and TDV scales like $M_s\, a_s^{-1/2}$, satellites close to the planet will have larger TDVs but smaller TTVs, while those farther out will have smaller TDVs but larger TTVs. Thus, both effects can only be detected for satellites at a certain intermediate distance from their host planet.

TRVs (Transit Radius Variations) happen when the satellite transit and the exoplanetary transit coincide. Rodenbeck et al. (2020) proposed the measurement of transit radius variations to reveal the presence of exomoons. When fitting a planet's transit to a model, which might be contaminated by an undetected companion, the effective planetary radius will change from epoch to epoch. To solve this problem the observer should let the planet's radius in each epoch as a free parameter.

Although these techniques in principle look really promising, to date there are just two, not yet confirmed, candidates coming from photometric studies. However, as discussed in the previous Section (2.3), planets closer to their star, which are ideal targets for the transit technique, are less favoured to host satellites because of their smaller Hill radius and the stronger tidal forces from the host star.

2.5.2 Rossiter-McLaughlin

Another method is the Rossiter-McLaughlin effect (Zhuang et al. (2012); Gaudi & Winn (2007); Ruffio et al. (2023)), a spectroscopic phenomenon that occurs when a satellite transits in front of its parent star, distorting the typical radial velocity due to the stellar rotation. A rotating star has one hemisphere that is blue-shifted, rotating towards us, and another one that seems red-shifted, rotating away from us. When a planet passes in front of the star, it will block part of the blue-shifted light first, then part of the red-shifted light, resulting in a spectral shift over time. If we observe, instead of an exoplanet, an exoplanet-exomoon system, we may see multiple shifts, some induced by the exoplanet and others by the satellite transiting the two hemispheres.

Observing these types of effects is more time-consuming and needs more resources than transit photometry, but it can give us valuable information about the architecture and dynamics of the system, such as the inclination and the direction of the orbit (see Figure 2.2). In addition, when the exoplanet is directly detected and resolved from the star the Rossiter-McLaughlin effect can be applied directly to it considering the exoplanet-exomoon system, where the exoplanet is rotating and the exomoon, transiting in front of the former, produces spectral shifts in the exoplanetary spectrum.

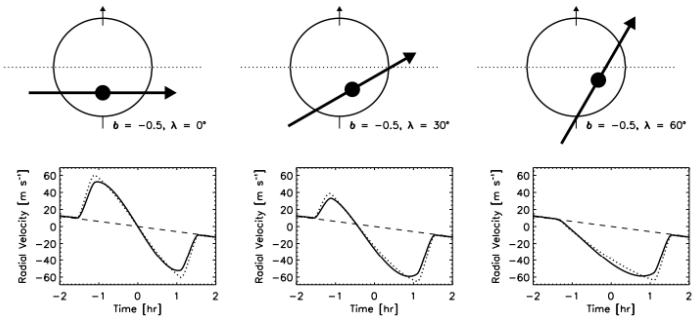

Figure 2.2: Illustration of the three different possible trajectories of a transiting exoplanet passing in front of the star, along with the corresponding Rossiter-McLaughlin waveform. Source: Gaudi & Winn (2007) (fig. 2).

2.5.3 Microlensing

The microlensing technique studies the light coming from a background star deviated and amplified by the passage of a foreground lens system. This lens system might be a triple star-planet-moon system as suggested by Liebig & Wambsganss (2010), or a free-floating planet-moon system as proposed by Sajadian & Sangtarash (2023). The deviated light results in a ring-distorted image whose radius depends on the total mass of the lenses and the projected distance between the light source and the lens. This radius is known as the Einstein radius and it is given by the equation:

$$\theta_E = \sqrt{\frac{4GM}{c^2}\frac{D_{LS}}{D_L D_S}}$$

where M is the total lens mass, D_{LS}, D_L, D_S are the distance of the lens system from the source, the distance of the lens system from the observer and the distance of the source from the observer, respectively. G is the gravitational constant and c is the speed of light. In general, the outcome of the passage is a bump in the light curve caused by a temporary magnification of the background source. The bump properties reflect the caustic-crossing configurations and the relative distance between the observer and the magnified system. By modelling the caustics, it is possible to determine the masses and architectures of the transiting lens system. The efficiency of the Roman telescope in detecting moon-induced perturbations has been evaluated by Sajadian & Sangtarash (2023) to be around (0.002-0.094)%.
With respect to the transit technique, microlensing can detect smaller M_s/M_p ratios, with current instruments. However, these events are unpredictable, unrepeatable, and short-lived, making it difficult to obtain a detailed characterization of the system, especially when the system is composed of an exoplanet and an exomoon and the level of precision needed is much higher.

2.5.4 New techniques

Besides these main techniques for the detection of exoplanets and exomoons, new techniques are being explored for the search of satellites, such as spectroastrometry (Agol et al. (2015)) and molecular mapping (Sparks & Ford (2002)).
Spectroastrometry consists of precisely measuring the position of the photocenter emitted

from an unresolved planet-satellite system for each wavelength of a spectrum and evaluating the differences in the light emissions. First, the planet-satellite system is directly imaged utilizing a coronagraph to suppress the starlight, then the planet and its satellite are assumed to emit energy with different spectra, causing the position of the light centroid to vary depending on the wavelength. This change provides insight into the planet-moon physical separation and with more than one observation, the two spectra could be disentangled, allowing for compositional characterization of the system. Similar to the transit technique, larger mass ratios are preferred for detection and characterization, but this technique is useful for exomoons orbiting far from their planet (Barr (2016)).
Molecular mapping, on the other hand, couples AO instruments with high-resolution spectrographs and disentangle the satellite's contribution from the giant exoplanet or brown dwarf spectrum. CRIRES+ is an optimal instrument for this innovative technique (Follert et al. (2014)). With this method, researchers can obtain the spectral characteristics, atmospheric composition and potential biomarkers of the satellite (Sparks & Ford (2002)).

2.6 Candidate companions

As of today, no official satellites have been confirmed, but some promising candidate companions have been proposed. Here below is a list of some of the main systems of interest detected either directly or indirectly through different techniques, taken from the article of Teachey (2024).

- **MOA-2011-BLG-262**: Bennett et al. (2014) detected with the microlensing technique a system of only two objects that they defined as a "free-floating exoplanet-exomoons system". The system is composed of a primary lens mass of $\sim$4 M_J and a sub-Earth mass exomoon. This discovery proved the capability of the microlensing technique to be sensitive to low-mass objects and thus satellites. However, this system could also be interpreted as a stellar primary orbited by a BD secondary companion. Unfortunately, microlensing events are not repeatable and unpredictable, so the confirmation of the nature of this system cannot be done with precision and remain undefined;

- **OGLE-2015-BLG-1459L**: Hwang et al. (2018) identified a second microlensing event. The event suggests the presence of 4 objects but with three possible configurations: a triple-lens system of planet-moon-star with only one source (3L1S); a binary lens, composed of a BD and a Neptune-mass planet, and two sources (2L2S); or one lens object and a triple-star source (1L3S). They concluded that the third scenario is the most favoured;

- **Kepler-1625 b**: Teachey & Kipping (2018) identified this transiting planet to be a potentially large exomoon host. This configuration explains the data very well, but to confirm the presence of an exomoon another transit observation with HST is needed. They claimed this presence based on a TTV with an amplitude of around 22 minutes. These TTV signals could either be explained by an exomoon or a secondary planet orbiting the star and not yet detected. The hosted exomoon would have a size similar to Neptune and it is named Kepler-1625 b-i, but its existence has been recently disputed (Heller & Hippke (2024));

- **MOA-2015-BLG-337**: Miyazaki et al. (2018) attributed a microlensing event to

either a BD, or a planet, with a Neptune-like satellite, or to a binary system of BDs. They concluded that the first scenario is slightly favoured but not confirmable.

- **WASP-49 b**: Oza et al. (2019b) studied 14 Hot Jupiters searching for volcanically active exomoons (like Io around Jupiter) that might be detected indirectly thanks to absorption by atmospheric gases during the exoplanet's transit. They proposed WASP-49 b as a possible host of an "exo-Io" which presented deep sodium (Na I) absorption lines. The critical factor is the vicinity of the exoplanet with its parent star and the fact that also other models could fit the data, such as a high-altitude thermosphere and atmospheric escape;

- **DH Tau B**: Lazzoni et al. (2020) proposed a 1 M_J candidate companion of the low-mass brown dwarf DH Tau B at 10 AU. The results were retrieved by applying the negative fake companion technique to SPHERE observations in the H and K bands. This technique suppresses the source star flux and analyses the residuals to search for fainter companions. Trying to confirm the presence of the companion they also observed the system in the L'-band with LMIRCam/LBT, but without significant detections. Therefore, at such wavelength, they were able to determine only an upper limit for the companion mass (2.6 M_J);

- **2MASS J11193254–1137466 AB**: Limbach et al. (2021) studying the light curves of this isolated planetary mass object (IPMO) found an event that could be due to the transit of a 1.7 $R_\oplus$ companion. IPMO might be the result of an ejection from their natal stellar system and Hong et al. (2018) found that satellites orbiting around them have $\geq 50\%$ chance of surviving. However, these transit variations are suitable with other scenarios and further observations are necessary;

- **Kepler 1708 b**: Similar to Kepler 1625 b-i, Kipping et al. (2022) proposed the presence of a secondary companion around the transiting Kepler 1708 b. This planet has approximately the mass of Jupiter and has an orbital period of 737 days. The candidate exomoon would have a radius of around 2.61 $R_\oplus$, which results in a very large object. However, the size could be influenced by the limitations of our observational instruments, similar to the biases seen with exoplanets. In this scenario other models were ruled out by Kipping et al. (2022) but to confirm the presence of a transiting exomoon a radial velocity analysis is needed to exclude false positives. As of today, only two transits of Kepler 1708 b have been observed, and at least one more observation is necessary to analyze TTVs and obtain an independent dynamical test for this hypothesis. Like Kepler-1625 b-i, also Kepler-1708 b-i has been disputed recently by Heller & Hippke (2024).

Besides these candidate companions, there is also a study of Pearson & McCaughrean (2023) on isolated planetary-mass objects (IPMO) in stellar forming regions, such as the Orion Nebula and Trapezium Cluster. IPMOs are objects with masses below 13 M_J, hence they are faint and most of the time difficult to observe. These forming regions provide the best conditions to look for them. They concluded that 9% of the discovered planetary-mass objects are in a wide binary opening a completely different view on both star and exoplanet's formation scenarios.

Chapter 3

Selection of the catalogue

My search of satellites, including exomoons and more massive companions, using the radial velocity technique, started by selecting the most suitable targets among the directly imaged exoplanets and brown dwarfs discovered so far. The focus of this study is on young, self-luminous, and well-separated exoplanets or brown dwarfs that have been directly imaged. These objects are ideal for this type of research because they are located far from their host stars and emit more energy because of their ongoing gravitational contraction. By directly imaging these planets, it is possible to resolve them from their host star and obtain their planetary spectra. From these spectra, applying the radial velocity method, we can search for Doppler shifts in the planetary lines that might indicate the presence of satellites. In particular, this work employs the CRIRES+ and HiRISE instruments, which can provide spectra with a high enough resolution to detect exomoons or binary planets, if present.

The final results of the selection process are reported in Tables 3.2, 3.3, 3.4, and 3.5, where the main properties of exoplanets and their relative host stars are listed. Specifically, Table 3.2 contains the key characteristics of directly imaged exoplanets and brown dwarfs suitable for spectroscopic analysis with CRIRES+, and Table 3.3 lists the main parameters of their parent stars. Similarly, Table 3.4 contains the key characteristics of directly imaged exoplanets and brown dwarfs suitable for spectroscopic analysis with HiRISE and, finally, Table 3.5 lists the main parameters of their parent stars.
In this chapter, the first Section illustrates the sources from which the planets and host stars' properties were retrieved. Section 3.2 describes the selection process by which the Tables were improved and reduced. Section 3.3 reports a general description of the final catalogue and the rejected objects. Finally, Section 3.4 describes the main characteristics of the two instruments that will be used in the follow-up analysis.

3.1 Sources

Tables 3.2 and 3.4 were developed by collecting exoplanets data from two main catalogues: the NASA Exoplanet Archive[1] and the Exoplanet.eu catalogue[2], along with the information about their host stars (updated to April 2024). The two catalogues have different inclusive criteria. The NASA catalogue lists all planets with estimated mass

[1] https://exoplanetarchive.ipac.caltech.edu/
[2] https://exoplanet.eu/catalog/

(or minimum mass) equal to or less than 30 M_J, with the planet's properties present in the peer-reviewed literature, and with sufficient follow-up observations proving that the object is not a false positive or unlikely to be one (Akeson et al. (2013)). On the other side, the European catalogue lists all the detections and data announced by professional astronomers on exoplanetary systems with objects lighter than 60 M_J orbiting stars or free-floating. It also provides a database on exoplanets in binary systems, a database on circumstellar discs, and an exhaustive bibliography.
All magnitudes of parent stars and brown dwarfs were retrieved from SIMBAD[3], then the values of Δm_H and Δm_K in Tables 3.3 and 3.5 were calculated by subtracting the star's magnitude from the planet's magnitude in the same band. When possible, the missing information from catalogues were filled in by consulting specific papers on each planet, which are referenced in the column titled *"Reference"*.
The information about the main instrumental parameters of CRIRES+ and HiRISE, which helped the association of one of them to each planet for the follow-up analysis, were retrieved from the official user manual of CRIRES+ (Dorn et al. (2023)), the ESO website[4], from Vigan et al. (2024) and from Otten et al. (2021). In particular, the criteria that distinguished the two instruments in the association of one, rather than the other one, to each planet are illustrated in Section 3.4.3.

3.2 Selection

After collecting all the available information for each planet, I selected only those suitable for radial velocity follow-up analysis with CRIRES+ and HiRISE. It is important to underline that the selection is based on the properties and capabilities of the instruments adopted in this project. If the study had adopted different instruments, the selection would have been different. In particular, as discussed in more detail in Section 3.4.2, HiRISE couples the AO of SPHERE with the CRIRES+ spectrograph. To ensure the highest level of precision for both instruments, I rejected all planets with an angular separation greater than 10" since this is the maximum slit length of CRIRES+ (see Table 3.1) which is also the limit used by HiRISE.
Additionally, I excluded all planets around host stars with a Gaia magnitude fainter than 12 mag, which is the star's apparent brightness as measured by the Gaia space observatory, a mission of the European Space Agency (ESA). The 12-mag limit was chosen because it roughly corresponds to the operating limit of SPHERE AO. The magnitude limit of MACAO, CRIRES+ adaptive optics system, was fainter (see Section 3.4.1, $R < 15$), so I adopted the more restricting value between the two.
Finally, I neglected all planets with a value of the declination coordinate greater than 25°, because those objects were located near or below the horizon and observing them from VLT latitudes would be difficult and would degrade the adaptive optics functions. As mentioned in Section 1.4.1 suitable instruments are, or are becoming, available also in the northern hemisphere, such as NIRSPEC and KPIC at Keck. These are not considered in the thesis, as I am focusing on instruments to which the Italian astronomical community would have direct access.

[3] https://simbad.u-strasbg.fr/simbad/sim-basicIdent=m33&submit=SIMBAD+search
[4] https://www.eso.org/sci/facilities/develop/instruments/crires_up.html

3.3 Catalogue

After the selection, the final catalogue comprises a total of 44 directly imaged exoplanets and BDs suitable for the radial velocity analysis. Their main characteristics are reported in Tables 3.2 and 3.4. Based on the criteria noted in Section 3.4.3, 27 of them were primarily assigned to CRIRES+, while the other 17 were assigned to HiRISE.
The selection process started with a total of 107 objects retrieved from the two catalogues (68 from the NASA archive and 39 from the European archive), 46 among them were rejected based on the selection criteria reported in Section 3.2. The remaining 61 objects were singularly analyzed to understand if they were feasible for the purposes of this project. Among them, 17 systems presented very particular configurations that would have needed a different and more specific analysis. They were rejected for reasons which are reported below, however, they could be studied individually in future works:

- HIP 81208 C b rotates around the star HIP 81208 C within a hierarchical quadruple system with three stars (Chomez et al. (2023));

- Lkca 15 b and c (Andrews et al. (2011)), HD 100546 b (Pineda et al. (2019)), HD 169142 b (Law et al. (2023)) and PDS 70 c (Benisty et al. (2021)) are planets around very young stars (age<10 Myrs) in which the disc is not yet dissipated and the observations might result challenging. The main aspects of CPDs are described in Section 1.6.1 and in principle they are very interesting in the search of exomoons and binary companions but would require specific observations and analysis for every single system;

- CFHTWIR-Oph 98 b is a 7.8 M_J planetary companion around a young low-mass brown dwarf (Fontanive et al. (2020));

- WISE J121756.91 + 162640.8 AB (Liu et al. (2012)), WISE J033605.05 - 014350.4 AB (Calissendorff et al. (2023)), CFBDSIR J145829 + 101343 AB (Liu et al. (2011)) and 2MASS J22062280 - 2047058 AB (Konopacky et al. (2010)) are binary systems composed by two brown dwarfs; In principle, isolated systems such these are fascinating objects for the radial velocity analysis since the contamination of the secondary companion is largely reduced, however, the secondary companion result too faint for the AO system and it will be difficult to apply this technique with the precision needed;

- L2 Pup b is a planet that rotates an AGB (Asymptotic Giant Branch) star. AGB stars have ongoing He fusion in the inner shell and H fusion in the outer shell, surrounded by a convective envelope (Kervella et al. (2016));

- HIP 79797 Ba and Bb is a close binary brown dwarf system orbiting the primary star, HIP 79797 A (Nielsen et al. (2014));

- TWA 5B is a brown dwarf companion in a young triple system that rotates around a pair of low-mass stars, TWA 5Aa-b (Köhler et al. (2013)); HIP 79098 AB b was rejected for the same reason;

- b Centauri (AB) b is an 11 M_J exoplanet in a circumbinary orbit around a binary star system (Janson et al. (2021)).

3.4 Instrument

3.4.1 CRIRES+

The upgraded CRIRES is a CRyogenic high-resolution InfraRed Echelle Spectrograph, developed by ESO (European Southern Observatory). It is located at the Nasmyth B focus of UT3 on the Very Large Telescope (VLT) at ESO's Paranal Observatory in Chile (Dorn et al. (2014); Dorn et al. (2023)).
The optical layout of CRIRES after the upgrade is shown in Figure 3.1.

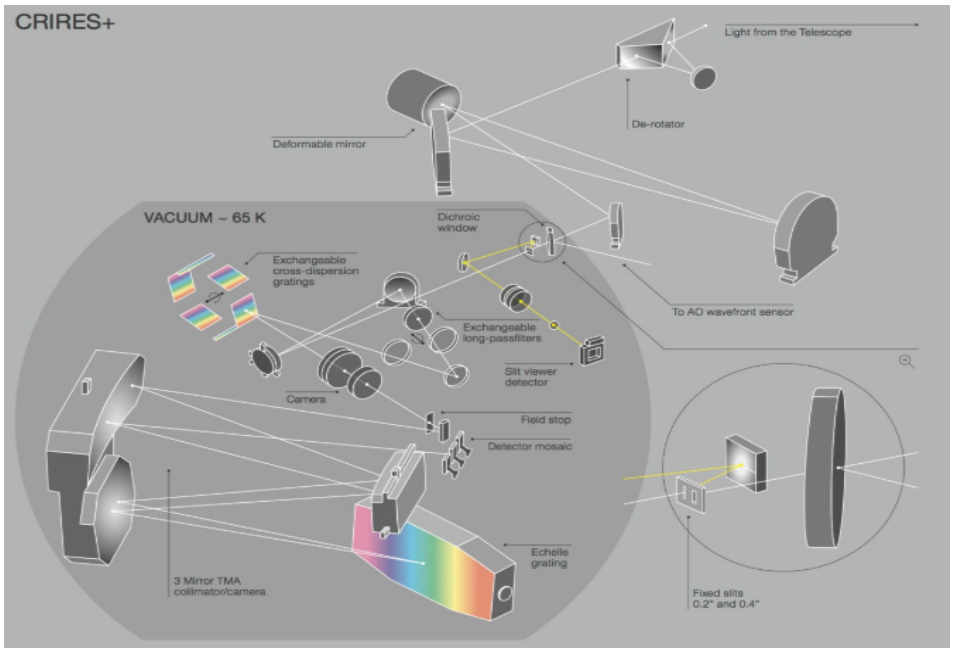

Figure 3.1: Optical layout of the new cross dispersion pre-optics CRIRES+. Source: CRIRES+ official User Manual (fig. 1).

Spectrograph characteristics

Any object that absorbs or emits light can be studied using a spectrograph to determine its characteristics, such as temperature, chemical composition, and rotational velocity.

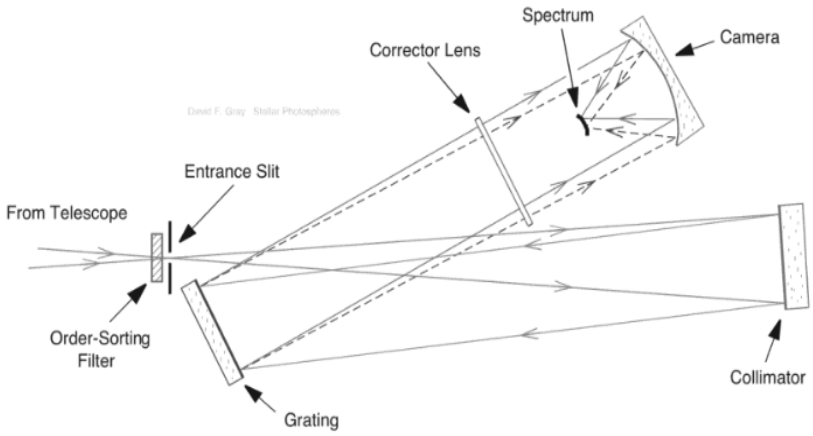

Figure 3.2: The optical layout of a typical spectrograph. Source: Gray (2005), (fig. 3.1).

A spectrograph is an instrument that collects and analyzes the light from a selected target. A schematic representation of the structure of a spectrograph with a reflection grating is shown in Figure 3.2 (Gray (2005)).
This instrument separates light into its different wavelengths and records the final spectrum. The five basic components of an astronomical spectrograph are the slit, collimator, grating or prism, camera and detector. Each of these objects is described below.
When the light enters the spectrograph, it passes through the *slit*, a narrow rectangular aperture mask located in the focal plane of the telescope. For example, CRIRES+ has two slit widths, one of 0.2" and the other one of 0.4". The slit helps isolate the region of interest in the sky because only the light that falls through it enters the spectrograph. Without it, the source spectra or additional sky background on either side of the target would overlap, contaminating the target spectrum and degrading its signal to noise ratio. Moreover, the slit provides a stable spectral resolution because the spectrum consists of an infinite number of images of the telescope focal plane, each shifted slightly in wavelength. Hence, without the slit, a star's spectral resolution would depend on seeing conditions, which change over time.
Exiting the slit, the light encounters the *collimator*, which can be either a lens or a mirror. The collimator takes the diverging light from the slit, makes it parallel, and directs it towards the grating. The light beams need to be parallel because if they hit the grating at different incidence angles, the same wavelength of light in the same order would appear at different positions on the detector and produce blurring into the final spectrum.
After this, the diffraction element, which is either a transmission or reflection *grating* or a prism, splits the light into its wavelength component, similar to how raindrops create a rainbow. By changing the angle of the grating with respect to the incoming light beam, the angle of the diffracted beam will change. This is why most spectrographs have tilting gratings that can adjust the starting and ending wavelengths of the spectrum.
These dispersed beams of light are then converged by the *camera* into the *detector*, creating the final spectrum. The camera can be either a lens, mirror, or catadioptric system. The detector is composed of a two-dimensional array of pixels that records a spectrum and the most utilized one is the CCD (Charge-Coupled Device). Finally, astronomers can analyze the pattern of the spectrum to identify atoms and molecules present in the target and understand the various physical and chemical properties of the source.

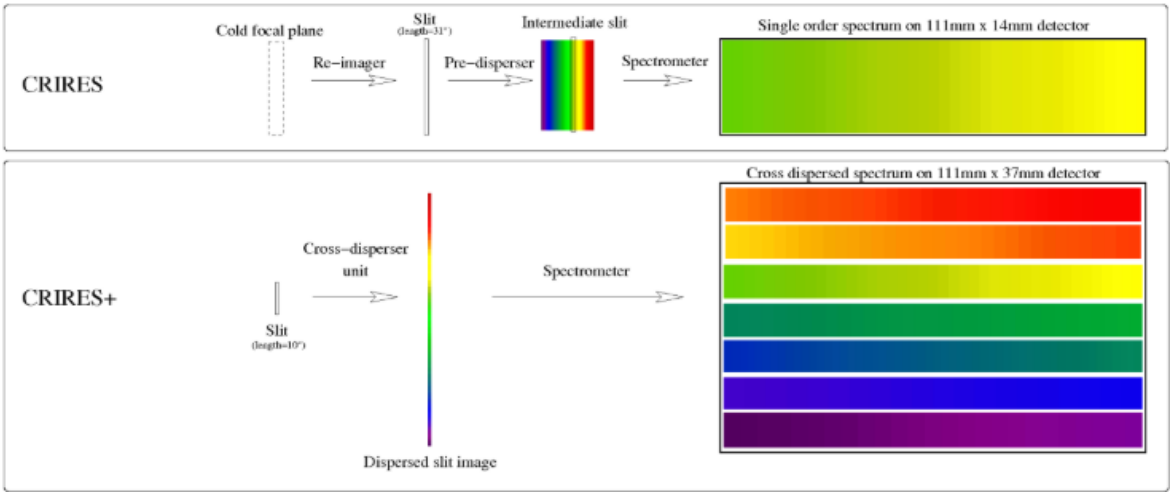

Figure 3.3: Schematic diagram summarizing the spectrograph differences between CRIRES and CRIRES+. Source: CRIRES+ official User Manual version P114.2 (fig. 3).

First of all, CRIRES+ is a high-resolution spectrograph. While low-resolution spectrographs measure broad continuous spectra, high-resolution spectrographs measure the fine details of the spectral lines, allowing them to resolve narrow spectral features with great precision. High-resolution spectroscopy has several advantages in the study of exoplanets. For example, it can analyze line shapes, widths, and shifts, which provide insights into the atmospheric, temperature, and chemical compositions of the target. Moreover, it allows for the characterization of an exoplanet's orbital motion and mass by studying the Doppler shifts in the star's spectral lines.
Furthermore, CRIRES+ operates in the IR wavelength range (0.95-5.3 μm), making it ideal for studying molecular absorption features in atmospheres of very cool star and substellar objects.
Lastly, the upgraded version of CRIRES is a Cross-dispersed Echelle spectrograph. An echelle spectrograph is characterized by high angular dispersion (with orders of $n \sim$100) and typically achieves a resolving power of R>40 000. When two orders overlap, this is resolved using a cross disperser, which is a low-resolution grating or prism positioned perpendicular with respect to the main grating, that disperses light in multiple directions. The advantage of using an echelle spectrograph is the broader wavelength coverage obtained in a single exposure, which is a powerful characteristic when analyzing radial velocity variations.

Updgrade

CRIRES+ is an upgraded version of the CRIRES spectrograph, that worked on the VLT for eight years and achieved great scientific results. CRIRES setup consisted of a single-order spectrograph that provided long-slit (40") spectroscopy with a resolving power of 100 000. However, this setup was limited to a narrow, single-exposure spectral range, resulting in low observing efficiency. The upgrade turned CRIRES into a cross-dispersed echelle spectrograph expanding the simultaneously covered wavelength range by a factor of ten while maintaining the CRIRES wavelength coverage (0.95-5.3μm) at a spectral resolution of 100 000. As shown in Figure 3.1, the cross-dispersion in CRIRES+ is performed using six reflection gratings mounted on a cryogenic wheel, each optimized for operation in a specific wavelength band (Y,J,H,K,L and M). With this configuration, only 29 different settings of grating angles are required to cover the $YJHKLM$ band for CRIRES+, compared with 280 settings needed by CRIRES, even if some small wavelength gaps cannot be covered (1356-1423 nm, 1854-1908 nm, and 2527-2725 nm). Other main upgrades include new custom-made absorption gas cells, for the advanced wavelength calibration module, a new large state-of-the-art detector with 5.3 μm cut-off wavelength, and a new spectropolarimetry module that allows the recording of circular and linear polarized spectra.

CRIRES+ includes both a spectrograph and an adaptive optics system. As mentioned earlier, the spectrograph's application is adopted to separate light into its components for detailed analysis and to study the exoplanetary spectrum at high resolution retrieving information from different elements. Instead, the adaptive optics system, known as MACAO (Multi-Applications Curvature Adaptive Optics), uses a reference star to measure and correct the atmospheric distortions of the image adopting a deformable mirror. MACAO improves clarity by providing diffraction-limited images at the focal plane, enhancing sensitivity by about a factor of two for point sources and correcting up to 1000 frames per second. This results in sharper images and better target light concentration

into the slit, which improves the signal to noise ratio of the observations.
A summary of the new and main instrument parameters is given in Table 3.1.

Spectral resolution	∼50 000 and ∼100 000
Wavelength coverage	0.95-5.3 μm ($YJHKLM$ bands)
RV precision goal	∼3 m/s
Slit length	10”
Slit width	0.2” and 0.4”
Polarimetry	linear + circular ($YJHK$ bands)
Adaptive optics	60 actuator curvature sensing
Cross-disperser	6 gratings
Focal plane	6144 × 2048 pixels (Mosaic of three H2RGs)

Table 3.1: Summary of the new and main instrument parameters in CRIRES+. Source: Dorn et al. (2023) (Table 1).

Goals

With these improvements, the instrument aims to search for super-Earths in the habitable zone (HZ) of low-mass stars, where planets that might support life are more likely to be found. It can also be used to characterize the chemical composition of exoplanet atmospheres, study protoplanetary discs, and improve our knowledge of the origin and evolution of stellar magnetic fields. For this research project, the first three aspects are the most important.

Since the beginning, finding exoplanets in the habitable zone of low-mass stars has been the main objective in the search for extrasolar life. Currently, only 5% of detected planets orbit stars with masses less than about 0.5 $M_\odot$, even though M-dwarfs are the most common stars in our galaxy. These low-mass stars are especially interesting because they are cooler, and their HZs result closer to the star. Moreover, M-dwarfs and BDs have low effective temperatures, meaning they emit most of their energy in the IR wavelengths (1.0-2.5 μm), hence a high-resolution IR spectrograph is well-suited for this type of research. Thanks to the new gas absorption cell, CRIRES+ can reach a radial velocity precision of ∼3 m/s. This precision would enable the detection of super-Earth mass exoplanets in the HZ of M-dwarf stars in the solar neighbourhood. Moreover, this level of precision is useful in my research because it enables the study of low-mass BDs and exoplanets, which are cooler and fainter objects than stars, so it also opens up the possibility of searching for satellites around planets.

Like CRIRES, CRIRES+ is designed to provide a relatively high spatial, spectral and temporal resolution. It is mainly used for radial velocity analysis, to detect and study exoplanets, as well as for direct spectroscopic detection and characterization of exoplanet atmospheres. The original CRIRES was effective for the observation of close-in (a<10 AU), highly-irradiated planets that emit most of their light in the IR. In this spectral region, lines of molecular gases like CO, NH_3, CH_4 can be found, indicating the characteristics of exoplanetary atmospheres. CRIRES+ has extended its wavelength coverage into the L and M bands, allowing it to detect additional molecules like H_2O, OH, HCN, and CO, as well as several atomic hydrogen lines. These features will be used to study the envelopes and potential jets of protoplanetary discs, which can tell us their ability to form planets and their evolutionary status.

Performance

In general, CRIRES+ has a peak overall efficiency of approximately 15-25%, which is approximately 15% higher compared to the older version of CRIRES. Evaluating the performance of MACAO system of CRIRES+, the results present some gain in the fraction of energy available for the spectrometer in the J band and a significant increase (about twice as much) in the K and M bands with respect to the no AO mode. However, for seeing worse than 1.4", the AO correction becomes very poor and unstable and will not bring any improvements. Normally, the overall performance of the AO system depends on both the brightness and the distance of the natural guide star (NGS) from the science target. The AO NGS star should be as close as possible to the scientific target, better if closer than 10", ideally, it is the science target itself. If the NGS is bright (R<11) the distance can extend to 20-30" from the target. Due to limitations in the total amount of counts of the instrumentation and taking into account the best seeing conditions, the limit brightness of the AO star is R∼15 mag. Fainter stars will not improve the detection compared to without AO system. Thus, the allowed NGS magnitude range is 0.2<R<15.

For direct observations of planets in very good conditions and very low airmass (≤1.15) the flux level in the wings of the stellar PSF drops below ∼10% of the peak flux at an angular distance of ∼0.25" from the peak in the H-band, the band of interest of this thesis project. For larger airmass values the quality of the AO correction will noticeably degrade and the PSF profile will be broadened.

On the spectroscopic level, as anticipated before, the introduction of a cross-dispersed echelle spectrograph expanded the simultaneous wavelength coverage by a factor of 10 with respect to CRIRES but still presenting some gaps within a photometric band. The FoV of CRIRES+ is slit width×10" and CRIRES+ as two slit widths of 0.2" and 0.4". The 0.4" slit width will give almost maximal throughput in most AO observations but with lower spectral resolving power. The 0.2" slit width will give a maximum resolving power of ∼86 000, while the 0.4" slit width will give a minimum resolving power of ∼43 000. The estimated radial velocity precision is ∼3 m/s. By employing the short gas cell as a wavelength calibrator. For a S/N of 150 an RV precision of 4 m/s is obtained for a sequence of short exposures (20 sec) in the laboratory with the 0.2" slit. Instead on the sky, the highest radial velocity precision reached with CRIRES is 2.6 m/s for a 60 s total exposure time and a S/N ratio of 280.

3.4.2 HiRISE

In July 2023, the VLT was equipped with a new fibre-optics tool, HiRISE (High-Resolution Imaging and Spectroscopy of Exoplanets), that couples the high-contrast imaging (HCI) of SPHERE and the high-resolution spectroscopy (HRS) of CRIRES+ using single-mode fibres (Otten et al. (2021); Vigan et al. (2024)). This combination allows for the suppression of stellar noise, which is the main contributor of noise, by first spatially resolving the stellar and planetary PSFs through adaptive optics, then applying mid-to high-resolution spectroscopy (R=5 000-100 000) to improve the spectroscopic studies of exoplanets. HiRISE provides a unique system capable of characterizing directly imaged exoplanets. The following section describes its main features, goals, and overall performance compared to CRIRES+.

Characteristics

There are different scientific and technical requirements that HiRISE should accomplish to benefit the coupling:

1. It must enable the direct characterization of substellar companions at a significance level higher than 5σ with integration times shorter than one night. This has been proven by Otten et al. (2021) to be easily reached considering bright stars and faint companions;

2. It must be more efficient than CRIRES+ in standalone mode for the same science cases. Otten et al. (2021) proved that in the H band HiRISE is able to outperform CRIRES+ in certain conditions, while in the K band this requirement will not be satisfied. For numerical detail see Section 3.4.3;

3. It must provide access to the H band and, if possible, to the K band. The K band coverage condition in the final design is only partially satisfied;

4. It must not impact standalone instruments, or require any modification of the hardware used.

The system is divided into three distinct components:

- FIM (Fibre Injection Module): implemented in SPHERE;
- FB (Fibre Bundle): links SPHERE and CRIRES+ around the UT3;
- FEM (Fibre Extraction Module): installed in CRIRES+;

The FIM is installed in the IFS arm of SPHERE on a vertical board. The light from the IFS beam is redirected to the FIM using a pick-off mirror installed on a linear translation stage. Then a single lens re-images the telescope's pupil onto a mirror attached to a tip-tilt platform, with an accuracy of the order of 0.01 λ/D. The FIM includes also a near-infrared tracking camera that centres the planetary PSF on the science fibre. This camera is cooled down to -40°C to minimize thermal noise and avoid fan vibrations on SPHERE. All the optics of the FIM include anti-reflection coatings to optimize the overall transmission in the H band, which amounts to ∼90%.

The FB is a single piece of hardware that connects the science and calibration fibres from SPHERE to CRIRES+ with a total length of 83.9 m and it is divided into three sections: 2.5 m inside SPHERE, a long section of 78.2 m around the telescope, and the remaining 3.2 m inside CRIRES. The FB includes various fibres for the science and the calibrations, as shown in Figure 3.4. The science and calibration fibres used for HiRISE in the bundle are single-mode fibres (SMFs) from Coherent, model 1310M-HP. These SMFs provide a positionally and spectroscopic stable source at the entrance of the spectrograph that eliminates the modal noise and reduces the stellar halo contamination at the planetary level (Otten et al. (2021)). For science, the bundle has four fibres that go all the way from SPHERE to CRIRES+: the science one that samples the planetary signal at the centre of the FoV, and three reference fibres that sample the PSF of the star in the FoV. The other ones are for calibration or simply dummy fibres filling the geometrical patterns in the ferrules. These fibres offer a very low attenuation in the H band, less than 0.5 dB/km at 1.55 μm which translates into an expected transmission $\geq$0.989 for a 100 m fibre. Taking into account the coating, the FB transmits ∼95% of the light.

The FEM within CRIRES+ is a much simpler system than FIM with just a few optics to re-image the output of the science fibres. It is located in the calibration carrier stage of CRIRES+ at the entrance of the warm bench of the instrument, composed of the instrument derotator, the MACAO deformable mirror, and the MACAO wavefront sensor. Again, the system is optimized to maximize the transmission in the H band, with 90% transmission.

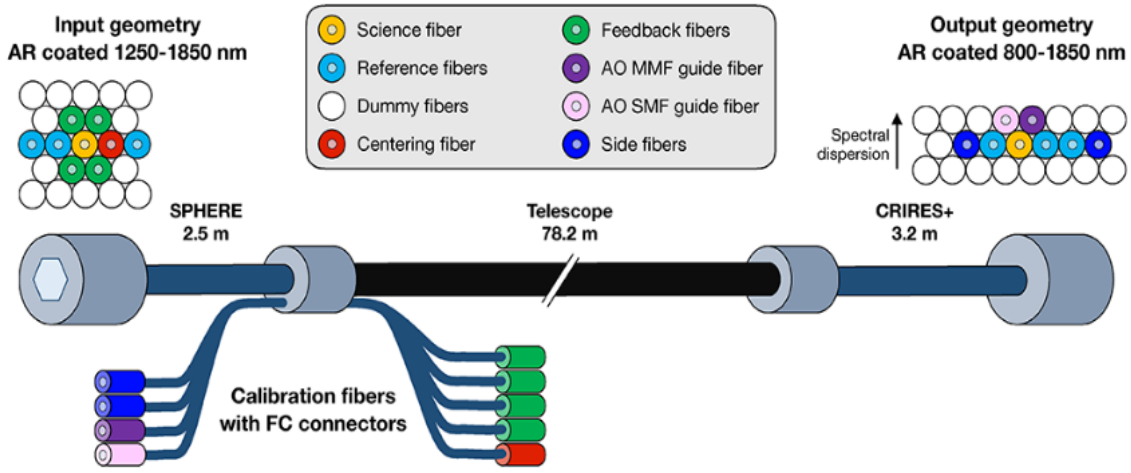

Figure 3.4: Conceptual drawing of the Fibre Bundle (FB). Source Vigan et al. (2024) (fig. 3).

Goals

The goal of HiRISE is to enable the characterization of known exoplanets in the H band with high resolutions (R=100 000) in a few hours of observing time. This helps us improve our knowledge of their formation scenarios, composition and evolution. While some atmospheric features of exoplanets can be detected at lower resolutions, others, such as looking for satellites (Ruffio et al. (2023); Lazzoni et al. (2022); Vanderburg et al. (2018)), require higher spectral resolutions for more precise measurements.

Performance

HiRISE is a NIR single-mode fibre bundle with at least four science fibres and injection and extraction optics that couple SPHERE and CRIRES+. As anticipated before, the optics in the FIM reduce transmission, with a 2% loss due to the lenses and a 5% loss from the dichroic. Considering there are six lenses, one mirror, and one dichroic in the injection optics, the total transmission factor is about ∼0.71. Regarding the transmissivity, to facilitate the installation and to reduce the risks, HiRISE is divided into three parts joined with connectors, each causing a loss of 0.15 dB that corresponds to a 2% loss from reflection at the fibre's input and output. Finally, the FEM has a transmission factor of approximately 0.8.

3.4.3 Comparison between CRIRES+ and HiRISE

The search of satellites around directly imaged exoplanets and BDs continued by assigning to each object of the catalogue an instrument between CRIRES+ (Table 3.2) or HiRISE (Table 3.4) based on its angular separation and contamination from the host star. The

division was based on the results by Otten et al. (2021) which analyzed the performance of HiRISE with respect to CRIRES+ as a function of the stellar magnitude and the planetary angular separation in the H and K bands.

In particular, Otten et al. (2021) concluded that:

- In general, HiRISE provides a substantial gain with respect to CRIRES+ in the H-band;
- For bright hosts, HiRISE largely outperforms CRIRES+ because of the high stellar contamination that CRIRES+ is not able to separate from the planetary flux;
- For hosts with H <8.5 and an angular separation between 50-350 mas from the exoplanets and hosts with H <7 and an angular separation between 50-700 mas from the exoplanet, HiRISE provides better performance than CRIRES+;
- For fainter hosts there are no significant improvements;
- For very small angular separations (<50 mas) both HiRISE and CRIRES+ are limited by the stellar photon noise, but CRIRES+ outperforms HiRISE because of its much higher transmission.

Main characteristics of planets suitable for CRIRES+ follow-up

Planet	a_P [AU]	R_P [R_J]	M_P [M_J]	ecc	i [°]	T [K]	Sp.T	H	K	ang. dist.	Reference
μ_2 Scorpii b	290	1.09	14.4	0.56	96.6	2200	-	-	15.99	1.709 ± 0.005	Squicciarini et al. (2022)
η Tel B	199.4	-	47	0.34	86	2600	M7.5V	11.93	13.2	4.214 ± 0.022	Lazzoni et al. (2022); Langlois et al. (2021)
GJ 504 b	43.88	1.16	4	-	-	510	T/Y	20.14	19.19	2.493 ± 0.003	Bonnefoy et al. (2018); NASA
HR 8799 b	68.16	1.2	5.8	-	28	1175	L	17.85	20.6	1.730 ± 0.005	Zurlo et al. (2022)
HR 8799 c	37.43	1.2	7.2	<0.5	28	1225	L	16.91	18.2	0.950 ± 0.005	Zurlo et al. (2022)
HR 3549 B	80	-	45	0.7	-	2350	-	10.24	-	0.850 ± 0.006	Mesa et al. (2016)
HIP 64892 B	159	2.3	33	-	-	2600	M9	14.11	16.3	1.273 ± 0.001	Cheetham et al. (2018)
HD 19467 B	51.1	-	67	-	-	978	T5.5	17.9	17.97	1.607 ± 0.007	Greenbaum et al. (2023); SIMBAD
HIP 65426 b	92.5	1.5	8	-	100	1500	L6	17.99	>21	0.830 ± 0.003	NASA
HIP 78530 B	710	-	23	-	-	2700	M8	14.39	18.4	4.533 ± 0.006	Lazzoni et al. (2020); NASA
HD 984 B	9	-	61	0.76	120.8	2730	M6.5	12.6	12.2	0.202 ± 0.001	Meshkat et al. (2015)
HD 106906 b	654.1	-	11	-	-	1820	L2.5	16.2	15.46	7.11 ± 0.03	Adams et al. (2023); NASA
AB Pic b	260	-	13	-	-	1800	L0	14.69	14.14	5.450 ± 0.014	Lazzoni et al. (2020); Chauvin et al. (2005c)
HD 284149 b	400	-	32	-	-	2537	M8-L1	14.715	14.32	3.681 ± 0.004	Bonavita et al. (2014)
CD-35 2722 B	67	-	31	0.82	126	1700-1900	L4-1	12.78	15.3	2.987 ± 0.003	Langlois et al. (2021)
YSES 2 b	115	-	6.3	-	-	1300	Late L-T	18.85	17.91	1.053 ± 0.005	Bohn et al. (2021)
GSC 08047-00232 b	277	-	13.8	-	-	2100	M9.5	15.45	14.75	3.207 ± 0.003	Chauvin et al. (2005a); Langlois et al. (2021)
TYC 8998-760-1 b	162	3	14	-	-	1727	L0	15.99	14.8	1.708 ± 0.003	Bohn et al. (2020a)
TYC 8998-760-1 c	320	1.1	6	-	-	1240	L7.5	19.81	17.96	3.369 ± 0.033	Bohn et al. (2020b)
GQ Lupi B	117	3.8	20	0.24	-	2700	M9	-	13.1	0.732 ± 0.003	Lazzoni et al. (2020)
CT Cha b	440	2.2	17	-	-	2600	M8	-	14.89	2.667 ± 0.036	NASA
GSC 06214-00210 b	320	1.8	14.5	-	-	2200	M9	15.52	14.87	2.206 ± 0.001	NASA
1RXS J160929.1-210524 b	330	1.664	8.37	-	-	1800	L4	16.86	16.15	2.219 ± 0.002	NASA
SR 12 AB c	1100	-	13	-	-	2400	M9-L0	15.35	14.57	8.659 ± 0.048	Martinez & Kraus (2022); NASA
2MASS J01225093-2439505 b	52	1	24.5	-	-	1600	L5	15.65	14.53	1.450 ± 0.002	NASA
HII 1348 B	138	-	59	-	-	2570	M8	15.30	14.88	1.12 ± 0.03	Geißler et al. (2012); Yamamoto et al. (2013)
DH Tau B	330	0.27	11	-	-	2700	M8	14.96	14.19	2.351 ± 0.001	Lazzoni et al. (2020)

Table 3.2: Characteristics of planets suitable for CRIRES+ follow-up analysis. In order from left to right, the columns contain the semi-major axis in astronomical units (a_P), the planetary radius in Jupiter's radii (R_P), the planetary mass in Jupiter's masses (M_J), the eccentricity and the inclination of the orbit (ecc, i), the effective temperature in Kelvin (T), the planetary spectral type (SP.T), the H and K magnitudes, the angular distance at the present epoch, and the paper or catalogues from which the characteristics were retrieved. When eccentricity and inclination were not found they were assumed for simplicity 0 and 90°, respectively.

Main characteristics of their stars

Star	Sp. T	Age [Myr]	T_{eff} [K]	$R_\star$ [$R_\odot$]	$M_\star$ [$M_\odot$]	d [pc]	H	K	Gaia	Δm_H	Δm_K	Catalogue
μ_2 Sco	B2IV	20	21700	5.6	9.1	169	4.159	4.292	3.543	-	11.7	NASA
η Tel	A0V	-	11941	1.6	2.18	49.54	5.15	5.01	5.001	6.8	8.2	EU
GJ 504	G0V	160	6234	-	1.22	17.56	4.107	4.033	5.039	16.28	15.38	NASA
HR 8799	A5V	60	7400	1.49	1.47	39.4	5.28	5.24	5.91	b:12.57 c:11.63	b:11.79 c:10.87	NASA
HR 3549	A0V	130	10207	1.88	2.35	92.5	6.047	6.044	6.013	4.2	-	EU
HIP 64892	B9.5V	16	10400	1.79	2.35	125	6.879	6.832	6.798	7.23	6.8	EU
HD 19467	G3V	7200	5680	1.15	0.95	30.86	5.447	5.401	6.814	12.45	12.57	EU
HIP 65426	A2V	14	8840	1.77	1.96	111.4	6.853	6.771	6.999	11.14	10.01	NASA
HIP 78530	B9V	5	10000	2.1	2.5	156.7	6.946	6.90	7.162	7.44	7.27	NASA
HD 984	F7V	30-200	6315	-	1.2	45.71	6.17	6.073	7.207	6.43	6.13	EU
HD 106906	F5V	13	6500	2.12	1.5	92	6.68	6.68	7.699	8.7	8.78	NASA
AB Pic	K2V	30.4	5188	0.92	0.9	47.3	7.09	6.98	8.838	7.6	7.16	NASA
HD 284149	F8	25	6040	1.36	1.14	108.2	8.208	8.1	9.43	6.507	6.22	EU
CD-35 2722	M1V	100	3680	-	0.4	21.3	7.28	7.046	10.217	5.5	4.98	EU
YSES 2	K1V	13.9	4749	1.193	1.1	109.4	8.484	8.358	10.525	10.37	9.55	NASA
GSC 08047-00232	K2V	42	-	-	0.89	86.29	8.53	8.45	10.614	6.91	6.3	EU
TYC 8998-760-1	K3IV	16.7	4573	-	1	94.6	8.562	8.39	10.638	b:7.43 c:11.25	b:6.41 c:9.57	NASA
GQ Lup	K7eV	2	4360	1.7	1.05	140	7.702	7.096	11.243	-	6.0	NASA
CT Cha	K7	2	-	-	0.7	165	8.944	8.661	11.801	-	6.23	NASA
GSC 06214-00210	M1	5	4300	0.9	0.6	145	9.342	9.152	11.855	6.19	5.74	NASA
1RXS J160929.1-210524	K7V	5	4000	1.3	0.85	150	9.109	8.891	12.037	7.751	7.26	NASA
SR 12 AB	K4; M2.5	3	-	-	-	125	8.63	8.408	12.21	6.72	6.16	NASA
2MASS J01225093-2439505	M3.5V	120	3400	0.366	0.4	36	9.47	9.198	12.891	6.18	5.36	NASA
HII 1348	K5V	-	-	-	-	127	9.83	9.719	12.229	5.47	5.15	EU
DH Tau	M0.5	2	4371	1.36	0.33	140	8.824	8.17	12.456	6.14	6.01	NASA

Table 3.3: Characteristics of the host stars for objects of Table 3.2. In order from left to right, the columns contain the spectral type of the star, the age of the system, the effective temperature of the star (T_{eff}), the radius of the star in units of solar radii ($R_\star$), the mass of the star in units of solar masses ($M_\star$), the distance of the system in parsecs, the H, K and Gaia magnitudes of the host star, and the difference in magnitudes in the H and K bands between the host star and the planetary companion. Finally, in the last column is reported the catalogue from which these informations were retrieved.

Main characteristics of planets suitable for HiRISE follow-up

Planet	a_P [AU]	R_P [R_J]	M_P [M_J]	ecc	i [°]	T [K]	Sp.T	H	K	ang. dist.	Reference
β Pic b	7.9	1.65	11.73	0.106	89	1650	M	13.5	14.9	0.33	Lazzoni et al. (2020); NASA
51 Eri b	13.2	1	2	0.45	-	675	T4.5	19.2	17.11	0.449 ± 0.007	Brown-Sevilla et al. (2023); Lazzoni et al. (2020)
HR 7672 B	14	-	73	-	-	1800	L4-5	14.04	13.04	0.720	Wang et al. (2022) Ruffio et al. (2023)
HD 60584 B	15.58	0.908	28	-	-	-	-	-	-	0.543 ± 0.005	Bonavita et al. (2022)
HR 8799 d	24.82	1.2	10	<0.6	28	1090	L	16.84	16.09	0.630 ± 0.005	NASA, Zurlo et al. (2022)
HR 8799 e	16.4	1.17	10	0.15	25	1200	-	16.58	18.2	0.368	NASA Apai et al. (2016)
HR 2562 B	20.3	1.11	30	-	-	1200	L7	16.83	15.43	0.64	Lazzoni et al. (2020); NASA
AF Lep b	9.3	1.17	4.3	0.32	98	750	L-T	17.50	16.85	0.338 ± 0.064	De Rosa et al. (2023); NASA
HIP 21152 B	17.5	-	24	0.36	95.3	1250	T	17.04	16.55	0.422 ± 0.001	Bonavita et al. (2022); NASA
HD 206893 B	9.6	1.25	28	0.14	146.8	1500	L5-6	16.79	15.05	0.252 ± 0.005	Ward-Duong et al. (2021)
HD 1160 B	80	-	20	-	-	2800	M6	14.65	14.12	0.78	Sutlieff et al. (2023)
HD 95086 b	56.4	-	5	0.2	141	800-1300	L6	20.07	18.89	0.624 ± 0.007	Lazzoni et al. (2020); NASA
HIP 63734 b	30.02	-	11	-	-	-	-	17.78	-	0.555 ± 0.002	Bonavita et al. (2022)
HIP 75056 Ab	22.48	2	35	0.44	12	2300	M6-L2	14.5	14.07	0.125 ± 0.006	Wagner et al. (2020); Balmer et al. (2024)
PZ Tel B	27	2.42	27	0.52	91.73	2600	M7	12.39	11.89	0.558	Lazzoni et al. (2020); Schmidt et al. (2014)
HIP 29724 B	6.3	-	63	-	-	-	-	-	13.35	0.099 ± 0.001	Bonavita et al. (2022)
PDS 70 b	22	2.72	6.5	0.19	-	1200	L	17.94	16.5	0.177 ± 0.009	Lazzoni et al. (2020); Zhou et al. (2021)

Table 3.4: Characteristics of planets suitable for HiRISE follow-up. The columns contains the same parameters as in Table 3.2. Also here, when eccentricity and inclination were not found they were assumed for simplicity 0 and 90°, respectively.

Main characteristics of their stars

Star	Sp. T	Age [Myr]	T_{eff} [K]	R [$R_\star$]	M [$M_\star$]	d [pc]	H	K	Gaia	Δm_H	Δm_K	Catalogue
β Pic	A5V	12	8038.7	1.54	1.8	19.2	3.45	3.53	3.823	10	9.2	NASA
51 Eri	F0IV	16	7295	1.49	1.75	29.4	4.77	4.54	5.141	14.430	12.57	NASA
HR 7672	G0V	-	6000	-	-	17.72	4.430	4.388	5.645	9.6	8.65	EU
HD 60584	F5	1000	-	-	1.35	30.53	4.9	4.773	5.72	-	-	EU
HR 8799	A5V	60	7400	1.49	1.47	39.4	5.28	5.24	5.91	d:11.56 e:11.3	d:10.85 e:10.67	NASA
HR 2562	F5V	450	6597	1.33	1.3	33.63	5.128	5.02	6.004	11.7	10.4	NASA
AF Lep	F8V	24	6130	1.25	1.2	26.85	5.087	4.926	6.209	12.48	11.84	NASA
HIP 21152	F5V	650	6655	-	1.3	43.4	5.38	5.33	6.268	11.65	11.22	NASA
HD 1160	A0V	50	9100	-	2.2	103.5	7.01	7.04	7.11	7.64	7.01	EU
HD 95086	A8III	13.3	7595	1.48	1.7	90.4	6.867	6.789	7.324	13.1	12.1	NASA
HIP 63734	F7/8V	150	-	-	1.21	54.08	6.522	6.436	7.610	11.26	-	EU
HIP 75056	A2V	16	-	-	1.7	122	7.350	7.302	7.75	7.15	6.775	EU
PZ Tel	G9IV	47	-	-	1.36	51.49	6.486	6.366	8.102	5.9	5.52	NASA
HIP 29724	G2V	150	-	-	1.04	63.05	7.447	7.346	8.748	-	6	EU
PDS 70	K7	5.4	3972	1.26	0.76	113.4	8.82	8.542	11.606	9.12	7.81	NASA

Table 3.5: Characteristics of the host stars for planets of Table 3.4. The columns contain the same parameters as in Table 3.3.

Chapter 4

Spectroscopic analysis

The direct imaging technique, thanks to its capability to resolve the planet from its host star, makes it possible to adapt all the other methods for exoplanet detection to search for satellites, though with some additional limitations. In particular, the techniques are applied considering the exoplanet as the equivalent of the central star and the satellite as the detectable companion. For example, photometric variations in the flux of directly imaged exoplanets or brown dwarfs may be indicative of transiting satellites, as well as Doppler shifts in their spectra might point to the presence of further companions causing radial velocity trends. A major difference with respect to the usual star-planet situation is the presence of the host star at close separation and much brighter than the planet itself. A study by Lazzoni et al. (2022) reviews different methods used to search for satellites around a test exoplanet detected with direct imaging, β Pic b. The authors simulated a population of satellites around the exoplanet, then evaluated the detection limits of four different techniques (direct imaging, astrometry, radial velocity and transit) and compared them with the capabilities of current and future instrumentation. Similar works were done by Ruffio et al. (2023), Vanderburg et al. (2018) and Vanderburg & Rodriguez (2021). They adopted the radial velocity technique on different self-luminous targets to put constraints on the possible satellite companions' characteristics or to estimate the capabilities of current instrumentation in detecting them.
Taking inspiration from these works, I decided to focus on the radial velocity technique and apply it to each directly detected exoplanet or brown dwarf of my catalogue, illustrated in chapter 3. This project aims to estimate the detection limits for satellites around each object of the catalogue and compare them with the capabilities of CRIRES+ and HiRISE. After this, I will provide a selected group of promising targets that, with further observations, could represent the best candidates to search for satellite companions.
Section 4.1 illustrates the main characteristics of the radial velocity technique and how it changes when applied for satellites' detection. Section 4.2 presents the key aspect of this project, which is to understand the radial velocity precision needed to detect satellites around an exoplanet. This limit takes into account both the characteristics of the system and the characteristics of the instrument, such as the spectral type, the S/N and the wavelength coverage ($\Delta\lambda$). Section 4.3 evaluates the contamination that the primary star of the system induces in the radial velocity calculation on the exoplanet and that adds up to the previous evaluation of the detection limit as an additional error that needs to be taken into account. Finally, in Section 4.4 the synthetic populations of satellites generated around every suitable target are presented, with a discussion of the results obtained.

4.1 Radial velocity

The radial velocity of a target, a star or a planet, with respect to the observer is the rate of change of the vector displacement between two points. In astronomy, one of the points is usually the observer on Earth whereas the second point is the observed target, so the radial velocity denotes the speed at which the object moves away, or towards, the Earth (Perryman (2018)).
The presence of an exoplanet around a star causes a visible effect on the plane of the sky, which varies the stellar velocity, detectable with the astrometry technique and an effect along the line of sight, which causes the Doppler shift of the stellar spectral lines, detectable with the radial velocity technique (Bozza et al. (2016)). In fact, in all orbiting systems, both the star and the exoplanet orbit around each other in a closed elliptical orbit with a fixed centre of mass. In this configuration, when an exoplanet rotates around it, the star's angular position in the sky changes periodically and with astrometric measurements, it is possible to monitor its apparent location over time. Instead, the radial velocity perturbation aspect is the main object of this chapter.

Radial velocity, or Doppler shift, measurements represent the projected motion, along the line-of-sight, of the primary star orbiting the barycentre of the system. Since the star is often much heavier than the exoplanet, the centre of mass is within the star's surface and this effect is very small. Nonetheless, as of today, the radial velocity technique, second only to the transit technique, has produced a high number of detected exoplanets (1097 out of 5756)[1]. Also, we recall that this is the technique with which Mayor & Queloz (1995) discovered the first exoplanet around a Main Sequence star, 51 Peg b.
This technique employed for exoplanet detection is based on the research of the Keplerian motion as an indicator of the presence of an undetected secondary companion orbiting the star (Murray & Correia (2010); Lovis & Fischer (2010)). It involves the third Kepler's law which is:

$$P^2 = \frac{4\pi^2(a_\star + a_p)^3}{G(M_\star + M_p)}$$

where $a_\star, M_\star$ are the semi-major axis and the mass of the star, a_p, M_p are the semi-major axis and the mass of the planetary companion and P is the period of the planet. From solving the two-body problem and through this law, the radial velocity semi-amplitude of the star induced by the exoplanet orbiting around it is given by:

$$K_\star\,[m/s] = \left(\frac{2\pi G}{P}\right)^{1/3} \frac{M_p\, sin\, i}{(M_\star + M_p)^{2/3}} \frac{1}{(1-e^2)^{1/2}} \tag{4.1}$$

where P is the orbital period of the exoplanet, M_p and $M_\star$ are the exoplanet's and host star's masses, and e and i are the eccentricity and inclination of the orbit, respectively. As we can see this value depends on many orbital factors of which the orbital inclination, i, is particularly critical. In fact, from the radial velocity measurements, it is possible to retrieve only the minimum mass of the exoplanet, $M_p\, sin\, i$. Since this technique measures the radial component of the velocity, it is not capable of distinguishing between the detection of a low-mass object with an inclination close to ninety degrees or a high-mass object with a much smaller inclination. Another factor that strongly affects the radial velocity value and shape is the eccentricity. The typical shape of a radial velocity curve

[1] https://exoplanetarchive.ipac.caltech.edu/docs/counts_detail.html

is sinusoidal and it is given when considering almost zero eccentricity, while higher values of e result in a more complicated shape of the curve. This is an important factor to take into account because with poor sampling exoplanets in very eccentric orbits might escape detection and the primary star might be considered with constant radial velocity, hence without any planetary companion.
This technique can also be applied to exoplanets or brown dwarfs detected with direct imaging to search for exomoons or binary companions by simply shifting the subject of the formula from the star to the planetary companion. The radial velocity semi-amplitude of the exoplanet, induced by the satellite orbiting it, becomes:

$$K_p\,[m/s] = \left(\frac{2\pi G}{P}\right)^{1/3} \frac{M_s\, sin\, i}{(M_p + M_s)^{2/3}} \frac{1}{(1-e^2)^{1/2}} \tag{4.2}$$

where P is the orbital period of the satellite around the exoplanet, M_s and M_p are the satellite's and exoplanet's masses, while e and i are the eccentricity and inclination of the satellite's orbit, respectively. From equations 4.1 and 4.2, we see that the radial velocity semi-amplitude directly depends on the mass of the orbiting object and inversely depends on its orbital period. In particular equation 4.2 tells us that this method is more effective in identifying more massive and close-in satellite companions.

Configuration	K [m/s]
Jupiter around Sun	12.4
Earth around Sun	0.089
Moon around Earth	12.52
Ganymede around Jupiter	0.85
Charon around Pluto	23.22
0.1 M_E satellite around 20 M_J exoplanet (P=15 days)	0.34

Table 4.1: Illustration of the different values of the radial velocity semi-amplitude (K), calculated with equation 4.1 and 4.2 in different configurations. The first three configurations are calculated assuming the characteristics of Jupiter, Earth and Moon in our Solar System. The last three were computed assuming $e = 0$ and $i = 90°$.

As reported in Table 4.1, the typical radial velocity semi-amplitude of a Jupiter-like exoplanet orbiting a Sun-like star is 12.4 m/s, while for an Earth-like exoplanet orbiting a Sun-like star is 0.089 m/s, which is a very low value and difficult to reach with nowadays instrumentation considering the uncertainties in the stellar activity. I also reported three values of radial velocity semi-amplitudes for planet-moon systems. In particular, the Earth-Moon system is the most analyzed and well-studied planet-moon system, Ganymede is the largest moon in our Solar System and the Charon-Pluto system is considered a "double dwarf planet" system. Other examples of semi-amplitude values of moons of our Solar System are reported in Vanderburg et al. (2018) (Table 2). The last value was computed assuming a 0.1 M_E satellite around a 20 M_J exoplanet in a 15-days orbit with $e = 0$ and $i = 90°$. The radial velocity semi-amplitude in this case increases to 0.34 m/s which is in principle reachable with nowadays instrumentation. Moreover, both theory and numerical simulations predict that such satellites could be easily formed around massive exoplanets and brown dwarfs.

4.2 Radial velocity precision

The estimation and refinement of the radial velocity (RV) precision is one of the most difficult, but fundamental, tasks of this technique. After the first years from 51 Peg b discovery in 1995, the Doppler precision improved from around 10 m/s to 3 m/s, in 1998, and then to about 1 m/s in 2005 when the High-Accuracy Radial Velocity Planetary Searcher (HARPS) became operating (Mayor et al. (2003)). Nowadays, thanks to ESPRESSO at VLT it is possible to reach an RV precision down to 10 cm/s (Mégevand et al. (2014)). The precision depends both on the instrument characteristics and on the system properties. Moreover, the contamination of the spectra of the target, for example in the case of binary systems, or in the search of satellites from the exoplanet's host star, is also relevant in the estimation of the RV precision. To increase the precision on the spectrograph level, higher resolution, higher sampling (thus more performing CCD detectors), more stability and more precise wavelength calibration are needed. From this point of view, the echelle spectrograph CRIRES+ offers high-quality data which are promising for both the detection of exoplanets and satellites, because it observes in the IR wavelength, rather than in the optical. On the other side, the precision depends also on stellar activity, when searching for exoplanets, or planetary intrinsic variability (Vanderburg et al. (2018)), when looking for satellites. As it can be seen in Figure 4.1, early-type stars (spectral type earlier than F) present few spectral lines, because of their higher temperatures. Moreover, these few lines are often broadened, due to the high rotational rates. For these stellar types, the Doppler study of the lines to search for planetary companions is challenging and imprecise. Instead, later-type stars, for example G-type stars like our Sun, are more stable and present more spectral lines, thus it is easier to study the Doppler shifts caused by an exoplanet. For these reasons, these spectral types represent the ideal target in the radial velocity study.

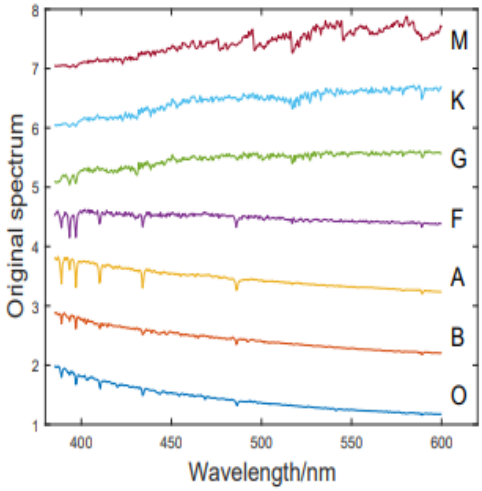

Figure 4.1: Seven examples of stellar spectra that highlight the different spectral lines based on the stellar type. Source: Li et al. (2019) (their Fig. 2). More details on spectral types are in Appendix C.

The effect of stellar activity that perturbs the spectral lines is referred to as jitter. The jitter is defined as a spurious Doppler signal caused by stellar activity that comes in different timescales, amplitudes and with different noise distributions. These signals can

mimic the presence of an exoplanet around the star and lead to fake planet detection (Huélamo et al. (2008)). For this reason, it is very important to identify and study them. In stars, the jitters can be caused by spots or stellar surface structure, stellar oscillations, convection patterns and noise. The amplitudes and frequency of these signals are enhanced for spotty, fast rotating and low-gravity stars. Nowadays there are several techniques developed to identify the jitter and confirm or reject the exoplanet candidate, such as the photometric study of the stellar surface (Saar et al. (1998)), the detection of CaII H and K lines and the study of the bisector of spectral lines (Queloz et al. (2001)).

The same challenges are found in the Doppler study of planetary spectral lines when looking for satellite companions. Vanderburg et al. (2018) evaluated the different radial velocity contributions that affect the total satellite signal but are due to the hosting exoplanet. They found that besides the satellite reflex motion, which is typically of the order of km/s, the second most important contribution to the satellite's signal is given by the planetary intrinsic variability, for example, the presence of clouds or atmospheric activity. These signals are of the order of 100 m/s and they are difficult to model due to our poor knowledge of the exoplanetary atmosphere and vary based on the system considered.

In this project, I evaluated the RV precision of the directly imaged exoplanet or BDs based on the work by Bouchy et al. (2001), in particular using equation 12. I estimated the detection limits for each target of a selected group, following the formula:

$$RV_{prec} = \frac{c}{Q\, S/N\, \sqrt{\Delta\lambda}} \tag{4.3}$$

where c is the speed of light, Q is a quality factor (see Section 4.2.1), S/N is the signal to noise ratio evaluated for every target as illustrated in Section 4.2.3 and $\Delta\lambda$ is a fixed interval of wavelength in units of nm (see Section 4.2.2). I decided to adapt Bouchy et al. (2001) equation to my project by approximating the square root of the total number of photoelectrons ($\sqrt{N_{e^-}}$) with the S/N values, and also by adding the wavelength coverage range term. The former is valid when the S/N is high because the photon noise is the dominant factor in the total error noise and the other factors are negligible (see equation 4.4). When the S/N is small this approximation is not valid anymore because other noise contributors become significant. However, in both scenarios, I decided to consider the S/N value because, in general, is a more reliable approximation than the total number of photons. By definition, the S/N is:

$$S/N = \frac{S}{\sqrt{\sigma_S^2 + \sigma_{SKY}^2 + RON^2 + \sigma_D^2}} \propto \frac{N_{e^-}}{\sqrt{N_{e^-}}} = \sqrt{N_{e^-}} \tag{4.4}$$

where S is the total signal intensity of the target and it is proportional to N_{e^-}, σ_S is the error associated with the signal which, assuming a Poissonian distribution of the collected photons, is equal to $\sqrt{S}$, σ_{SKY} is the associated background noise, RON is the Read-Out-Noise of the CCD, which correspond to a constant value based on the CCD and σ_D is the thermal noise associated to the total exposure time and the sensor temperature. In this work, I considered only the noises due to the signal of the planet and the contamination from the host star, while other sources of error, like wavelength calibration, instrumental stability and intrinsic variability of the planet were neglected because they are still not defined with enough precision for the chosen instruments. The wavelength range term was added to take into account an average value of all the spectral lines inside a grating order range (see CRIRES+ manual, Dorn et al. (2023) pag. 73, Table 13).

4.2.1 Quality factor, Q

Based on the work by Bouchy et al. (2001), I estimated a plausible range of quality factor values suitable for every target of my catalogue. In their work, the authors estimated the quality factor Q for F-G-K stellar spectral type, different stellar rotational rates (v sin$i$ from 0 to 20 km/s) and different spectral resolutions of the spectrograph. Their work aimed to compute the uncertainty of the RV measurements due to the stellar noise. In my project, I applied the radial velocity technique to the exoplanet rather than the star, so I estimated this uncertainty for the exoplanet noise. Following the work by Bouchy et al. (2001), I assumed a mean planetary rotational velocity of 16 km/s for each target of the sample and approximated a range of Q values between 4000 and 5000 for spectral types between M and L, which were not included in the paper considered but are part of this work. The rotational velocity is expected to be moderately large for our targets, considering a few sparse results from high-resolution spectra of directly imaged planets (Snellen et al. (2014); Ruffio et al. (2023)) and the rotation of Jupiter in the Solar System. Instead, the range of quality factors was extrapolated from Table 2 of Bouchy et al. (2001) in the column relative to the fixed rotational velocity of 16 km/s. For my project, I decided to estimate a range of values of quality factor rather than specific values for each spectral type to give an approximation of the range in which the radial velocity uncertainties could fall around each target. In future works, this range should be refined to better characterize the specific value of the radial velocity uncertainty.

Spectral type	Q	v sin$i$
M-type	4000-4600	16 km/s
L-type	4600-5000	16 km/s

Table 4.2: Range of quality factor values for spectral types M and L with fixed planetary rotational velocity to 16 km/s, estimated following Table 2 of Bouchy et al. (2001).

4.2.2 Wavelength coverage, $\Delta\lambda$

The wavelength coverage term was added to equation 4.3 to take into account an average of the planetary spectra rather than the specific value at a fixed spectral line.
I selected the 36 grating order range between 1566.354 and 1596.996 nm, so the $\Delta\lambda$ results in 300 nm. This corresponds to the minimum grating order providing full-slit spectral coverage in the chosen setting on ETC, $H1582$ filter (Dorn et al. (2023), their Table 13).

4.2.3 Signal to noise ratio, S/N

The S/N factor of equation 4.3 was computed differently depending on whether the object was assigned to CRIRES+ or HiRISE.
For the HiRISE sample of exoplanets the values were discussed in a private communication with the PI of the instrument, Arthur Vigan. HiRISE is a new-generation instrument still in development, thus the S/N values were available only for 9 out of 17 exoplanets that were assigned to HiRISE in my project. The other 8 targets, where the S/N was not available, were left aside for further studies when more data will become available. The S/N values available for the exoplanets assigned to HiRISE are reported in Table 4.3.

Planet	S/N
β Pic b	23
51 Eri b	5
HR 8799 d	18
HR 8799 e	21
HR 2562 B	22
AF Lep b	14
HD 1160 B	25
PDS 70 b	11
HD 95086 b	2

Table 4.3: List of HiRISE exoplanets and BDs directly detected with their S/N values. The values were discussed in a private communication with the PI of the instrument, Arthur Vigan. The last planet, separated from the others by a horizontal line, was left aside for future works due to its low S/N value.

Based on equation 4.3, to reduce the uncertainty in the RV, we need observations with high S/N. One of the targets had an S/N value of 2 which was too low to obtain significant results in this type of research, so I rejected it. We recall that the purpose of this project is to select a group of exoplanets or brown dwarfs detected with direct imaging with promising radial velocity precision for the detection of satellite companions, utilizing CRIRES+ and HiRISE.

For the CRIRES+ sample of exoplanets, the S/N values were computed with the Exposure Time Calculator (ETC)[2]. This tool either provides the S/N achieved in a fixed exposure time or estimates the exposure time necessary to reach a specific value of the S/N. It takes into consideration the target properties, the instrument setup, and the constraints set, such as sky conditions, airmass, and seeing. While the ETC is built to estimate S/N or exposure time for a stellar target, I employed it to estimate the S/N for planetary targets or brown dwarfs, which brought some challenges. In particular, I adopted the `PHOENIX` catalogue model for the exoplanets' Spectral Energy Distribution (SED), which has a minimum temperature of 2 300 K. For exoplanets and BDs with colder temperatures, I adopted the `Blackbody` model, even though this approach is less precise.
In my calculations, for simplicity, I assumed standard observable parameters, which are reported in Table 4.4. I also assumed the NGS AO mode and adopted the central star H band magnitude as the NGS magnitude.

Parameter	Value	Description
log(g)	3.5	Logarithmic value of the exoplanet's surface gravity
airmass	1.4	A measure of the amount of air along the LOS
FLI	0.5	Fractional Lunar Illumination
PWI	2.5	Precipitable Water Vapour in mm
Slit width	0.2"	Slit width of CRIRES+
Seeing	$\leq$ 0.8"	Degree of turbulence in the Earth's atmosphere
τ_0	$\geq$ 4.1 ms	Minimum Coherence time

Table 4.4: Illustration of the standard observable parameters adopted in the ETC to estimate the S/N of exoplanets and BDs assigned to CRIRES+.

[2] `https://etc.eso.org/crires2`

For targets where the `PHOENIX` model was applied, I chose an observing time of 600DIT × 2NDIT, for a total of 20 minutes of observation. Instead, for targets for which I used the `Blackbody` model, the resulting S/N was much smaller in the same exposure time. This is because colder objects have a lower emission peak in the IR and for example, to increase the S/N of a factor 3 we need to increase the total exposure time of at least a factor 9. I first extended the observing time to 900DIT × 8NDIT, for a total of 2 hours of observation. Then, for very faint targets, I further extended the interval to 900DIT × 20NDIT, for a total of 5 hours of observation.
Finally, as a reference wavelength value, I chose the $H1582$ filter (1582.339 nm) and, when the exoplanet wasn't observed in the H band, I utilized the K-band at 2216.704 nm (K2217).
Among the 27 exoplanets assigned to CRIRES+, for 13 of them I calculated the S/N adopting the `PHOENIX` model in the H and K bands, while for 14 of them I calculated the S/N adopting the `Blackbody` model in the same bands. The S/N results for these bands are reported in Tables 4.5 and 4.6 along with the main parameters utilized in the ETC.

Planet	T_{eff} [K]	H_p	$H_\star$	DIT [s]	NDIT	S/N	MODEL
η Tel B	2600	11.93	5.15	600	2	49.4	PHOENIX
HR 3549 B	2350	10.24	6.047	600	2	130	PHOENIX
HIP 64892 B	2600	14.11	6.879	600	2	9.31	PHOENIX
HIP 78530 B	2700	14.39	6.946	600	2	7.33	PHOENIX
HD 984 B	2730	12.60	6.17	600	2	30.2	PHOENIX
HD 284149 b	2537	14.71	8.208	600	2	5.5	PHOENIX
CD-35 2722 B	1800	12.78	7.27	600	2	24	PHOENIX
DH Tau B	2700	14.96	8.82	600	2	4.4	PHOENIX
SR 12 AB c	2400	15.35	8.63	600	2	3	PHOENIX
GSC 06214-00210 b	2200	15.52	9.34	600	2	2.69	PHOENIX
HII 1348 B	2570	15.3	4.292	600	2	3	PHOENIX
HD 106906 b	1820	16.2	6.78	900	8	3.23	Blackbody
AB Pic b	1513	14.69	7.09	900	8	12.2	Blackbody
GSC 08047-00232 b	2100	15.45	8.53	900	8	6.56	Blackbody
TYC 8998-760-1 b	1727	15.99	8.56	900	8	3.87	Blackbody
2M0122-2439 b	1600	15.65	9.47	900	8	5.19	Blackbody
GJ 504 b	510	20.14	4.107	900	20	0.055	Blackbody
HR 8799 b	870	17.85	5.28	900	20	0.7	Blackbody
HR 8799 c	1090	16.91	5.28	900	20	1.85	Blackbody
HD 19467 B	978	17.90	5.447	900	20	0.712	Blackbody
HIP 65426 b	1500	17.99	6.853	900	20	0.76	Blackbody
YSES 2b	1300	18.85	8.358	900	20	0.25	Blackbody
TYC 8998-760-1 c	1240	19.81	8.56	900	20	0.137	Blackbody
1RXS J1609-2105b	1800	16.86	9.109	900	20	2.23	Blackbody

Table 4.5: List of CRIRES+ exoplanets and BDs with their S/N ratio values in H band. The values of the S/N were computed with the ETC. In the Table are also reported the parameters utilized in the computation: the effective temperature of the planet (T_{eff}), the magnitudes in the H band of the exoplanet or BD and the star (H_p and $H_\star$), the detector integration time in seconds (DIT), and the number of DIT exposures (NDIT). In the computation I fixed airmass=1.4, slit width=0.2" and seeing<0.8".

Planet	T_{eff} [K]	K_P	$K_\star$	DIT [s]	NDIT	S/N	MODEL
GQ Lup B	2700	13.1	7.096	600	2	8.53	PHOENIX
CT Cha b	2600	14.89	8.661	600	2	2	PHOENIX
μ_2 Scorpii b	2200	15.99	4.292	900	8	1.6	Blackbody

Table 4.6: List of CRIRES+ exoplanets and BDs with their S/N ratio values in K band. The values of the S/N were computed in the same conditions and the columns contain the same parameters as in Table 4.5 except for the columns with K-band magnitudes of the exoplanet or BD and of the star.

I preferred the 20-minute observing time interval because this project aims to provide a sample of exoplanets and BDs for which we can have access to the satellite regime in a reasonable amount of telescope time. A 20-minutes integration time can be significantly extended, even to 2 hours or 5 hours, for single-epoch observations aimed at planet atmospheric characterization, but longer times become much less manageable when considering multi-epoch radial velocity monitoring. Hence, to obtain significant results for this project, I decided to apply equation 4.3 only to targets with S/N>4. For this, all the exoplanets with a total exposure time of 5 hours in Table 4.5 were left aside for a more specific analysis. I also rejected SR 12 AB c, GSC 06214-00210 b, HII 1348 B among the targets with a total exposure time of 20 minutes and HD 106906 b and TYC 8998-760-1 b among the targets with a total exposure time of 2 hours. In Table 4.6, instead, I kept only GQ Lup B. These rejected objects could be observed with ANDES at ELT (Marconi et al. (2024), Section 1.4.3) to obtain high precision results and higher S/N values. The targets of CRIRES+ that I kept for the estimation of the detection limits are reported in Table 4.7, while the targets of HiRISE that I kept are in Table 4.8.

4.2.4 Detection limits estimation

Following equation 4.3, I computed a range of radial velocity uncertainties for each of the 20 selected targets from Tables 4.3, 4.5 and 4.6. The results are reported in Table 4.7 for CRIRES+ and in Table 4.8 for HiRISE. Note that in Table 4.7 are also reported the results for the three objects with a total exposure time of 2 hours, highlighted by an asterisk. Moreover, I report GQ Lup B for CRIRES+ where the analysis was developed in K-band for lack of observations in the H-band.
These radial velocity uncertainty values consider both the properties of the exoplanet or brown dwarf and their associated instrument. However, when the radial velocity technique is applied to the exoplanet or brown dwarf, rather than to the star, to search for satellites, we are dealing with a triple system composed of the satellite, the planetary host and the central star. In this configuration, the contamination of the central star at the separation of the secondary object becomes important in the computation. In particular, this effect makes the radial velocity precision estimation worse of a factor that it is linked to the instrument's PSF. In the next section, I illustrated the processes to retrieve this additional error on the radial velocity both for CRIRES+ and HiRISE and its impact on the final detection limits estimation for the purposes of my project.

Planet	Q_{min}	Q_{max}	S/N	$\Delta\lambda$ [nm]	RV_{min} [m/s]	RV_{max} [m/s]
η Tel B	4000	5000	49.4	300	70	88
HR 3549 B	4000	5000	130	300	27	33
HIP 64892 B	4000	5000	9.31	300	372	465
HIP 78530 B	4000	5000	7.33	300	472	591
HD 984 B	4000	5000	30.2	300	114	143
HD 284149 b	4000	5000	5.5	300	629	787
CD-35 2722 B	4000	5000	24	300	144	180
DH Tau B	4000	5000	4.4	300	787	984
AB Pic b*	4000	5000	12.2	300	283	355
GSC 08047-00232 b*	4000	5000	6.56	300	528	661
GQ Lup B	4000	5000	8.53	300	406	507
2M0122-2439 b*	4000	5000	5.19	300	667	834

Table 4.7: Table representing the fixed values utilized in the calculation of the radial velocity precision limits for the exoplanets and BDs assigned to CRIRES+. From left to right the columns contain the lower and upper estimated values of the quality factor (see Section 4.2.1), the signal to noise computed as illustrated in Section 4.2.3, the chosen wavelength interval illustrated in Section 4.2.2. The last two columns contain the upper and lower limits of the radial velocity uncertainties computed for each planet from equation 4.3 with Q_{min} and Q_{max}, respectively. The asterisk is to highlight the CRIRES+ exoplanets for which, to obtain a significant value of the S/N, the total observing time was expanded. Note that GQ Lup B is the only object in this table for which the calculation of the S/N was done in the K band.

Planet	Q_{min}	Q_{max}	S/N	$\Delta\lambda$ [nm]	RV_{min} [m/s]	RV_{max} [m/s]
β Pic b	4000	5000	23	300	150	188
51 Eri b	4000	5000	5	300	692	866
HR 8799 d	4000	5000	18	300	192	241
HR 8799 e	4000	5000	21	300	165	205
HR 2562 B	4000	5000	22	300	157	197
AF Lep b	4000	5000	14	300	247	309
HD 1160 B	4000	5000	25	300	138	173
PDS 70 b	4000	5000	11	300	315	394

Table 4.8: Table representing the fixed values utilized in the calculation of the radial velocity precision limits for the exoplanets and BDs assigned to HiRISE. The columns contain the same parameters as Table 4.7.

4.3 Contamination

To evaluate the contamination of the central star in the planetary spectra, three parameters are relevant in the radial velocity precision calculation: the angular separation between the star and the secondary companion, their flux ratios and their mutual spectral type. Observations of objects less separated from the host star are more affected by the stellar noise preventing the detection of satellites. However, if the secondary object is very near the host star but their spectral types are very different, then it is possible to disentangle the two contributions without significant challenges. If this is the case, it will be easier to distinguish between spectral lines associated with stellar activity and the ones associated with planetary activity.

First, to evaluate the contamination of the central star on the planetary spectra in CRIRES+ and HiRISE, I extracted the PSF of each instrument from observations in standard conditions (seeing=0.6" and airmass=1.1). These distributions tell us the fraction of stellar flux present at a given distance from the central star. In Section 4.3.1 and 4.3.2 are presented the main steps employed for the PSF computations and their distributions are reported in Figures 4.5 and 4.8. From these figures, I retrieved the fraction of stellar flux, in units of magnitude (Δm_C), present at the planetary angular distance for each planet of Tables 4.7 and 4.8.

After this, based on the work by Cunha et al. (2013) (their Figure 7, pg. 11), I evaluated the impact of the contaminant magnitude on the radial velocity calculation taking into account the exoplanet and star's spectral types.
In particular, their work evaluated the impact of a stellar companion within the fibre during the radial velocity measurements. They considered both the contaminant star as part of a binary system, in which the primary star is the target star and the secondary is contaminating its spectra, or as a background/foreground star. For this project, the focus will be only on the first scenario that they analyzed. They assumed spectral types varying between F-G-K-M for both the target and the contaminant stars. In this project, the target is represented by the exoplanet or BD, whose spectral types are M-L-T. Hence, I adopted the results of Cunha et al. (2013) in the case of a target with spectral type M3 and approximated later spectral types to it. Moreover, the contaminant is represented by the host star light and when its spectral type was an earlier type than F-type, I approximated to the earliest type available, which was F2 (see Figure 4.2). For these reasons, my results represent a pessimistic estimate for those spectral types and a detailed study is required to obtain more accurate results for each spectral type.

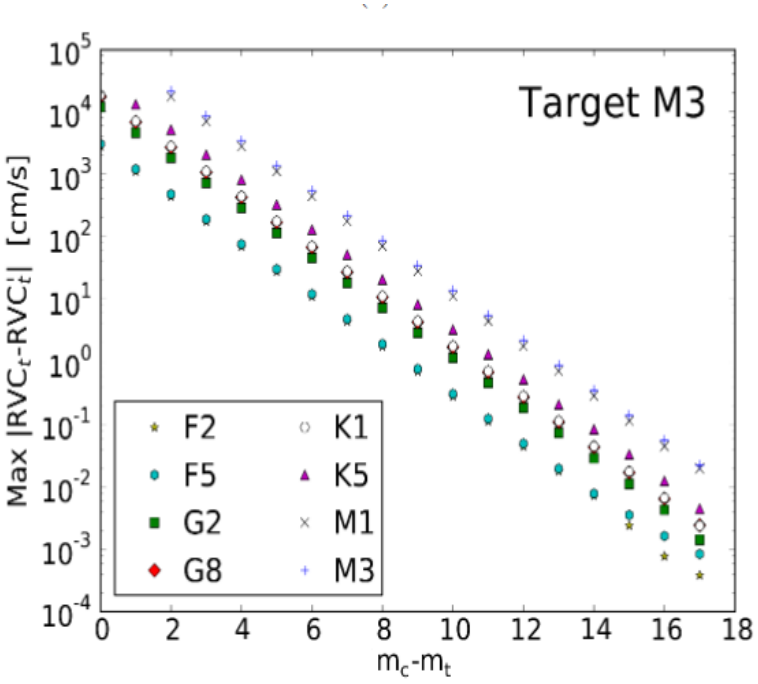

Figure 4.2: Maximum impact of magnitude difference (Δm) on the contamination of the radial velocity (RV_C) for a target star of spectral type M3 and contaminants of spectral types F2 (star), F5 (hexagon), G2 (squares), G8 (diamonds), K1 (circles), K5 (triangles), M1 (x crosses), and M3 (+ crosses). Source: Cunha et al. (2013) (their Fig. 7).

To retrieve the impact of the contaminant magnitude on the radial velocity measurements at the planet separation, I applied equation (1) from Cunha et al. (2013), reported here for simplicity:

$$RV_C\,[\mathrm{cm/s}] = 10^{a\cdot(\Delta m_C - \Delta m_H)+b} \tag{4.5}$$

where a and b are constants that depend on the mutual spectral type between the target and its star. I took the values from Table 7 (case of M3 target) of the same paper. I reported in Tables 4.9 and 4.10 the values for a and b for each target. $\Delta m_C - \Delta m_H$ is the difference between the fraction of stellar flux contaminating the planetary target in units of magnitude and contrast, in units of magnitude, of the planet with respect to the star in the H band. If this difference has a negative value then the stellar flux at the target's position is higher than the target flux itself. We note that for GQ Lup B, instead of the Δm_H, I considered the Δm_K, for lack of observations in the H band. The computed values of RV_C are reported in Table 4.9, for HiRISE, and in Table 4.10, for CRIRES+.

4.3.1 HiRISE

Since HiRISE couples the high-contrast imager SPHERE with the high-resolution spectrograph CRIRES+, to retrieve the PSF distribution I considered the observations of a target with IRDIS/SPHERE in H_2 and H_3 bands. In particular, I analyzed the observations of HIP 65426 (RA=13h24m36,10s DEC=-51d30m16.04s) of 6^{th} February 2017 taken in standard conditions, thus seeing=0.6" and airmass=1.1.

I started the analysis from the pre-reduced full-frame coronagraph data cube of the star HIP 65426. This data cube is made up of multiple images taken fixing the star at the centre and rotating the FoV around it (pupil-stabilized mode). To reduce the speckle noise left over from the AO system, I analyzed the image resulting from the median of all the images in the data cube. The coronagraph is useful because it reduces significantly the stellar contamination. However, the observations taken into account were making use of the satellite spots, reproductions of the stellar PSF behind the coronagraph along the diagonals. This practice is particularly useful for predicting the exact centre of each frame but, on the other hand, affects our analysis of the contamination. For this reason, I masked these spots with a circular mask with a radius of 7 pixels, centred on the brightest pixel of each spot. Then, I drew an annulus aperture, centred on the spots and 14 pixels wide, and I calculated the median value of the pixels therein, excluding the masked ones. Lastly, I substituted the values of the masked pixels with the calculated median. The initial and final images of this process are reported in Figure 4.3.

I analyzed only an 80×80 pixels frame of the total full-frame image. The restricted image was centred on the star and I generated a bundle of lines passing through the central pixel of the full-frame image. The bundle of lines was generated by varying the inclination angle from 0° to 83° and then from 96° to 180°. Angles between 84° and 95° were too close to the right angle and the angular coefficient values would degenerate. Along these lines, I evaluated the value of the flux at each pixel and took the median of all the pixel values at the same radial distance from the centre. In Figure 4.4 are represented some of the projected lines and some of the radial distances considered.

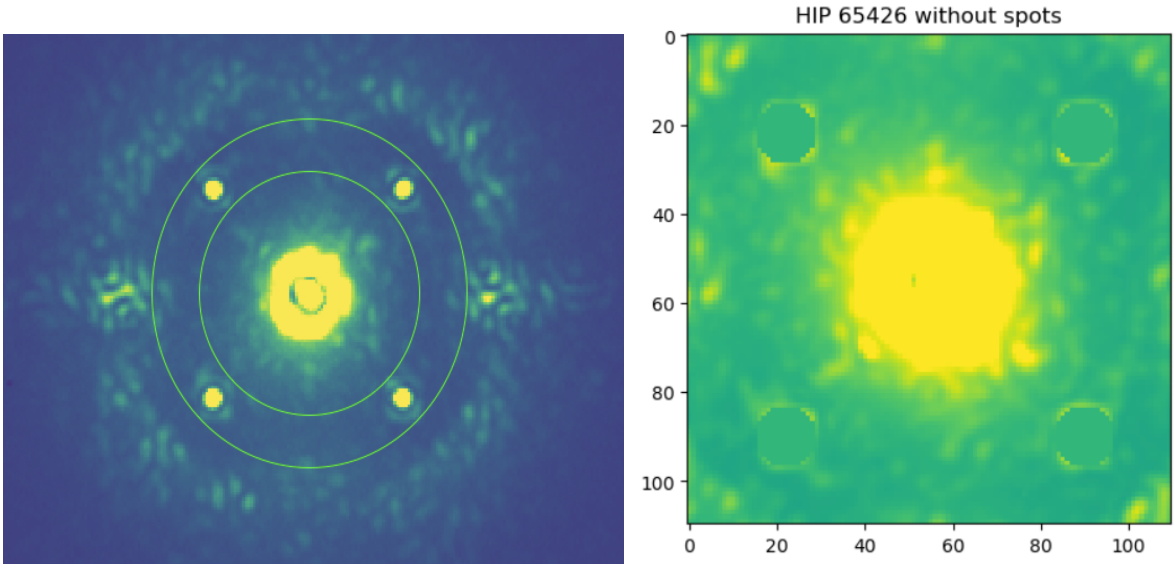

Figure 4.3: Illustration of the observations of HIP 65426 before (on the left) and after (on the right) the removal of the spots due to the coronagraph. In the left figure, is illustrated the image with the four spots (yellow spots) and the annulus region considered for the median computation (yellow circles). In the right figure, is illustrated the image with the spots masked by the four circular masks computed.

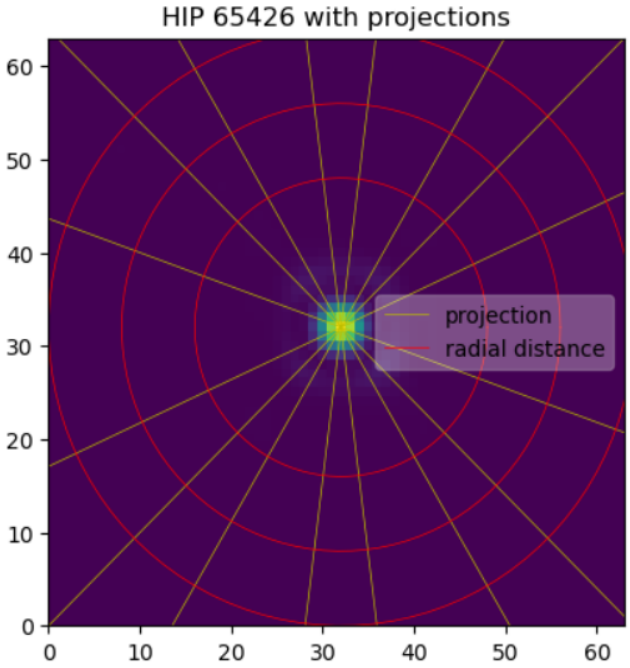

Figure 4.4: Illustration of the median image of HIP 65426 after removing the spots. The yellow lines represent some of the projected lines adopted for the analysis. The red circles represent some of the radial distances adopted to retrieve the final PSF of SPHERE. In particular, they correspond to a radial distance of 0.2, 0.3 and 0.4 arcseconds, respectively.

By doing so I obtained a single value of the flux for each radial distance in units of pixels. To translate this distance into an angular distance, I converted pixels into arcsecs knowing that for IRDIS the conversion factor is 0.01225”/pixel. Then, I normalized the

flux for the maximum flux at the centre of the image and translated this ratio into a magnitude difference with the formula reported in Appendix A. In this case, $m_A - m_B$ is the contamination magnitude, F_A is the stellar flux at a specific angular separation and F_B is the stellar flux at the centre of the image.

Figure 4.5 illustrates the final plot of the SPHERE PSF. This plot represents the magnitude difference of the contaminant with respect to the angular separation. Figure 4.5 presents two significant bumps at separations 0.1" and 0.8". The former is due to the reflected light caused by the end of the coronagraph, while the latter is due to the outer working angle of SPHERE beyond which the AO system is not effective anymore.

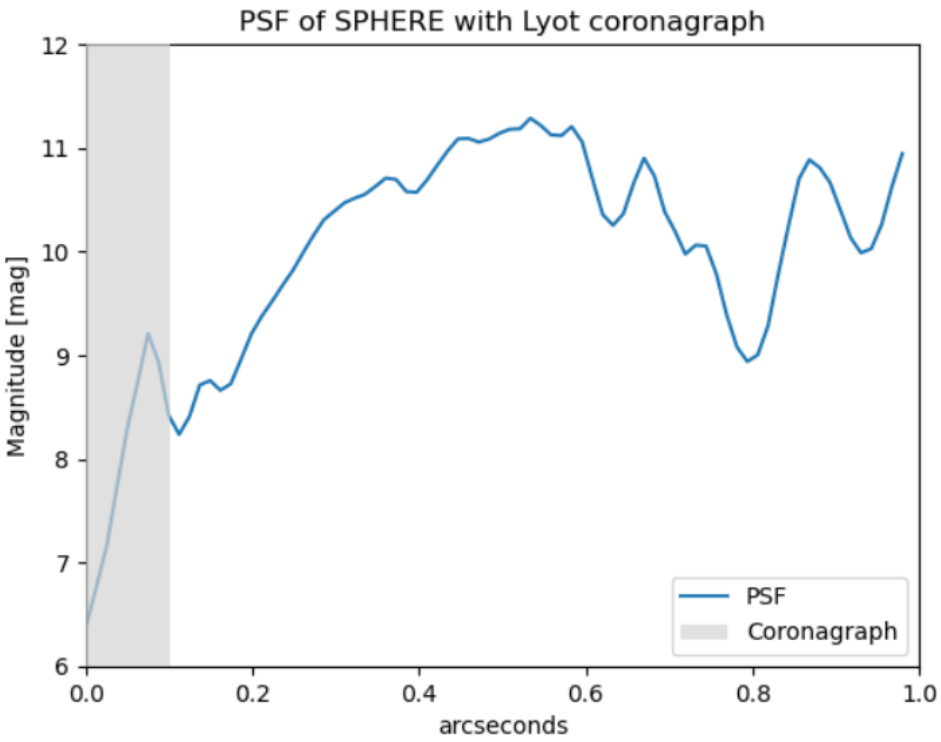

Figure 4.5: Illustration of the PSF of SPHERE retrieved from the observations of HIP 65426 (RA=13h24m36,10s DEC=-51d30m16.04s) on 6^{th} February 2017 taken in standard conditions, thus seeing=0.6" and airmass=1.1. The shaded grey area represents the area covered by the coronagraph. On the y-axis, there is the magnitude difference of the contaminant and on the x-axis, there is the angular separation in arcsecs.

The final radial velocity precision values for the targets assigned to HiRISE are reported in the last two columns of Table 4.9. These values were calculated by adding in quadrature (see Appendix B) the value of the radial velocity error resulting from the contamination (RV_C) and the values of the last two columns of Table 4.8.

Planet	Δm_H	Δm_C	Δ	a	b	RV$_C$ [m/s]	RV$_{min}$ [m/s]	RV$_{max}$ [m/s]
β Pic b	10	10	0	-0.4052	3.4770	30	154	191
51 Eri b	14.43	11	-3.5	-0.4052	3.4770	785	1047	1169
HR 8799 d	11.56	10.5	-1	-0.4052	3.4770	76	207	252
HR 8799 e	11.3	10.5	-1	-0.4052	3.4770	76	182	220
HR 2562 B	11.7	10.5	-1.2	-0.3924	3.4425	82	178	213
AF Lep b	12.5	10.5	-1.9	-0.3924	3.4425	154	291	346
HD 1160 B	7.6	9.5	1.86	-0.4052	3.4770	5	139	173
PDS 70 b	9.12	9	0	-0.4021	4.5317	340	463	520

Table 4.9: In this Table are reported the main parameters adopted for the computation of the final radial velocity precision for exoplanets and BDs assigned to HiRISE. From the left, the columns contain the difference in magnitudes between the planet and the host star (Δm_H) in the H band, the contaminant's magnitude extrapolated from Figure 4.5 (Δm_C) at the position of each planet, the difference between the first two columns, the values of a and b adopted in equation 4.5, the resulting radial velocity error from the contamination (RV$_C$) in m/s and, in the last two columns, the updated values of the minimum and maximum radial velocity precisions calculated as reported in appendix B.

4.3.2 CRIRES+

To retrieve the PSF of CRIRES+, I first considered the observations of the brown dwarf CD-35 2722 B/TYC 7084-794-1 B (RA=06h09m19,21s, DEC=-35d49m31,06s) in H-band taken in standard conditions (seeing=0.6" and airmass=1.1) retrieved from Alice Zurlo & Kevin Hoy (private communication). In particular, I analysed the 30^{th} January 2024 observations for each nodding position (A and B) reported in Figure 4.6.

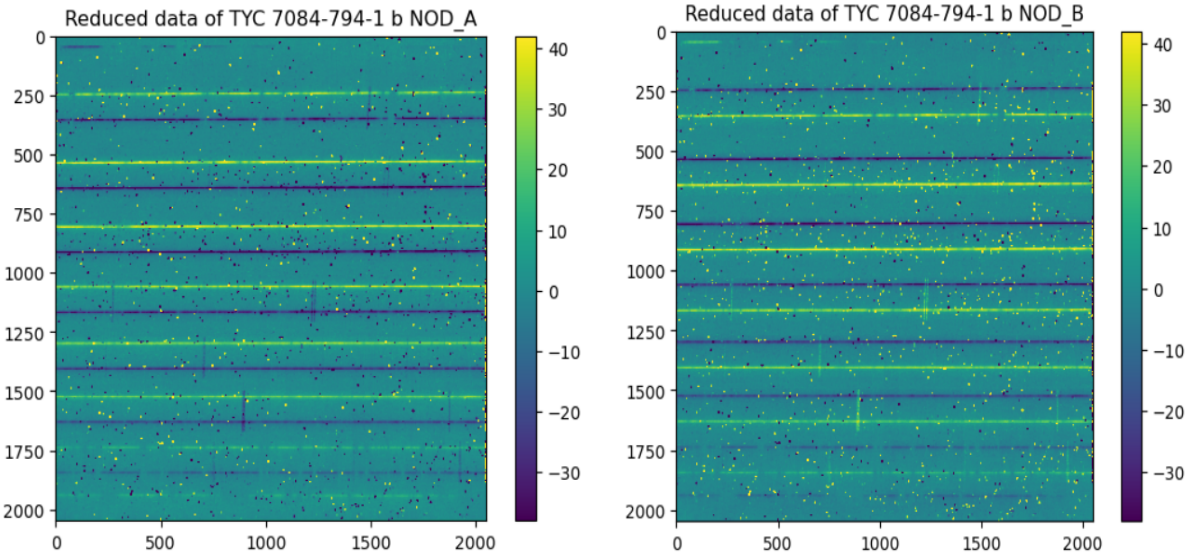

Figure 4.6: Illustration of the observations of the brown dwarf TYC 7084-794-1 B for the nodding position A (left) and B (right). The images are divided into 8 boxes where on the x-axis there are the wavelengths while each box represents a different order. In the analysis, I considered the first 6 starting from the top because they were the brightest. The horizontal yellow lines represent the slit of the spectrograph at each order, while the dark lines represent the negative counterpart of the slit position in the other nod.

On the x-axis of the initial image, there were the wavelengths, while on the y-axis the different orders. To reduce as much as possible the background noise of the data, I first divided the image into 8 boxes and considered only the first brightest 6, where each box was centred in the slit (yellow horizontal line in Figure 4.6) selecting only a single order, then I did the same division for the image of the second nodding observation. The 12 boxes were mediated to obtain a single image with a higher S/N reported in Figure 4.7. Then, to retrieve the final PSF, I projected a vertical line with respect to the slit direction into the median image for each pixel. Then, I mediated the values for each pixel in the horizontal direction at the same radial distance from the slit to obtain a single vertical projection. An example of the vertical lines projected in the median image is reported in Figure 4.7.

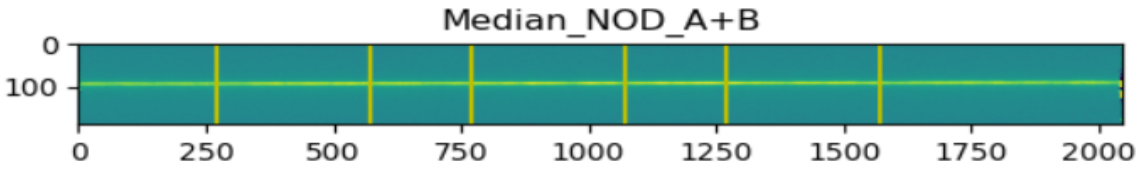

Figure 4.7: Illustration of the median image resulting from the median of the 12 selected boxes from nodding A and B observations. The yellow lines represent some of the projected vertical lines adopted for the PSF computation.

Finally, I plotted the distribution of the values of each pixel along this line as a function of the pixel itself for all the pixels along the x-axis. Then, I converted pixels into arcsecs knowing that for CRIRES+ the conversion factor is 0.059”/pixel. After this, I normalized the flux for the maximum value along the projected line and translated it into a magnitude difference with the same formula utilized for HiRISE (equation in Appendix A). The PSF distribution after this analysis is reported in Figure 4.8.
However, this PSF was retrieved from the observation of a BD companion which is fainter than a star and the background noise cannot be corrected efficiently. In fact, in this distribution, the fraction of flux present at larger distances should decrease much more and much faster. For this reason, I decided to proceed with the analysis considering the PSF distribution reported in the CRIRES+ User Manual (version P114.2)[3]. This plot was first left aside because it represented the distribution only for angular separations smaller than 1” and most of the objects assigned to CRIRES+ were at larger separations. Moreover, from this plot, it is difficult to extrapolate the value of the relative flux with the precision needed at separations larger than 0.25”. For lack of alternative data, I choose to approximate the analysis considering the PSF distribution, reported in Figure 4.9 taken in the H band at standard conditions (TC=30% and airmass=1.14) for a star with magnitude R=9.509.

[3] https://www.eso.org/sci/facilities/paranal/instruments/crires/doc/CRIRES_User_Manual_P114.2.pdf

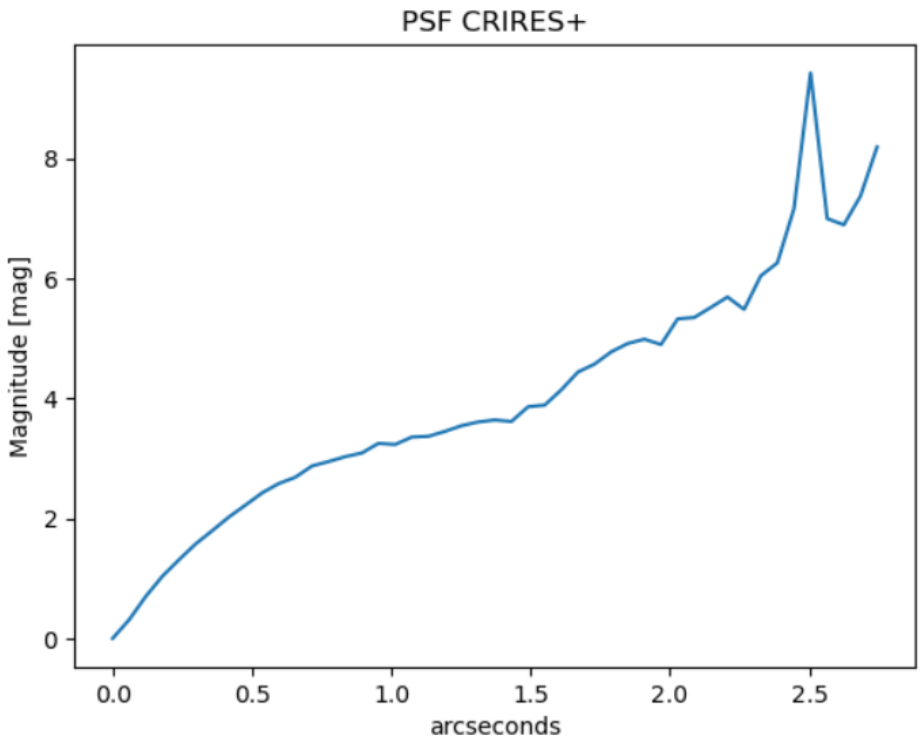

Figure 4.8: Illustration of the PSF of CRIRES+ from the observations of the brown dwarf CD-35 2722 B/TYC 7084-794-1 B (RA=06h09m19,21s, DEC=-35d49m31,06s) on 30^{th} January 2024 taken in standard conditions, thus seeing=0.6" and airmass=1.1.

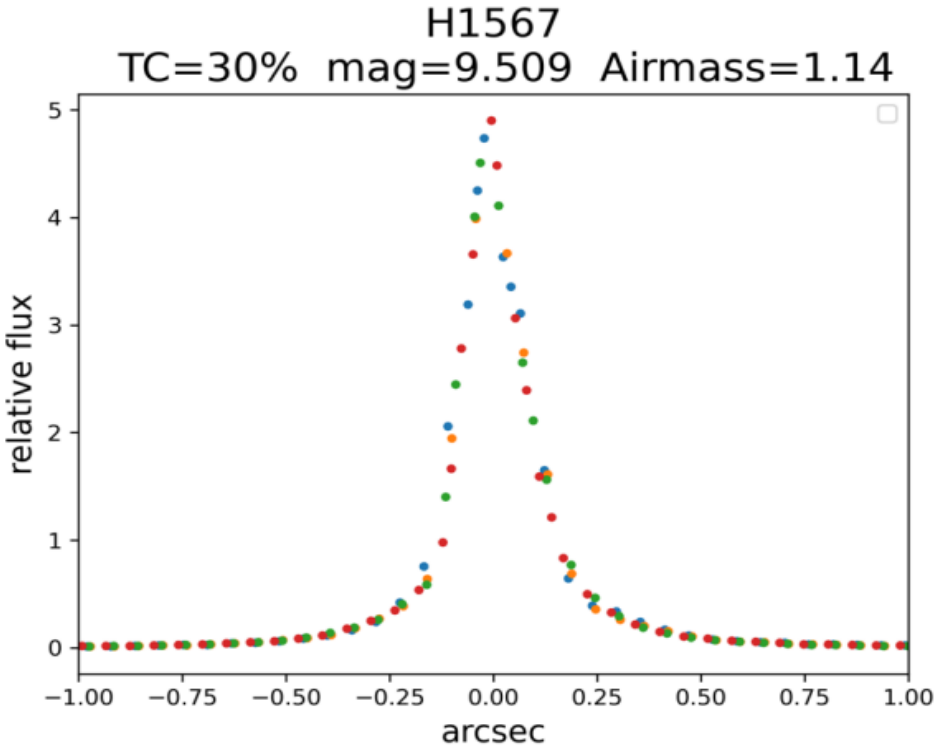

Figure 4.9: Illustration of the PSF of CRIRES+ from the CRIRES+ User Manual (version P114.2) taken in standard conditions (TC=30% and airmass=1.1) in the H band. Different colours represent different wavelengths.

In particular, I approximated all targets at separation larger than 1" with the PSF value at that separation obtaining a Δm_C=5 for all of them. In my sample only 3 out of 12 targets have an angular separation ≤1", while all the other targets results are an approximation. In future works, it will be possible to obtain a better description of the PSF also at larger separations and retrieve more precise results. Table 4.10 represents the result of this part of the analysis for objects assigned to CRIRES+. The final radial velocity precision values are reported in the last two columns of this table. These were calculated by adding in quadrature the value of the radial velocity error resulting from the contamination (RV_C) and the values of the last two columns of Table 4.7. The formula adopted for the addition in quadrature is reported in Appendix B.

Planet	Δm_H	Δm_C	Δ	a	b	RV$_C$ [m/s]	RV$_{min}$[m/s]	RV$_{max}$ [m/s]
η Tel B	6.8	5	-1.8	-0.4052	3.4770	161	176	183
HR 3549 B	4.2	4.48	0.3	-0.4052	3.4770	23	35	40
HIP 64892 B	7.23	5	-2.2	-0.4052	3.4770	234	440	521
HIP 78530 B	7.44	5	-2.4	-0.4052	3.4770	281	550	654
HD 984 B	6.43	2.32	-4	-0.3924	3.4421	1027	1033	1037
HD 284149 b	6.507	5	-1.5	-0.3924	3.4421	107	639	795
CD-35 2722 B	5.5	5	-0.5	-0.3991	5.0440	1752	1758	1761
DH Tau B	6.14	5	-1.1	-0.3991	5.0440	3040	3140	3195
AB Pic b	7.60	5	-2.6	-0.4024	4.2649	2047	2067	2078
GSC 08047-00232 b	6.91	5	-2	-0.4024	4.2649	1174	1287	1347
GQ Lup B*	6.004	4.25	-1.75	-0.4021	4.5317	1719	1766	1792
2M0122-2439 b	6.18	5	-1.2	-0.3999	5.1436	4202	4255	4284

Table 4.10: In this Table are reported the main parameters adopted for the computation of the final radial velocity precision for exoplanets and BDs assigned to CRIRES+. The columns contain the same parameters as Table 4.9

4.4 Results and conclusions

In the last part of the analysis, I generated a population of satellites around each target from Tables 4.9 and 4.10 along with their minimum and maximum detection limits. In particular, for each target, I computed the Roche radius and half of the Hill radius, which represent the lower and upper limits for the stability of a satellite around an exoplanet (the adopted formulas for the radii and the physical aspect of stability are illustrated in Section 2.3). The values adopted for each target to retrieve these quantities are reported in Table 4.11 for simplicity, but were taken from Tables 3.2, 3.3, 3.4 and 3.5 of chapter 3. After this, I generated a population of satellites with semi-major axes between the Roche radius and half of the Hill radius and with masses between one-thousandth of the target mass (M$_p$/1000) and the target mass itself. The final plots are illustrated in Figures 4.10 and 4.11, where the shaded grey area corresponds to the tidal disruption region, and the grey, light-blue, green, yellow and red curves represent satellites with orbital periods respectively of 10 days, 100 days, 1 year, 10 years and 100 years. In these plots, all the satellites with masses and semi-major axes above the inclined purple lines, that delimit the detection limits range, are expected to be detectable.

Planet	a_p [AU]	M_p [M_J]	ecc	$M_\star$ [$M_\odot$]
η Tel B	199.4	47	0.34	2.18
HR 3549 B	80	45	0.7	2.35
HIP 64892 B	159	33	0	2.35
HIP 78530 B	710	23	0	2.5
HD 984 B	9	61	0.76	1.2
HD 284149 b	400	32	0	1.14
CD-35 2722 B	67	31	0.82	0.4
DH Tau B	330	11	0	0.33
AB Pic b*	260	13	0	0.9
GSC 08047-00232 b*	277	13.8	0	0.89
GQ Lup B	117	20	0.24	1.05
2M0122-2439 b*	52	24.5	0	0.4
β Pic b	7.9	11.73	0.106	1.8
51 Eri b	13.2	2	0.45	1.75
HR 8799 d	24.82	10	0.6	1.47
HR 8799 e	16.4	10	0.15	1.47
HR 2562 B	20.3	30	0	1.3
AF Lep b	9.3	4.3	0.32	1.2
HD 206893 c	3.53	12.7	0.41	1.31
HD 1160 B	80	20	0	2.2
PDS 70 b	22	6.5	0.19	0.76

Table 4.11: The values adopted for each target of the sample to retrieve their Roche and Hill limits for the generation of a population of satellites around them. From the left, the columns contain the semi-major axis of the exoplanet (a_p), its mass (M_p), the eccentricity of the orbit (ecc) and the mass of the hosting star ($M_\star$). The values were taken from Tables 3.2 and 3.3 for the CRIRES+ targets and from Tables 3.4 and 3.5 for the HiRISE targets.

In the HiRISE sample of targets, we see that more or less the values of the radial velocity precision reachable are of the order of 10^2 m/s except for 51 Eri b, which has a precision of the order of 10^3 m/s. In fact, 51 Eri b is the target with the largest radial velocity error both in Table 4.8 and in Table 4.9, because of its faintness and large contamination. The high value in the former is due to its small S/N value, while the high value in the latter is due to the similarity between its spectral type, T-type but assumed M3-type in the analysis, and the spectral type of the host star, F0-type. For the same reasons, PDS 70 b is the target with the second largest error value for its radial velocity precision. PDS 70 b is the second planet with the smallest S/N value and its spectral type, L but assumed M3 in the analysis, is close to the spectral type of its host, K7. Moreover, the radial velocity study of PDS 70 b, as well as DH Tau B and GQ Lup B, is limited by their high intrinsic variability due to ongoing material accreting. For those three objects, this intrinsic variability could generate spurious signals in the radial velocity measurements, with errors in the order of km/s, which affects the accuracy of the radial velocity of the planet. Instead, for other targets, Vanderburg et al. (2018) estimated that the impact of planetary activity on radial velocity is around 100 m/s, which is small enough to be ignored for most of the targets listed in Tables 4.9 and 4.10. However, since the effect of planetary activity on radial velocity depends on many factors such as the target's spectral type, rotational velocity, and whether it is still accreting or not, further researches are

required to better define this error contribution, especially for targets like HR 3549 B, where the radial velocity precision is similar.
In conclusion, for this part of the sample, the most reliable results are those for β Pic b and HD 1160 B because their spectral type, M-type, did not require any approximation during the analysis. The other targets' results represent a pessimistic case and should be refined with further studies.
Looking at the plot for β Pic b in Figure 4.10, we conclude that all satellites with minimum mass above 0.5 M_J are detectable, while for lower masses, only particular separations are favoured. For example, a 0.1 M_J satellite on an orbit of less or equal to 10-days (grey curve) is detectable around this planet. Assuming sin i=1 and e=0, for equation 4.2, this type of satellite around β Pic b will generate an RV of 187m/s. For HD 1160 B all the satellites with minimum mass above 2 M_J are detectable, while for lower masses, only particular separations are favoured, for example, a 0.3 M_J satellite on an orbit of less or equal to 100-days (light-blue curve) is detectable. Assuming sin i=1 and e=0, for equation 4.2, this type of satellite around HD 1160 B will generate an RV of 184m/s. These results are promising because, considering that β Pic b and HD 1160 B are, respectively, an 11.73 M_J exoplanet and a 20 M_J brown dwarf, the assumption of a 0.1 M_J or a 0.3 M_J satellite orbiting them is reasonable, according to the formation theories of binary planets.

In the CRIRES+ sample of targets, we see that more or less the values of the radial velocity precision reachable are of the order of 10^3 m/s except for η Tel B, HR 3549 B and HIP 64892 B, which have a precision of the order of 10^2 m/s. While for HiRISE the order of magnitudes of the radial velocity between Tables 4.8 and 4.9 was the same, for CRIRES+ the values of the detection limits in Table 4.10 for each target besides η Tel B, HR 3549 B, HIP 64892 B and HIP 78530 B, have increased of a factor one with respect to Table 4.7. In fact, in the contamination part of the analysis, the last five targets of the sample generated the highest detection limits and in particular, 2MASS J01225093-2439505 b (RV_C=4202m/s) and DH Tau B (RV_C=3040m/s) had the highest values among them. This is because their spectral types, L5 and L2 (assumed spectral-type in the analysis M3), with respect to the spectral types of their host stars, M3.5 and M1, respectively, are very close and the contamination from the star is more difficult to disentangle. Moreover, their angular distances, 1.449" and 2.351" respectively, were out of range in the available PSF distribution for CRIRES+ (Figure 4.9). This brought a further approximation, worsening the results of the detection limit range. Only 4 out of 12 targets for CRIRES+ did not require any approximation, neither on their value of semi-major axes (<1") nor the spectral type (HR 3549 B, HIP 64892 B, HD 984 B and GQ Lup B). Hence, these are the only reliable results within the CRIRES+ sample. The other targets' results, as in the HiRISE part of the analysis, represent a pessimistic case and should be refined with further studies. We note that in the case of GQ Lup B, although no approximation was needed for this system, it has very high detection limits (RV_{min}=1766m/s and RV_{max}=1792m/s). This is due to the fact that its spectral type, M9, and its host spectral type, K7, are very close. Considering also that its retrieval was done adopting the magnitudes in the K-band for lack of observations in the H-band, results for this system are not very promising and might be less precise, so also this target requires further studies.
Looking at the plots for HR 3549 B, HIP 64892 B and HD 984 B in Figure 4.11 we conclude that for HR 3549 B all the satellites with minimum mass above 0.4 M_J are detectable, while for lower masses, only particular separations are favoured, for example, a 0.2 M_J satellite on a 1-year orbit (green curve) or shorter ones are detectable around this planet.

For HIP 64892 B all the satellites with minimum mass above 10 M_J are detectable, while for lower masses, only particular separations are favoured, for example, a 1 M_J satellite on an orbit of less or equal to 10-days (grey curve) or shorter ones are detectable. This is a particularly high mass for a satellite but considering that HIP 64892 B has a mass of 33 M_J, this would classify as a binary system that, as we discussed in chapter 2, cannot be excluded in principle. Finally, for HD 984 B all the satellites with minimum mass above 5 M_J are detectable, while for lower masses, only particular separations are favoured, for example, a 2 M_J satellite on an orbit of less or equal to 10-days (grey curve) is detectable. Assuming sin i=1 and e=0, for equation 4.2, this type of satellite around HR 3549 B, HIP 64892 B and HD 984 B, respectively, will generate an RV of 46m/s, 927m/s and 1178m/s. In conclusion, among the CRIRES+ sample, these 3 targets are the most promising for the search of satellites, however, with a more extended description of the instrument PSF, also η Tel B, HIP 78530 B and HD 284149 b might give promising results. Hence, hoping to improve this aspect of my project, I also included them in the final selection of the most favourable targets, which are reported in Table 4.12.

Finally, for this project, I select a total of 5 targets which present the most favourable conditions for further specific observations to search for exomoons or binary planets. They are reported in the last Table 4.12. Here are also reported the three CRIRES+ targets that might present favourable conditions after extending the angular separation scale of the CRIRES+ PSF (η Tel B, HIP 78530 B and HD 284149 b).
We note that among all of them, HR 3549 B is the most promising target having the lowest detection limits (RV_{min}=35m/s and RV_{max}=40m/s) and it will be the main subject of future researches and observations.
These results show the feasibility of a dedicated search for satellites around directly imaged exoplanets and brown dwarfs using the radial velocity technique. The number of available targets is limited by the current number of discovered exoplanets with direct imaging and the instrument characteristics, although it can be increased with a more extended investigation, for example including the targets rejected from the HiRISE sample because the S/N was unknown, or considering treatments of the CRIRES+ PSF shape at larger separations, to decrease the contamination error in the radial velocity precision. Furthermore, future instrumentation at ELTs will allow us to greatly extend the exoplanetary targets suitable for a radial velocity study to search for satellites and improve the precision as discussed in the conclusions.

Planet	M_p [M_J]	RV_{min} [m/s]	RV_{min} [m/s]	Instrument
β Pic b	11.73	154	191	HiRISE
HD 1160 B	20	139	173	HiRISE
HR 3549 B	45	35	40	CRIRES+
HIP 64892 B	33	440	521	CRIRES+
HD 984 B	61	1033	1037	CRIRES+
η Tel B	47	176	183	CRIRES+
HIP 78530 B	23	550	654	CRIRES+
HD 284149 b	32	639	795	CRIRES+

Table 4.12: Representation of the main characteristics of the final selected exoplanets and brown dwarfs for CRIRES+ and HiRISE that presented favourable conditions for the detection of satellites. The last three targets were included hoping to extend the PSF distribution of CRIRES+ in future works.

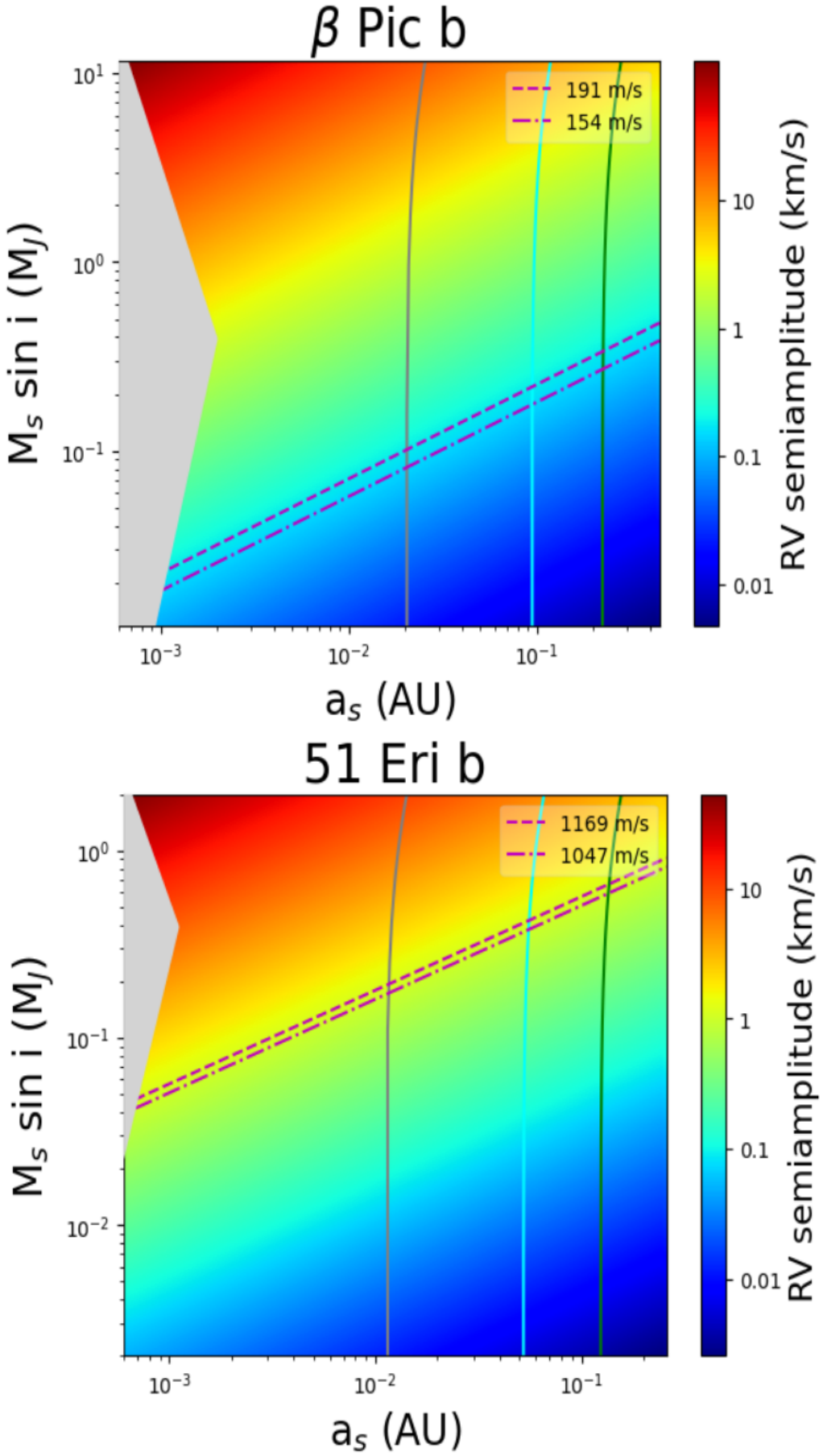
β Pic b
191 m/s
154 m/s
$M_s \sin i\ (M_J)$
a_s (AU)
RV semiamplitude (km/s)
51 Eri b
1169 m/s
1047 m/s
$M_s \sin i\ (M_J)$
a_s (AU)
RV semiamplitude (km/s)

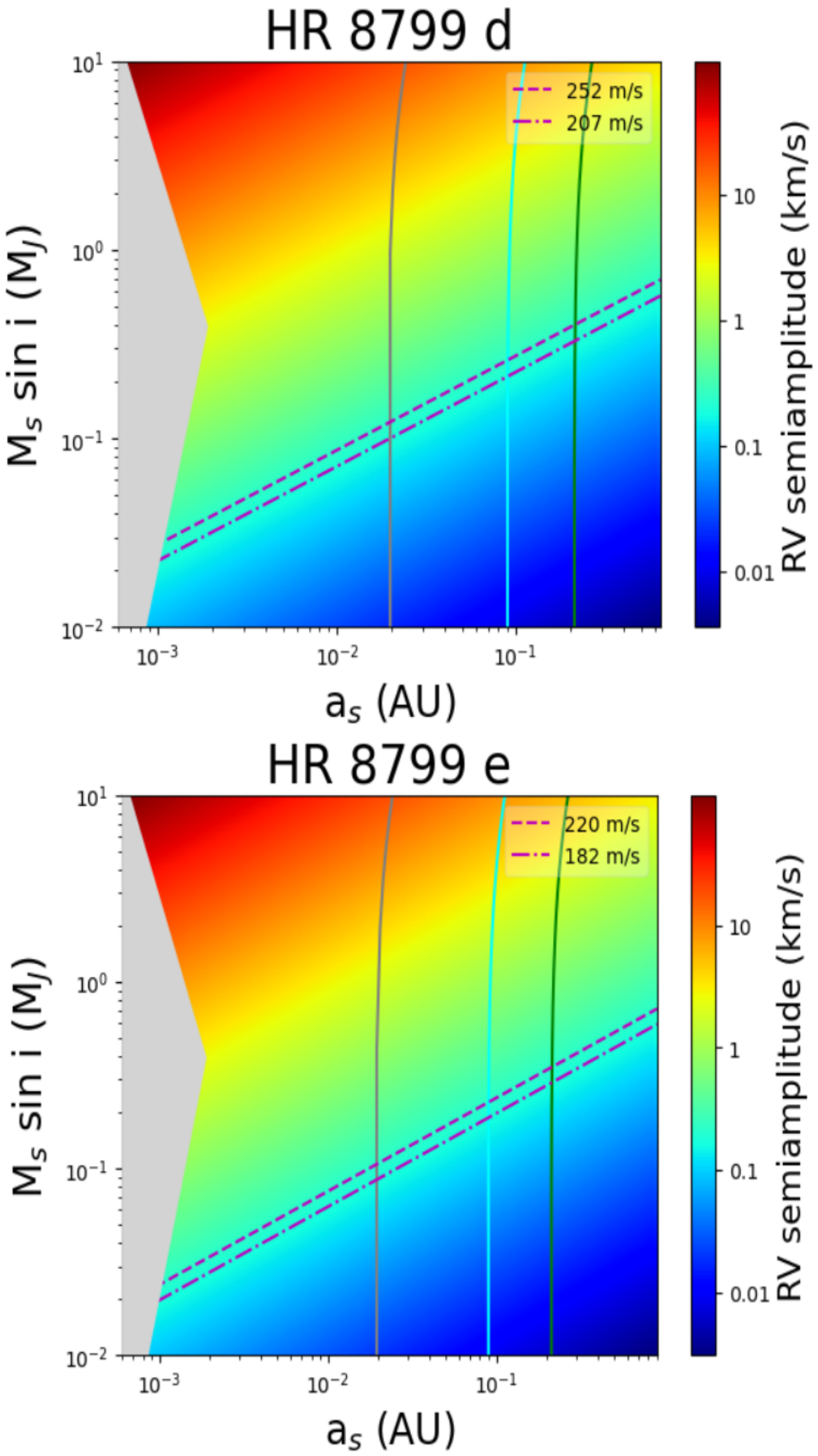
HR 8799 d
252 m/s
207 m/s
$M_s \sin i\ (M_J)$
a_s (AU)
RV semiamplitude (km/s)
HR 8799 e
220 m/s
182 m/s
$M_s \sin i\ (M_J)$
a_s (AU)
RV semiamplitude (km/s)

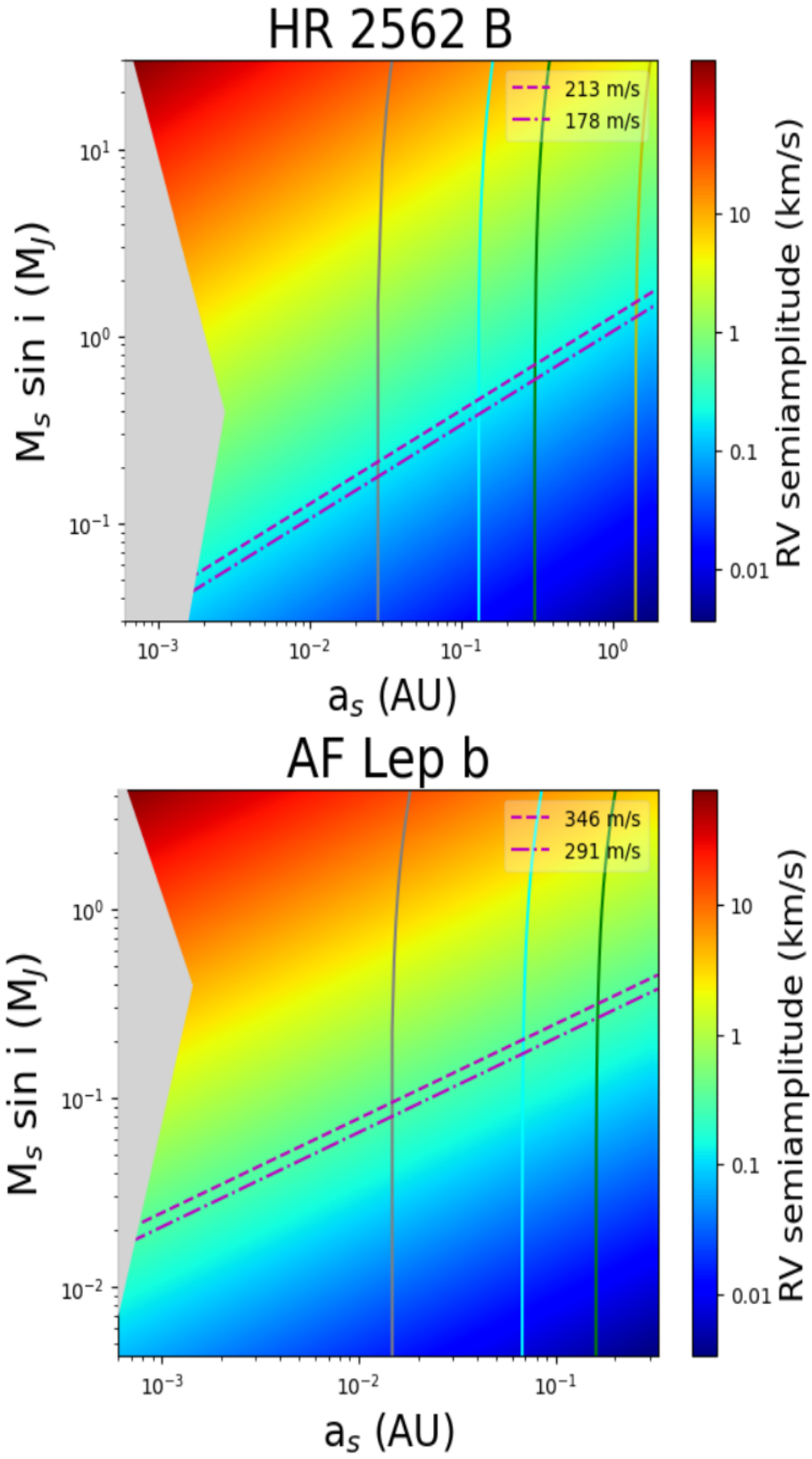
HR 2562 B
213 m/s
178 m/s
M_s sin i (M_J)
a_s (AU)
RV semiamplitude (km/s)
AF Lep b
346 m/s
291 m/s
M_s sin i (M_J)
a_s (AU)
RV semiamplitude (km/s)

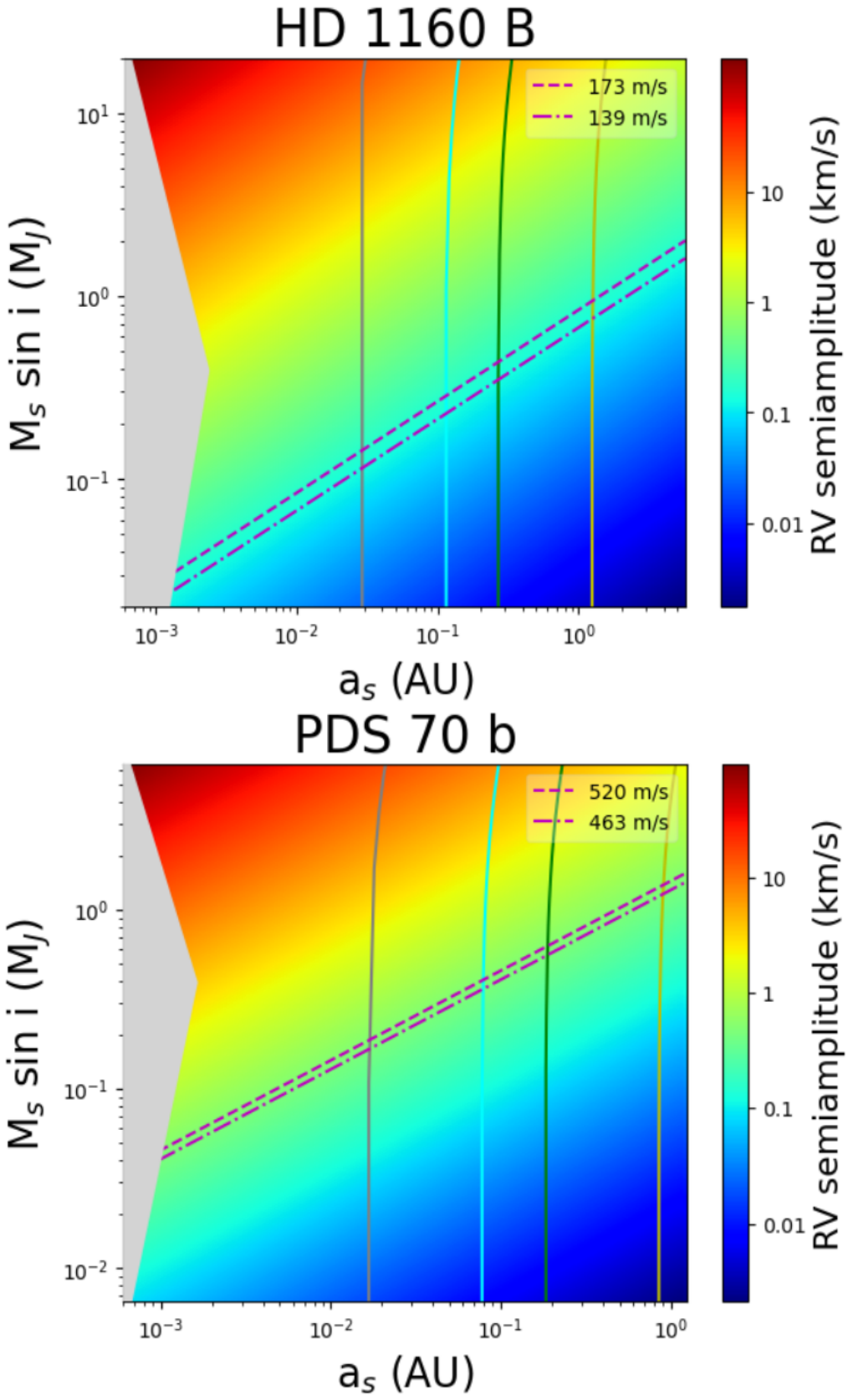

Figure 4.10: Results for HiRISE after generating a population of satellites around each target of the sample. The grey shaded area represents the area of the tidal disruption of the satellite, the purple lines represent the detection limits, RV_{min} and RV_{max}. The grey, light-blue, green, yellow and red curves represent respectively the orbits of satellites with periods of 10 days, 100 days, 1 year, 10 years and 100 years.

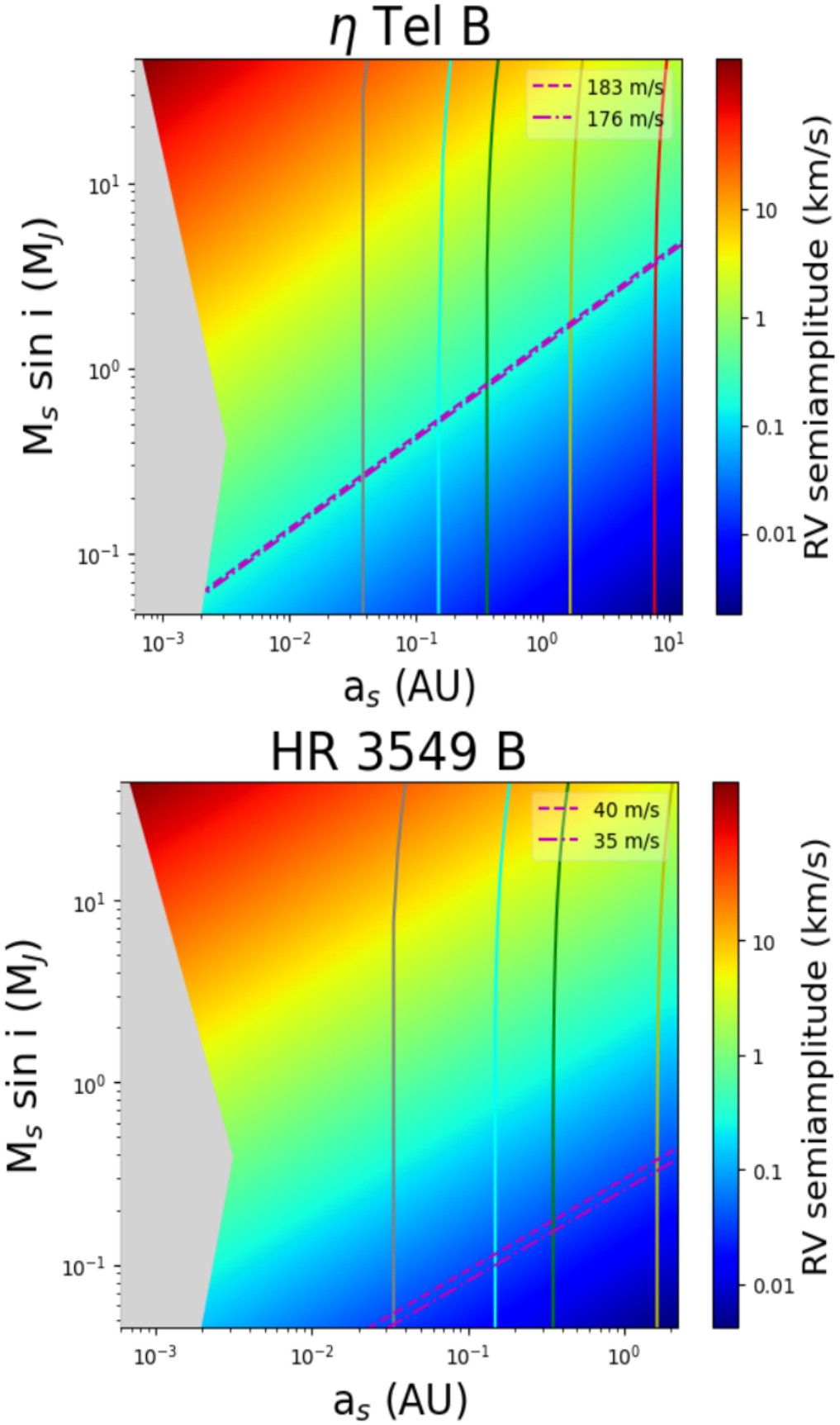
η Tel B
183 m/s
176 m/s
M_s sin i (M_J)
a_s (AU)
RV semiamplitude (km/s)
HR 3549 B
40 m/s
35 m/s
M_s sin i (M_J)
a_s (AU)
RV semiamplitude (km/s)

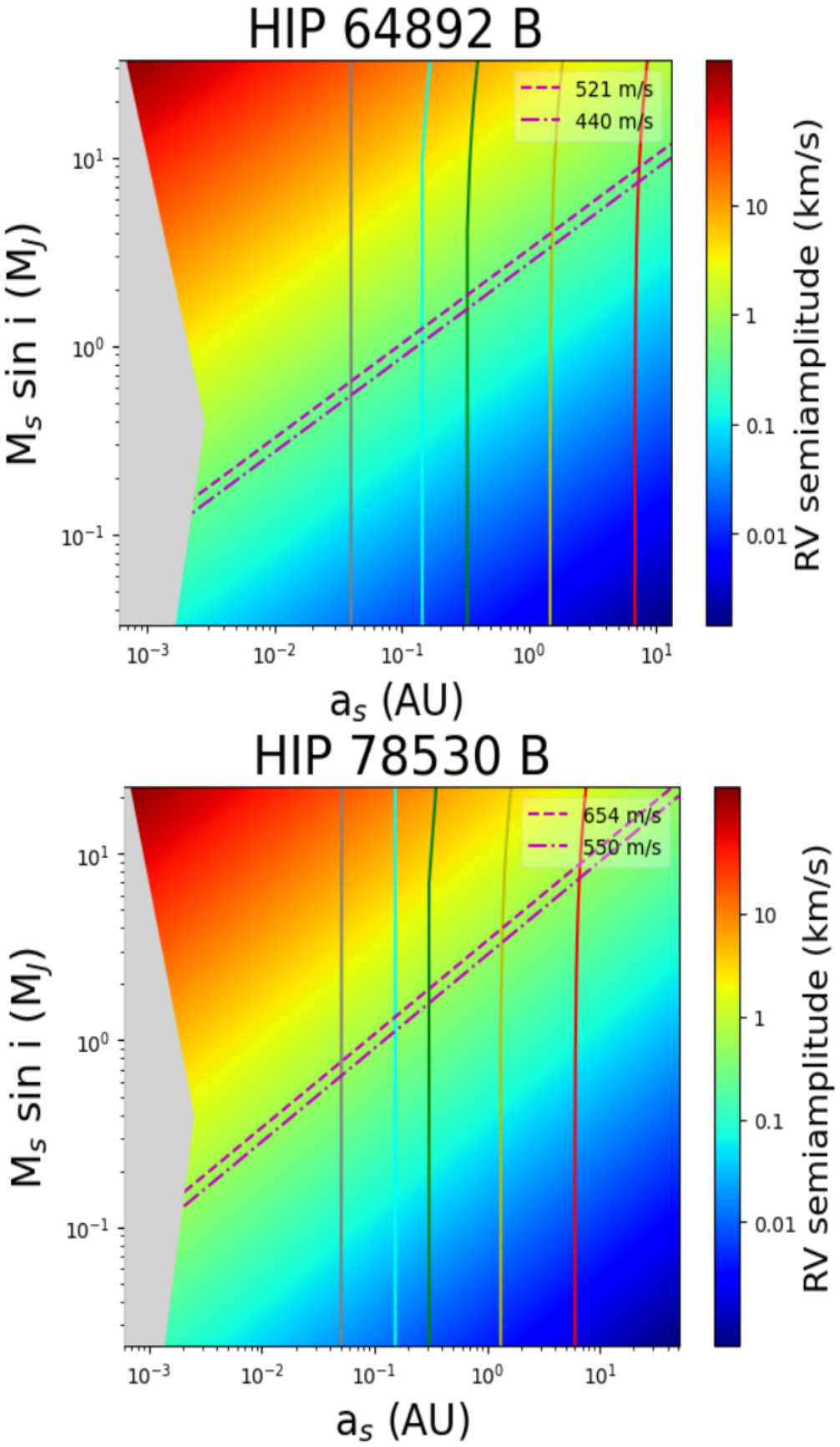
HIP 64892 B
521 m/s
440 m/s
M_s sin i (M_J)
a_s (AU)
RV semiamplitude (km/s)
HIP 78530 B
654 m/s
550 m/s
M_s sin i (M_J)
a_s (AU)
RV semiamplitude (km/s)

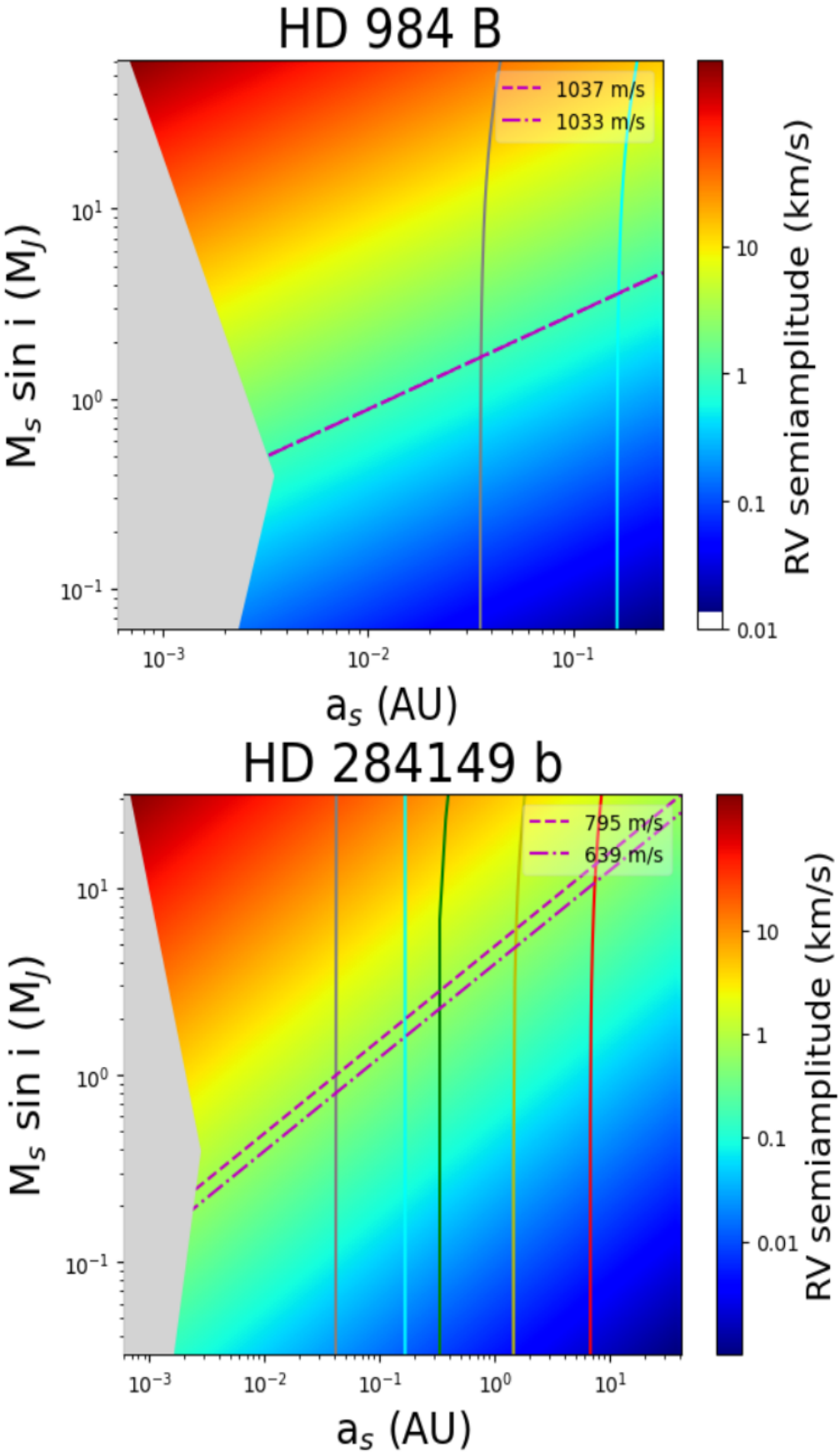
HD 984 B
1037 m/s
1033 m/s
M_s sin i (M_J)
a_s (AU)
RV semiamplitude (km/s)
HD 284149 b
795 m/s
639 m/s
M_s sin i (M_J)
a_s (AU)
RV semiamplitude (km/s)

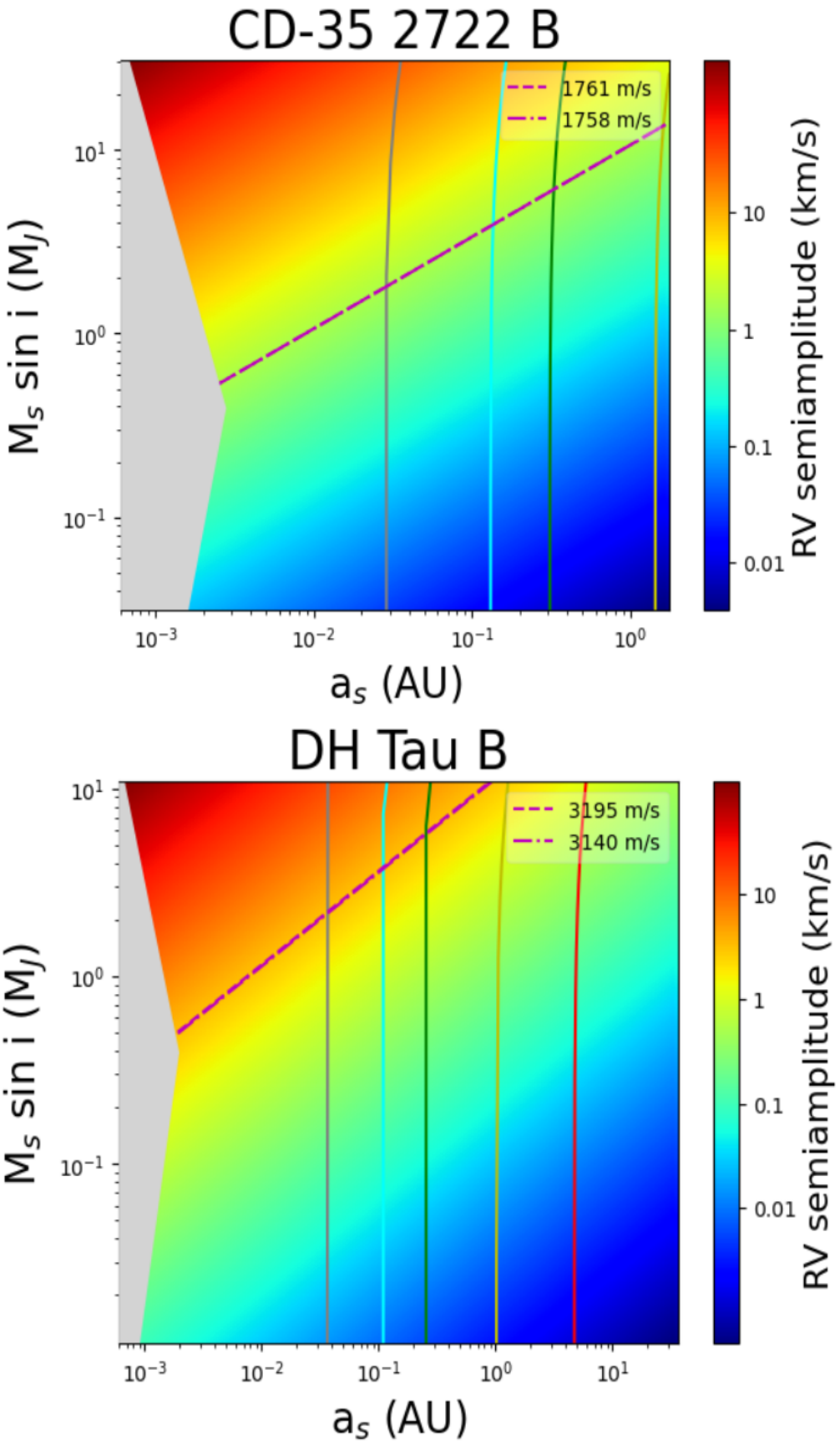
CD-35 2722 B
1761 m/s
1758 m/s
$M_s \sin i$ (M_J)
a_s (AU)
RV semiamplitude (km/s)
DH Tau B
3195 m/s
3140 m/s
$M_s \sin i$ (M_J)
a_s (AU)
RV semiamplitude (km/s)

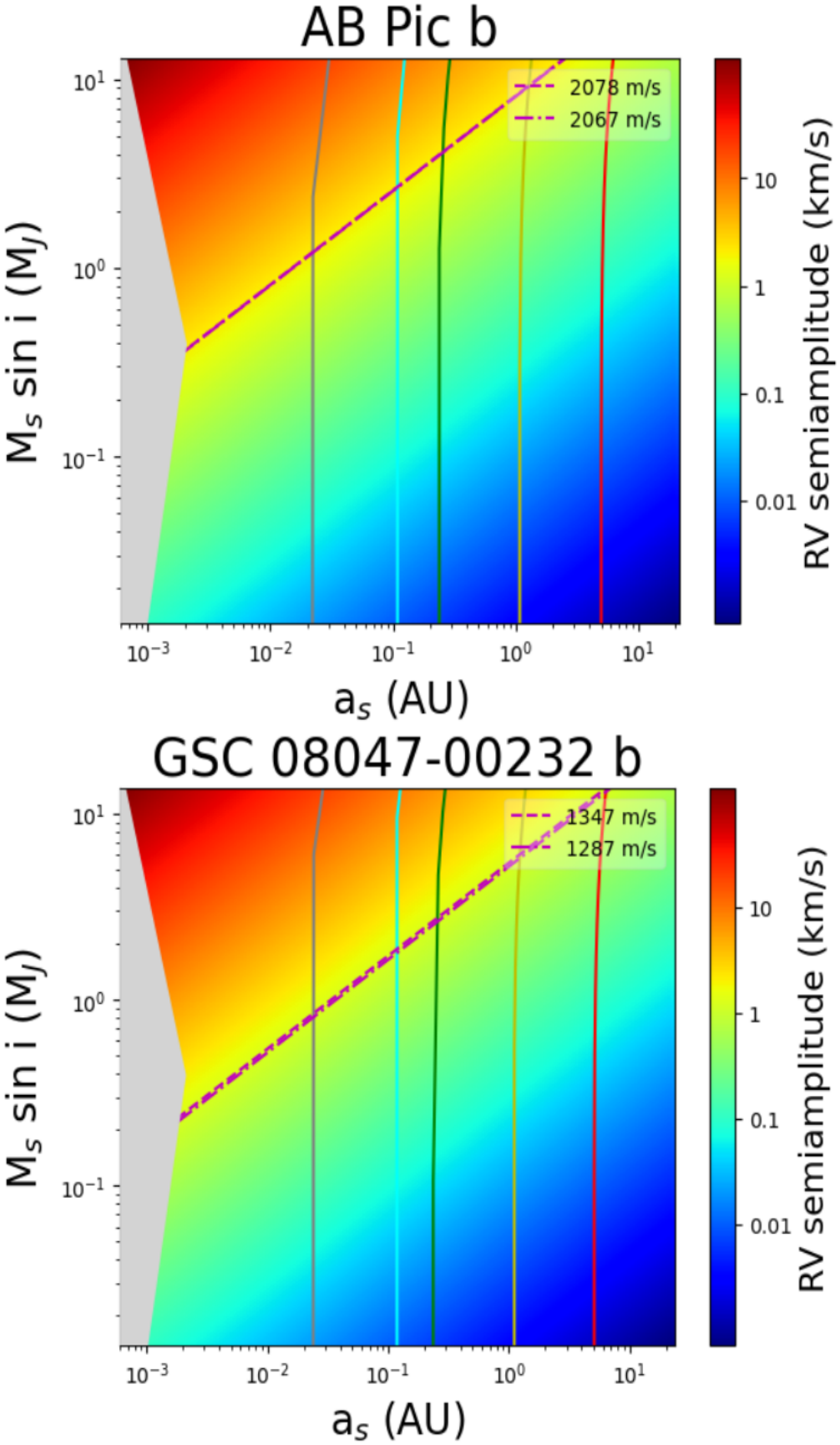
AB Pic b
2078 m/s
2067 m/s
$M_s \sin i\ (M_J)$
a_s (AU)
RV semiamplitude (km/s)
GSC 08047-00232 b
1347 m/s
1287 m/s
$M_s \sin i\ (M_J)$
a_s (AU)
RV semiamplitude (km/s)

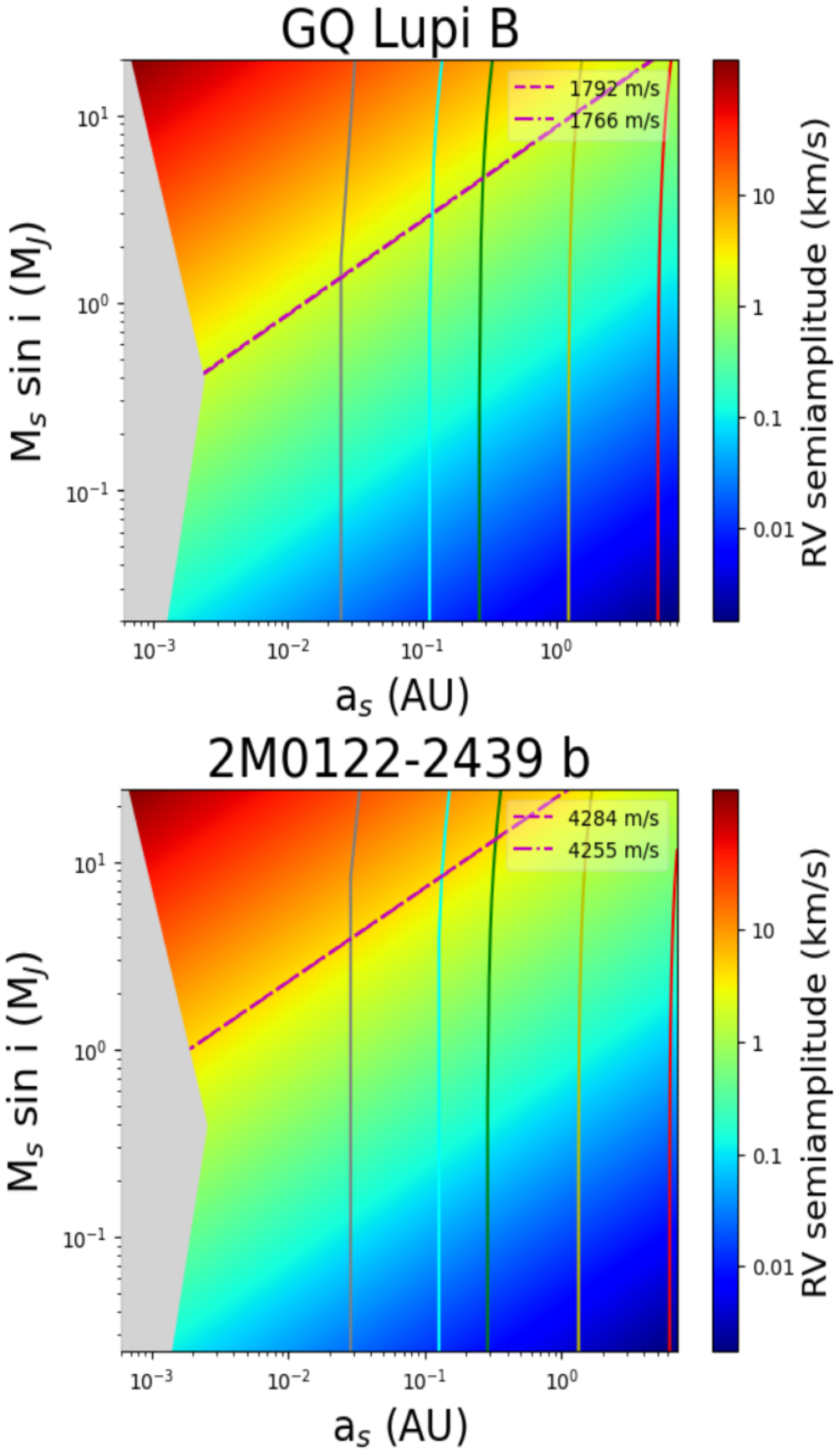

Figure 4.11: Results for CRIRES+ after generating a population of satellites around each target of the sample. The characteristics of the plots are the same as in Figure 4.10.

Conclusions

The research presented in this thesis project focused on identifying binary companions or exomoons by analyzing Doppler measurements from a selected group of directly imaged exoplanets or brown dwarfs. Finding satellites around exoplanets and brown dwarfs will be important for understanding the past and future dynamical evolution of these systems and help characterising their formation scenarios. Additionally, detecting a satellite could bring important implications regarding habitability and the search for extrasolar life. The results of this project are significant for future studies in exoplanetary science, as they identify a group of promising objects that could lead to the discovery of the first exomoon with further observations.

This project started by developing a catalogue of directly imaged exoplanets and brown dwarfs. This technique was chosen among the others because its targets are typically well-separated, young, self-luminous giant planets. Based on the configuration of satellites in our Solar System, these types of targets present very promising characteristics to host larger, hence easier-to-detect, satellites. Moreover, this technique allows to spatially resolve the planet from the star, enabling the application of all the other methods, such as transits or radial velocities. These methods can be applied to the exoplanet itself, rather than to the star, for the search of satellites. Among these techniques, I focused on studying the perturbations of the exoplanet's radial velocity induced by the presence of a satellite orbiting the planet. The radial velocity technique was chosen because it is the second most prolific technique, right after the transit method, with a total of 1097 out of 5756 exoplanets discovered in 30 years[4]. Additionally, with this technique, applied to the exoplanet, more massive and close-in satellites are easier to detect and nowadays instruments allowing us to perform this kind of search have become available.

The catalogue was created by retrieving information about directly imaged exoplanets and brown dwarfs from the NASA and European archives, observable from Paranal Observatory with either CRIRES+ or HiRISE. CRIRES+ is the upgraded high-resolution spectrograph working in the near-infrared, while HiRISE is a new module which links the extreme AO system of the SPHERE instrument to CRIRES+. From this initial catalogue, I rejected objects placed far away from the host star, in particular, exoplanets with angular separations larger than 10", as they would not fit with the instrumental requirements needed to retrieve the spectrum. I also excluded targets around stars with a Gaia magnitude fainter than 12 mag, as this is the operating limit for the adaptive optics system of the instruments considered in this study. Additionally, some specific systems were excluded due to their unique configurations, which would need a more detailed analysis. After selecting the most suitable targets of the catalogue for the radial velocity

[4] https://exoplanetarchive.ipac.caltech.edu/docs/counts_detail.html

analysis, I associated each one to either CRIRES+ or HiRISE based on the target's and the instrument's characteristics. This distinction is important to improve the precision of radial velocity measurements. In fact, the radial velocity precision not only depends on the target characteristics but also on the spectrograph utilized during the observations.

CRIRES+ is an echelle spectrograph that works at high resolution in Infrared wavelengths. It was developed by ESO and it is located at the Nasmyth B focus of UT3 on the VLT at ESO's Paranal Observatory in Chile. HiRISE, instead, is a new fibre-optics tool that couples the high contrast imaging of SPHERE with the high spectral resolution of CRIRES+. It was introduced at VLT in 2023 to suppress more efficiently the stellar noise. In particular, HiRISE spectroscopy is more effective at smaller angular separations because the adaptive optics system of SPHERE performs better than the intrinsic adaptive optics system of CRIRES+ (MACAO). For hosts with H <8.5 and separation of the targeted planet between 0.05-0.35" from the star and hosts with H <7 and separation of the targeted planet between 0.05-0.7" from the star, HiRISE perform better than CRIRES+. Instead, at larger separations, the better efficiency of CRIRES+ standalone coupled with the limited contamination from the central host star even without the SPHERE AO module makes the use of CRIRES+ more advantageous.

The estimation of the radial velocity precision for each target was divided into two steps. First, I analyzed how this precision depends on both the target's and the instrument's characteristics. Then, I computed the fraction of stellar light contaminating the exoplanet's spectrum, which reduces the precision of the radial velocity estimate.
In the first part, based on the work by Bouchy et al. (2001), I computed the signal to noise ratio (S/N) for each target and estimated a quality factor range based on its spectral type and rotational velocity. After this, I calculated the radial velocity precision, which depends on the S/N, the quality factor (Q) and an additional factor that I introduced to account for the wavelength coverage range ($\Delta\lambda$), fixed at 300nm. This allowed me to estimate a range of detection limits for each target. Future studies will aim to improve the quality factor estimates and obtain more reliable values for each object based on its spectral type. As a result of this first step, I rejected some targets with very low S/N values, that would not have produced significant results for this project.
In the second part of the analysis, I estimated the contamination from the star in the target spectrum. In particular, I considered the PSF of CRIRES+ and the PSF of SPHERE to understand how much residual stellar flux is present at the radial position of the planet. Such flux was then normalized for the peak of the star itself and converted into a magnitude difference. Thanks to the work by Cunha et al. (2013), I estimated how the magnitude difference would affect the precision of radial velocity measurements. This perturbation depends not only on the mutual distance between the planet and the star but also on the similarities between the two spectra. When the two objects have very similar spectral types, contamination is higher because the two spectra are more difficult to disentangle, while when the two objects have very different spectral types, even at small angular separations, the contamination from the star can be isolated and subtracted without major challenges. In this second part of the project, for both instruments, stellar contamination turned out to deeply impact the results, particularly for targets where the planetary and stellar spectral types were close. As a result of this second step, I selected 5+3 targets that present the most favourable radial velocity conditions for the detection of satellites.

The outcome of this work is, in fact, the identification of a group of directly imaged exoplanets and brown dwarfs for which present instruments have the highest potential to detect satellites. The selected targets are HR 3549 B, HIP 64892 B, and HD 984 B for CRIRES+, and β Pic b and HD 1160 B for HiRISE. These targets have relatively low detection limits and promising conditions for future observations. Moreover, the estimates of their RV precision do not include extrapolations regarding the stellar contamination and are then more reliable, while for other targets a more extended analysis will be necessary in the future. These results confirm that instruments like CRIRES+ and HiRISE are capable of detecting satellites in certain system configurations. Among them, HR 3549 B stands out as the most promising target, with the lowest detection limits (RV_{min}=35m/s and RV_{max}=40m/s). Even if CRIRES+ and HiRISE will not detect any satellite, they would put constraints on whether a certain population of satellites is present or not. For example, from the theory, we would expect that binary planets are common, if this will not be confirmed by observations with these instruments, then we need to review the theory to understand the reason for this inconsistency.

The main limitation during this project and for the outcome of the results is the evaluation of how the shape of the CRIRES+ PSF changes in space. A significant portion of the targets in the CRIRES+ samples was rejected because of the limited knowledge of the PSF distribution at larger separations. However, systems like η Tel B, HIP 78530 B and HD 284149 b were not definitely rejected, as they might provide promising results considering treatments of the PSF shape at large separations. On the other hand, other targets, despite this problem, presented high detection limit values and would require more advanced instrumentation.

As next-generation telescopes like the ELT become operational with more upgraded equipment, the potential for detecting exomoons and binary planets will expand. In particular, the ELT will reduce the contamination from the host star, thanks to a sharper PSF, and it will increase the value of the S/N reachable for each target, thanks to the larger telescope aperture. Moreover, instruments such as the ANDES spectrograph on the E-ELT will refine the detection limits for each planet and improve the chances of detecting smaller, low-mass companions that were previously undetectable. In fact, ANDES will be an extremely stabilized spectrograph and this will reduce significantly the error related to the stability and improve the radial velocity precision for each target. While the astronomical community awaits for this revolutionary instrumentation to be available, the targets selected in this project can still be investigated and may yield significant results with the instruments available today.

In conclusion, although there is still much work to be done, such as extending the observational methods to increase the number of suitable targets, this study has provided an important foundation. Future observations will likely build on these results, bringing us closer to the first discovery of an exomoon.

Appendix A

Flux-magnitude relation

In astronomy, the flux of an object, F, is typically expressed in orders of relative magnitudes, m, which is the logarithmic equivalent of the flux measure with the formula:

$$m = -2.5 \log_{10} F + C$$

where the constant is given by the zero point of the chosen photometric system.

From this formula, to calculate the difference in magnitudes between two sources A and B, knowing their fluxes ratio the formula becomes:

$$m_A - m_B = -2.5 \log_{10} \left(\frac{F_A}{F_B} \right) \tag{A.1}$$

We note that from this equation, a difference in magnitudes of a factor 5 means a difference in the fluxes of a factor 100.

Appendix B

Addition in quadrature

The addition in quadrature is a mathematical operation that combines two or more independent uncertainties in the propagation of uncertainty.

If X, Y, and Z are three independent measurements with independent errors ΔX, ΔY, and ΔZ, respectively, the overall error given by this method is

$$\Delta = \sqrt{(\Delta X)^2 + (\Delta Y)^2 + (\Delta Z)^2}$$

Appendix C

Spectral types

The classification system most commonly used is the Morgan–Keenan (MK) system, which classifies stars based on their spectral characteristics.
This classification system is based on the study of absorption lines in the stellar spectrum, which are caused by specific elements, present in the star atmosphere, absorbing different wavelengths of light.
The MK classification system is reported here:

1. O-Type (T≥33 000 K): Very hot, blue stars with prominent ionized He lines.
2. B-Type (10 000 K≤T≤33 000 K): Blue-white stars with strong neutral He lines.
3. A-Type (7 300 K≤T≤10 000 K): White stars with strong H lines.
4. F-Type (6 000 K≤T≤7 300 K): Yellow-white stars with weaker H lines and stronger metallic lines.
5. G-Type (5 300 K≤T≤6 000 K): Yellow stars like the Sun with prominent Ca lines (like H and K lines) and H lines.
6. K-Type (3 900 K≤T≤5 300 K): Orange stars with even weaker H lines and stronger metal lines.
7. M-Type (2 300 K≤T≤3 900 K): Red stars with strong metallic lines and molecules like titanium oxide.

A common mnemonic utilized for remembering the order of the spectral type letters, from hottest to coolest, is "Oh, Be A Fine Guy/Girl: Kiss Me!"
The spectral class is usually denoted by a letter, followed by a number from 0 to 9, where 0 represents the hottest and 9 represents the coolest stars within each class.
In the MK system, the luminosity class is usually added to the spectral class using Roman numerals, based on the absorption line widths in the star's spectrum. This width varies with the density of the atmosphere and so distinguishes giant stars from dwarfs.

- Class 0 (Ia+): Hypergiants;
- Class I: Supergiants;
- Class II: Bright giants
- Class III: Regular giants;

- Class IV: Subgiants;
- Class V: Main-Sequence stars;
- Class VI (or sd): Subdwarfs;
- Class VII (or D): White Dwarfs

For example, the spectral class for the Sun is then G2V, indicating a main-sequence yellow star with a surface temperature of around 5 800 K.

This project also considered types L and T that represent Brown Dwarfs objects with very low temperatures, hence their emission peak is in the Infrared.

Bibliography

Adams A. D., et al., 2023, , 166, 192

Agol E., Jansen T., Lacy B., Robinson T. D., Meadows V., 2015, , 812, 5

Akeson R. L., et al., 2013, , 125, 989

Allard F., 2014, in Booth M., Matthews B. C., Graham J. R., eds, IAU Symposium Vol. 299, Exploring the Formation and Evolution of Planetary Systems. pp 271–272, doi:10.1017/S1743921313008545

Andrews S. M., Rosenfeld K. A., Wilner D. J., Bremer M., 2011, , 742, L5

Apai D., et al., 2016, , 820, 40

Babcock H. W., 1953, , 65, 229

Bailey V. P., et al., 2023, in Society of Photo-Optical Instrumentation Engineers (SPIE) Conference Series. p. 126800T (arXiv:2309.08672), doi:10.1117/12.2679036

Balmer W. O., et al., 2024, , 167, 64

Baraffe I., Chabrier G., Barman T. S., Allard F., Hauschildt P. H., 2003, , 402, 701

Barnes J. W., O'Brien D. P., 2002, , 575, 1087

Barr A. C., 2016, The Astronomical Review, 12, 24

Beichman C., et al., 2019, , 51, 58

Benisty M., et al., 2021, , 916, L2

Bennett D. P., et al., 2014, , 785, 155

Beuzit J. L., et al., 2019, , 631, A155

Bohn A. J., et al., 2020a, , 492, 431

Bohn A. J., et al., 2020b, , 898, L16

Bohn A. J., et al., 2021, , 648, A73

Bonavita M., Daemgen S., Desidera S., Jayawardhana R., Janson M., Lafrenière D., 2014, , 791, L40

Bonavita M., et al., 2022, , 513, 5588

Bonnefoy M., et al., 2018, , 618, A63

Bouchy F., Pepe F., Queloz D., 2001, , 374, 733

Bozza V., Mancini L., Sozzetti A., eds, 2016, Methods of Detecting Exoplanets Astrophysics and Space Science Library Vol. 428, doi:10.1007/978-3-319-27458-4.

Brown-Sevilla S. B., et al., 2023, , 673, A98

Calissendorff P., et al., 2023, , 947, L30

Chauvin G., 2024, Comptes Rendus Physique, 24, 139

Chauvin G., et al., 2005a, , 430, 1027

Chauvin G., Lagrange A. M., Dumas C., Zuckerman B., Mouillet D., Song I., Beuzit J. L., Lowrance P., 2005b, , 438, L25

Chauvin G., et al., 2005c, , 438, L29

Cheetham A., et al., 2018, , 615, A160

Chen X., Szulágyi J., 2022, , 516, 506

Chomez A., et al., 2023, , 676, L10

Cunha D., Figueira P., Santos N. C., Lovis C., Boué G., 2013, , 550, A75

De Rosa R. J., Nielsen E. L., Wahhaj Z., Ruffio J.-B., Kalas P. G., Peck A. E., Hirsch L. A., Roberson W., 2023, , 672, A94

Delorme J.-R., et al., 2021, Journal of Astronomical Telescopes, Instruments, and Systems, 7, 035006

Dobos V., Charnoz S., Pál A., Roque-Bernard A., Szabó G. M., 2021, , 133, 094401

Domingos R. C., Winter O. C., Yokoyama T., 2006, , 373, 1227

Dorn R. J., et al., 2014, The Messenger, 156, 7

Dorn R. J., et al., 2023, arXiv e-prints, p. arXiv:2301.08048

Fischer D., Howard A., Laughlin G., Macintosh B., Mahadevan S., Sahlmann J., Yee J., 2014, pp 715–737

Follert R., et al., 2014, in Ramsay S. K., McLean I. S., Takami H., eds, Society of Photo-Optical Instrumentation Engineers (SPIE) Conference Series Vol. 9147, Ground-based and Airborne Instrumentation for Astronomy V. p. 914719, doi:10.1117/12.2054197

Fontanive C., et al., 2020, , 905, L14

Gaudi B. S., Winn J. N., 2007, , 655, 550

Gaudi B. S., Seager S., Mennesson B., Warfield K., Kiessling A., 2019, in AGU Fall Meeting Abstracts. pp P52A–01

Geißler K., Metchev S. A., Pham A., Larkin J. E., McElwain M., Hillenbrand L. A., 2012, , 746, 44

Gray D. F., 2005, 3rd ed. Cambridge University Press

Greenbaum A. Z., et al., 2023, , 945, 126

Guerri G., et al., 2009, arXiv e-prints, p. arXiv:0901.2429

Guyon O., 2018, , 56, 315

Helled R., et al., 2014a, in Beuther H., Klessen R. S., Dullemond C. P., Henning T., eds, Protostars and Planets VI. pp 643–665 (arXiv:1311.1142), doi:10.2458/azu˙uapress˙9780816531240-ch028

Helled R., et al., 2014b, in Beuther H., Klessen R. S., Dullemond C. P., Henning T., eds, Protostars and Planets VI. pp 643–665 (arXiv:1311.1142), doi:10.2458/azu˙uapress˙9780816531240-ch028

Heller R., 2014, , 787, 14

Heller R., 2018, in Deeg H. J., Belmonte J. A., eds, , Handbook of Exoplanets. p. 35, doi:10.1007/978-3-319-55333-7˙35

Heller R., Hippke M., 2024, Nature Astronomy, 8, 193

Hong Y.-C., Raymond S. N., Nicholson P. D., Lunine J. I., 2018, , 852, 85

Huélamo N., et al., 2008, , 489, L9

Hwang K. H., et al., 2018, , 155, 259

Inderbitzi C., Szulágyi J., Cilibrasi M., Mayer L., 2020, , 499, 1023

Janson M., et al., 2021, , 600, 231

Jovanovic N., et al., 2013, in Esposito S., Fini L., eds, Proceedings of the Third AO4ELT Conference. p. 94 (arXiv:1310.0476), doi:10.12839/AO4ELT3.13396

Kaltenegger L., 2010, , 712, L125

Kaushik M., Mattoo A., Rastogi R., 2024, arXiv e-prints, p. arXiv:2404.09143

Kenworthy M. A., Codona J. L., Hinz P. M., Angel J. R. P., Heinze A., Sivanandam S., 2007, , 660, 762

Kervella P., Homan W., Richards A. M. S., Decin L., McDonald I., Montargès M., Ohnaka K., 2016, , 596, A92

Kipping D. M., 2009, , 392, 181

Kipping D., et al., 2022, 54, 504.04

Köhler R., Ratzka T., Petr-Gotzens M. G., Correia S., 2013, , 558, A80

Konopacky Q. M., Ghez A. M., Barman T. S., Rice E. L., Bailey J. I. I., White R. J., McLean I. S., Duchêne G., 2010, , 711, 1087

Langlois M., et al., 2021, , 651, A71

Law C. J., Booth A. S., Öberg K. I., 2023, , 952, L19

Lazzoni C., et al., 2020, , 641, A131

Lazzoni C., Desidera S., Gratton R., Zurlo A., Mesa D., Ray S., 2022, , 516, 391

Lazzoni C., Rice K., Zurlo A., Hinkley S., Desidera S., 2024, , 527, 3837

Li X.-R., Lin Y.-T., Qiu K.-B., 2019, Research in Astronomy and Astrophysics, 19, 111

Liebig C., Wambsganss J., 2010, , 520, A68

Limbach M. A., Vos J. M., Winn J. N., Heller R., Mason J. C., Schneider A. C., Dai F., 2021, , 918, L25

Liu M. C., et al., 2011, , 740, 108

Liu M. C., Dupuy T. J., Bowler B. P., Leggett S. K., Best W. M. J., 2012, , 758, 57

Lovis C., Fischer D., 2010, in Seager S., ed., , Exoplanets. pp 27–53

Macintosh B. A., et al., 2014, in Marchetti E., Close L. M., Vran J.-P., eds, Society of Photo-Optical Instrumentation Engineers (SPIE) Conference Series Vol. 9148, Adaptive Optics Systems IV. p. 91480J, doi:10.1117/12.2056709

Maire A.-L., et al., 2021, Journal of Astronomical Telescopes, Instruments, and Systems, 7, 035004

Marconi A., et al., 2024, arXiv e-prints, p. arXiv:2407.14601

Martinez R. A., Kraus A. L., 2022, , 163, 36

Mayor M., Queloz D., 1995, , 378, 355

Mayor M., et al., 2003, The Messenger, 114, 20

Mégevand D., et al., 2014, in Ramsay S. K., McLean I. S., Takami H., eds, Society of Photo-Optical Instrumentation Engineers (SPIE) Conference Series Vol. 9147, Ground-based and Airborne Instrumentation for Astronomy V. p. 91471H, doi:10.1117/12.2055816

Mesa D., et al., 2016, , 593, A119

Meshkat T., et al., 2015, , 453, 2378

Miyazaki S., et al., 2018, , 156, 136

Morbidelli A., Lunine J. I., O'Brien D. P., Raymond S. N., Walsh K. J., 2012, Annual Review of Earth and Planetary Sciences, 40, 251

Mosqueira I., Estrada P. R., 2003, , 163, 232

Murray C. D., Correia A. C. M., 2010, in Seager S., ed., , Exoplanets. pp 15–23, doi:10.48550/arXiv.1009.1738

Nielsen E. L., Liu M. C., Wahhaj Z., Biller B. A., Hayward T. L., Hayward 2014, in Booth M., Matthews B. C., Graham J. R., eds, IAU Symposium Vol. 299, Exploring the Formation and Evolution of Planetary Systems. pp 60–61, doi:10.1017/S1743921313007874

Ochiai H., Nagasawa M., Ida S., 2014, , 790, 92

Otten G. P. P. L., et al., 2021, , 646, A150

Oza A. V., et al., 2019a, , 885, 168

Oza A. V., et al., 2019b, , 885, 168

Palle E., et al., 2023, arXiv e-prints, p. arXiv:2311.17075

Pearson S. G., McCaughrean M. J., 2023, arXiv e-prints, p. arXiv:2310.01231

Perryman M., 2018, The Exoplanet Handbook

Phillips M. W., et al., 2020, , 637, A38

Pineda J. E., et al., 2019, , 871, 48

Pollack J. B., Hubickyj O., Bodenheimer P., Lissauer J. J., Podolak M., Greenzweig Y., 1996, , 124, 62

Queloz D., et al., 2001, , 379, 279

Rodenbeck K., Heller R., Gizon L., 2020, , 638, A43

Rosario-Franco M., Quarles B., Musielak Z. E., Cuntz M., 2020, , 159, 260

Rouan D., Riaud P., Boccaletti A., Clénet Y., Labeyrie A., 2000, , 112, 1479

Ruffio J.-B., et al., 2023, , 165, 113

Saar S. H., Butler R. P., Marcy G. W., 1998, in Donahue R. A., Bookbinder J. A., eds, Astronomical Society of the Pacific Conference Series Vol. 154, Cool Stars, Stellar Systems, and the Sun. p. 1895

Sajadian S., Sangtarash P., 2023, , 520, 5613

Santerne A., 2018, in Deeg H. J., Belmonte J. A., eds, , Handbook of Exoplanets. p. 154, doi:10.1007/978-3-319-55333-7˙154

Sasaki T., Stewart G. R., Ida S., 2010, , 714, 1052

Schmidt T. O. B., Mugrauer M., Neuhäuser R., Vogt N., Witte S., Hauschildt P. H., Helling C., Seifahrt A., 2014, , 566, A85

Snellen I. A. G., Brandl B. R., de Kok R. J., Brogi M., Birkby J., Schwarz H., 2014, , 509, 63

Sparks W. B., Ford H. C., 2002, , 578, 543

Squicciarini V., et al., 2022, , 664, A9

Sutlieff B. J., et al., 2023, , 520, 4235

Szabó G. M., Schneider J., Dencs Z., Kálmán S., 2024, Universe, 10, 110

Szulágyi J., Garufi A., 2021, , 506, 73

Szulágyi J., Mayer L., Quinn T., 2017, , 464, 3158

Szulágyi J., Dullemond C. P., Pohl A., Quanz S. P., 2019, , 487, 1248

Teachey A., 2024, arXiv e-prints, p. arXiv:2401.13293

Teachey A., Kipping D. M., 2018, Science Advances, 4, eaav1784

Trani A. A., Hamers A. S., Geller A., Spera M., 2020, , 499, 4195

Traub W. A., Oppenheimer B. R., 2010, in Seager S., ed., , Exoplanets. pp 111–156

Vanderburg A., Rodriguez J. E., 2021, , 922, L2

Vanderburg A., Rappaport S. A., Mayo A. W., 2018, , 156, 184

Vigan A., et al., 2021, , 651, A72

Vigan A., et al., 2024, , 682, A16

Wagner K., Apai D., Kasper M., McClure M., Robberto M., Currie T., 2020, , 902, L6

Wang J., et al., 2022, , 163, 189

Ward-Duong K., et al., 2021, , 161, 5

Wolszczan A., Frail D. A., 1992, , 355, 145

Wu Y.-L., et al., 2022, , 930, L3

Yamamoto K., et al., 2013, , 65, 90

Zhou Y., et al., 2021, , 161, 244

Zhuang Q., Gao X., Yu Q., 2012, , 758, 111

Zurlo A., 2024, arXiv e-prints, p. arXiv:2404.05797

Zurlo A., et al., 2022, , 666, A133

van Holstein R. G., et al., 2021, , 647, A21